

DISS. ETH NO. 15668

# **THE GREENHOUSE EFFECT IN THE ALPS – BY MODELS AND OBSERVATIONS**

A dissertation submitted to the  
SWISS FEDERAL INSTITUTE OF TECHNOLOGY  
ZURICH

for the degree of  
DOCTOR OF NATURAL SCIENCES

presented by  
BRUNO DÜRR  
Dipl. Natw. ETH  
born 16 October 1975  
citizen of Gams (SG)

accepted on the recommendation of  
Prof. Dr. Atsumu Ohmura, examiner  
PD Dr. Rolf Philipona, co-examiner  
Prof. Dr. Michael Kuhn, co-examiner

2004



# Abstract

The investigation of the greenhouse effect at the Earth's surface has become a key issue in climate science. It is widely accepted that global mean temperature and greenhouse gas concentrations substantially rised during the 20th century, but a clear experimental evidence to link the temperature rise at the surface to enhanced greenhouse radiative forcing is still lacking.

The Alpine Surface Radiation Budget (ASRB) project was initiated in 1994 to investigate radiation balance and greenhouse effect in the Alps from 370 m a.s.l. to 3580 m a.s.l. at ten radiation stations. The strong decrease of temperature, and thus water vapour, with height allows to examine different radiation fluxes under strongly varying ambient temperature and humidity.

ASRB instruments were calibrated in situ with a Travelling Standard during 2000 and 2001 to monitor longterm stability of ASRB measurements. The comparison of the new calibration factors with old factors from 1996/97 revealed that PIR pyrgeometers remained very stable all over the years. The shielding effect of obstacles around the stations was re-evaluated.

The Clear-Sky Index (*CSI*) method was improved to accurately detect cloud-free situations also during night- and wintertime. An Automatic Partial Cloud Amount Detection Algorithm (*APCADA*) was developed to estimate cloud cover without cirrus clouds every ten minutes during day- and nighttime.

Cloud-free longwave downward radiation computations from two different Radiative Transfer Models (RTMs) were compared with measurements at eight ASRB stations. The complex model MODTRAN delivered accurate results for cold and warm ambient temperatures. However substantial deficiencies in the order of  $-20 \text{ W m}^{-2}$  were found for the simplified RTM used in the operational Numerical Weather Prediction (NWP) model "aLMo" at MeteoSwiss in Zurich.

Eight years of annual mean downward and upward radiative fluxes at the ASRB stations Payerne (490 m a.s.l.) and at the experimental field of the Swiss Avalanche Institute (SLF), called SLF-Versuchsfeld (2540 m a.s.l.), were statistically examined. The total heating radiation (*THR*) and the longwave upward radiation (*LUR*) from the surface significantly increased at both stations. Surface albedo, however, has slightly decreased at both sites, which mostly explains the increase of net shortwave radiation. The shortwave cloud effect (*SCE*) for the Earth's surface remained rather stable, but the longwave cloud effect (*LCE*) decreased at both stations. Thus the net cloud effect (*NCE*) also decreased and slightly reduced the strong increase of *THR*. The cloud-free greenhouse effect increased in the order of  $1 \text{ W m}^{-2}$  per year. The increase of the all-sky greenhouse effect is less pronounced due to the decreasing longwave cloud effect (*LCE*).



# Zusammenfassung

Die Erforschung des Treibhauseffektes der Erdatmosphäre ist zu einem Kernthema der Klimawissenschaften geworden. Es besteht weitgehend Übereinstimmung darüber, dass die mittlere globale Temperatur und die Konzentrationen der wichtigsten Treibhausgase im 20. Jahrhundert deutlich angestiegen sind. Es fehlen jedoch bis heute schlüssige experimentelle Beweise dafür, dass der Temperaturanstieg und die Zunahme der Treibhausgase kausal in einem Zusammenhang stehen.

Das Projekt zur Schaffung eines alpinen Strahlungsbilanzmessnetzes (ASRB) wurde 1994 ins Leben gerufen, um die Strahlungsbilanz und den Treibhauseffekt von 370 bis 3580 m ü.M. an zehn Stationen in den Alpen untersuchen zu können. Die starke Abnahme der Temperatur, und damit des Wassergehaltes, mit der Höhe ermöglicht die Erforschung von verschiedenen Strahlungsflüssen unter wechselnden Temperatur- und Feuchteverhältnissen. Es ist jedoch keine leichte Aufgabe, qualitativ hochwertige Strahlungsmessungen unter alpinen Wetterbedingungen aufrecht erhalten zu können.

Die Strahlungsinstrumente des ASRB wurden in den Jahren 2000 und 2001 an Ort und Stelle mit einem Vergleichsstandard kalibriert. Der Vergleich der neuen Kalibrationsfaktoren mit den alten Faktoren aus den Jahren 1996/97 hat gezeigt, dass die PIR Pyrgeometer über die Jahre hinweg stabil geblieben sind. Die Beeinflussung der Messung durch Hindernisse an den Stationen wurde neu evaluiert.

Die Clear-Sky Index (CSI) Methode wurde verbessert, um wolkenlose Situationen auch nachts und während des Winters besser erfassen zu können. Ein automatisches Verfahren zur Bestimmung der Wolkenbedeckung ohne Cirren (APCADA) wurde entwickelt, welches alle 10 Minuten und rund um die Uhr eine Schätzung der Wolkenbedeckung liefert.

Berechnungen der langwelligen Gegenstrahlung unter wolkenlosen Bedingungen von zwei verschiedenen Strahlungstransfermodellen wurden mit Messungen an acht ASRB-Stationen verglichen. Das komplexe Strahlungstransfermodell MODTRAN lieferte sowohl für kalte, als auch für warme Umgebungstemperaturen gute Resultate. Das vereinfachte Strahlungstransfermodell, welches im operationellen Wettervorhersagemodell "aLMo" an der MeteoSchweiz verwendet wird, unterschätzte die langwellige Gegenstrahlung jedoch in der Grössenordnung von  $-20 \text{ W m}^{-2}$ .

Jährliche Mittelwerte der einfallenden und ausgehenden Strahlungsflüsse von acht Jahren an den ASRB-Stationen Payerne (490 m ü.M.) und SLF-Versuchsfeld (2540 m ü.M.) wurden statistisch ausgewertet. Die totale absorbierte Strahlung (*THR*) und thermische Emission der Erdoberfläche (*LUR*) sind an beiden Stationen signifikant angestiegen. Die Oberflächenalbedo hat dagegen etwas abgenommen, womit der leichte Anstieg der kurzwelligen Nettostrahlung erklärt werden kann. Der kurzwellige Wolkeneffekt (*SCE*) an der Erdoberfläche blieb mehr oder weniger stabil, doch nahm der Netto-Wolkeneffekt (*NCE*) leicht ab, d.h. der Einfluss der Wolken hatte einen dämpfenden Effekt auf die Zunahme der *THR*. Der Treibhauseffekt unter wolkenlosem Himmel hat um rund  $1 \text{ W m}^{-2}$  pro Jahr zugenommen. Der Anstieg des Treibhauseffektes über alle Verhältnisse gesehen fällt etwas weniger deutlich aus, da der langwellige Wolkeneffekt (*LCE*) leicht abgenommen hat.



# Contents

<b>Abstract</b>	<b>3</b>
<b>Zusammenfassung</b>	<b>5</b>
<b>Abbreviations and Acronyms</b>	<b>11</b>
<b>1 Introduction</b>	<b>13</b>
1.1 Motivation . . . . .	13
1.2 Objectives . . . . .	13
<b>2 Observational Data</b>	<b>15</b>
2.1 ASRB Network . . . . .	15
2.2 BSRN Network . . . . .	16
<b>3 Theory of the installation and calibration</b>	<b>17</b>
3.1 Introduction . . . . .	17
3.2 Correction of Direct Solar Radiation Influence on <i>LDR</i> . . . . .	17
3.2.1 Description of Sun Correction Method used in ASRB . . . . .	17
3.2.2 Real-time Estimation of Direct Solar Radiation . . . . .	18
3.2.3 Comparison of Estimated and Measured <i>SDR<sub>d</sub></i> . . . . .	19
3.3 Re-evaluation of ASRB Shielding Factor . . . . .	23
3.3.1 Determination of Sky Shielding . . . . .	23
3.3.2 Determination of Obstacle Influence on <i>LDR</i> . . . . .	24
3.4 Calibration of Travelling Standard and ASRB Davos . . . . .	25
3.5 Calibration of ASRB Pyrgeometers . . . . .	26
3.5.1 Evaluation of <i>LDR</i> Data from First Field Calibration Campaign . . . . .	28
3.6 Summary . . . . .	28
<b>4 Cloud Amount Detection</b>	<b>31</b>
4.1 Introduction . . . . .	31
4.2 Observational Data . . . . .	31
4.2.1 Observed Irradiances . . . . .	31
4.2.2 Synoptic Observations . . . . .	32
4.3 Requirements to Automatic Cloud Amount Detection . . . . .	32
4.4 Automatic Partial Cloud Amount Detection . . . . .	33
4.4.1 Variability of Longwave Downward Radiation . . . . .	33
4.4.2 The Improved Clear-Sky Index . . . . .	33
4.4.3 Determination of Site Specific Functions $k(t)$ and $\Delta k(t)$ . . . . .	35

4.4.4	Example Fit of $k$ and $\Delta k$ . . . . .	36
4.4.5	Estimation of Partial Cloud Amount . . . . .	37
4.5	Results for APCADA Cloud Cover Estimation . . . . .	39
4.5.1	Comparison of Partial Cloud Amount at ASRB Station Payerne . . . . .	39
4.5.2	Performance of APCADA in Different Climate Regions . . . . .	39
4.6	Discussion . . . . .	41
4.6.1	Comparison of Observed and Estimated Partial Cloud Amount . . . . .	41
4.6.2	Comparison of Single Day in Payerne . . . . .	41
4.6.3	Implementation of APCADA in Different Climate Regions . . . . .	43
4.6.4	Cloud Amount Detection without High Clouds . . . . .	43
4.7	Conclusions . . . . .	43
<b>5</b>	<b>Homogenisation of Longterm LDR Series</b>	<b>45</b>
5.1	Introduction . . . . .	45
5.2	Methods . . . . .	45
5.2.1	<i>CFI</i> -Saturation . . . . .	45
5.2.2	<i>CFI</i> -Saturation Inhomogeneities . . . . .	46
5.2.3	Correction of Inhomogeneous <i>LDR</i> Series . . . . .	47
5.3	Comparison of uncorrected and corrected <i>LDR</i> series . . . . .	48
5.3.1	ASRB Station Davos . . . . .	48
5.3.2	ASRB Station Jungfrauoch . . . . .	50
5.4	Discussion . . . . .	50
5.4.1	Reasons for <i>LDR</i> Inhomogeneities . . . . .	50
5.4.2	Limitations of Longterm <i>LDR</i> Series Correction . . . . .	52
5.5	Conclusions . . . . .	52
<b>6</b>	<b>Comparison of Observed and Modeled Longwave Downward Radiation</b>	<b>53</b>
6.1	Introduction . . . . .	53
6.2	Observational Data . . . . .	53
6.2.1	ASRB Data . . . . .	53
6.2.2	Cloud-Free Situations . . . . .	54
6.3	Models and Experiments . . . . .	54
6.3.1	MODTRAN and Input Data . . . . .	54
6.3.2	aLMo . . . . .	55
6.3.3	Assimilation of Atmospheric Profiles in MODTRAN . . . . .	56
6.3.4	Height Correction of Computed <i>LDR</i> . . . . .	57
6.3.5	Description of <i>LDR</i> Model Experiments . . . . .	57
6.4	<i>LDR</i> Computation Experiments . . . . .	58
6.4.1	Experiment 1.: Performance of MODTRAN . . . . .	58
6.4.2	Experiment 2.: Comparison of MODTRAN and aLMo Radiative Transfer Model . . . . .	60
6.4.3	Experiment 3.: Comparison of Measured and Forecasted Vertical Profiles . . . . .	62
6.4.4	Experiment 4.: Insertion of Measured Surface Data . . . . .	63
6.5	Summary . . . . .	64
<b>7</b>	<b>Greenhouse Effect in the Alps</b>	<b>67</b>
7.1	Introduction . . . . .	67
7.2	Greenhouse- and Cloud Radiative Effect . . . . .	67
7.2.1	Modelling of Greenhouse Effect . . . . .	68



---

7.3	Surface Radiation Balance . . . . .	70
7.4	Greenhouse Effect in the Alps . . . . .	73
7.5	Summary . . . . .	73
<b>8</b>	<b>Conclusions</b>	<b>75</b>
8.1	Synthesis . . . . .	75
8.1.1	Maintenance of ASRB Network . . . . .	75
8.1.2	Detection of Cloud-Free Sky . . . . .	75
8.1.3	Estimation of Diffuse Shortwave Downward Radiation . . . . .	75
8.1.4	Homogenisation of <i>LDR</i> Time Series . . . . .	76
8.1.5	Longwave Downward Radiation Modelling . . . . .	76
8.1.6	Radiation Budget, Cloud- and Greenhouse Effect . . . . .	76
8.2	Outlook . . . . .	76
<b>A</b>	<b>Code for diffuse SDR estimation</b>	<b>79</b>
	<b>List of Figures</b>	<b>81</b>
	<b>List of Tables</b>	<b>85</b>
	<b>Bibliography</b>	<b>87</b>
	<b>Acknowledgements</b>	<b>91</b>
	<b>Curriculum Vitae</b>	<b>93</b>



# Abbreviations and Acronyms

**Table 1:** *Abbreviations and acronyms used in this study*

Abbr./Acro.	Definition
aLMo	<i>a</i> Lpine Model, NWP model used at MeteoSwiss
ANETZ	MeteoSwiss automatic network
APCADA	Automatic Partial Cloud Amount Detection Algorithm
ASRB	Alpine Surface Radiation Budget network
ASRB-TS	ASRB Travelling Standard
BSRN	Baseline Surface Radiation Network
<i>CSI</i>	Clear-Sky Index
<i>CFI</i>	Cloud-Free Index
<i>CFI</i> <sub>sat</sub>	Cloud-Free Index saturation
DAV	ASRB-station Davos
ENET	MeteoSwiss complementary network
GCM	General Circulation Model
IWC	Integrated Water Content
JFJ	ASRB-station Jungfrauoch
KWA	BSRN-station Kwajalein
<i>LCE</i>	Longwave Cloud Effect
<i>LDR</i>	Longwave Downward Radiation
<i>LNR</i>	Longwave Net Radiation
LOM	ASRB-station Locarno-Monti
<i>LOR</i>	Longwave Outgoing Radiation
<i>LUR</i>	Longwave Upward Radiation
MAE	ASRB-station Männlichen
MeteoSwiss	Federal Office of Meteorology and Climatology, Zurich, Switzerland
MODTRAN	MODerate TRANsfer model
<i>NCE</i>	Net Cloud Effect
NWP	Numerical Weather Prediction model
NYA	BSRN-station Ny Ålesund
PAY	ASRB-station Payerne
<i>PCA</i>	Partial Cloud Amount
PIR	Precision Infrared Radiometer
PMOD/WRC	Physikalisch-Meteorologisches Observatorium Davos/World Radiation Centre
RTM	Radiative Transfer Model
SBL	Surface Boundary Layer
<i>SCE</i>	Shortwave Cloud Effect

**Table 1:** *Continued ...*

<i>Abr./Acro.</i>	<i>Definition</i>
<i>SDR</i>	Shortwave Downward Radiation
<i>SDR<sub>d</sub></i>	Diffuse Shortwave Downward Radiation
<i>SLF</i>	Swiss Federal Institute for Snow and Avalanche Research, Davos
<i>SNR</i>	Shortwave Net Radiation
<i>SUR</i>	Shortwave Upward Radiation
<i>THR</i>	Total Heating Radiation
<i>TNR</i>	Total Net Radiation
<i>WFJ</i>	ASRB-station Weissfluhjoch
<i>VSF</i>	ASRB-station SLF-Versuchsfeld

# Chapter 1

## Introduction

### 1.1 Motivation

The thesis of Christoph Marty represents the first documentation for the Alpine Surface Radiation Budget (ASRB) project. This chapter follows the comprehensive introduction given by *Marty (2000)*.

Predictions presented by the Intergovernmental Panel on Climate Change (IPCC) indicate that the future mean global surface temperature may rise in the order of 1.5 to 6°C (*Houghton et al., 2001*). Even larger temperature increases are expected for the cold regions of the Earth, e.g. around the poles or mountain areas, because cold regions are more sensitive to radiative forcing. The Alpine Surface Radiation Budget (ASRB) project was initiated in 1994 to complement the world-wide Baseline Surface Radiation Network (BSRN). ASRB stations span from 370 m a.s.l. to 3580 m a.s.l. covering a broad range of different climate zones. This change is comparable to the latitudinal change from central Europe to the Arctic.

A main goal of the ASRB project is to obtain various radiative fluxes at various altitudes north and south of the Alps with high accuracy. ASRB data is used to describe the influence of the greenhouse effect on surface radiation budget and to link rising concentrations of greenhouse gases like H<sub>2</sub>O, CO<sub>2</sub>, CH<sub>4</sub>, and O<sub>3</sub> to the temperature increase at the surface. ASRB data is also ideal for the validation of General Circulation Models (GCMs), Numerical Weather Prediction (NWP) models and satellite based surface radiation retrivals over complex terrain.

### 1.2 Objectives

The main objective of this work was to investigate changes of radiation balance, albedo and cloud- and greenhouse effect in the Alps. Emphasis was mainly laid on the investigation of longwave radiation fluxes. The main objective was supported by the following set of sub-objectives:

- to improve the detection of cloud-free situations and to investigate the effect of cloud cover on surface radiation,
- to develop a real-time method to correct the impact of direct sun on longwave measurements,
- to develop a method to homogenise longterm longwave downward radiation series.

To reach the above mentioned objectives, existing quality- and correction methods for ASRB data were first improved and refined to provide homogenous longterm radiation series for the statistical examination of various radiation fluxes. Secondly, radiative transfer model calculations were validated

with ASRB measurements and later used to provide informations about the top of atmosphere long-wave outgoing radiation. Thirdly, the increase of the greenhouse effect was demonstrated at two ASRB stations on different altitudes in Switzerland.

## Chapter 2

# Observational Data

### 2.1 ASRB Network

The ASRB (Alpine Surface Radiation Budget) project (*Fröhlich et al.*, 1998) was initiated in 1994 to investigate the surface radiation balance and its altitude dependency in a mountainous region, i.e. in the Alps. ASRB data was also intended to be used for the early detection of anthropogenic greenhouse warming. Altitude dependency of the surface radiation budget and cloud effects on radiation were investigated by *Marty et al.* (2002) and first indications for an increasing greenhouse effect in the Alps were found by *Philipona et al.* (2004b). The ASRB is part of the Swiss Atmospheric Radiation Monitoring Program (CHARM). The CHARM program (*Heimo et al.*, 1998) coordinates various radiation monitoring projects with the aim to investigate climate change in Switzerland. The ASRB network (Fig. 2.1) consists of 10 stations between 370 and 3580 m a.s.l. in Switzerland (status end of 2003). Broadband and hemispherically integrated longwave downward radiation (*LDR*) and shortwave downward radiation (*SDR*) are measured at all sites. Three stations (Payerne, Davos and SLF-Versuchsfeld) additionally deliver shortwave upward radiation (*SUR*), i.e. part of *SDR* reflected at the surface, and longwave upward radiation (*LUR*) from the surface. Measurements of upward fluxes from these three stations were used to estimate upward fluxes at the other stations with the help of air temperature and local characteristics of snow cover and ground vegetation (*Marty et al.*, 2002). In collaboration between the Physikalisch-Meteorologisches Observatorium Davos/World Radiation Centre (PMOD/WRC) and the Federal Office of Meteorology and Climatology (MeteoSwiss) the ASRB network was built at stations of the MeteoSwiss automatic network (ANETZ) and complementary network (ENET) in 1994/95.

Eppley Precision Infrared Radiometer (PIR) pyrgeometers and Kipp & Zonen CM21 pyranometers are used to measure *LDR*, respectively *SDR* at screen level height, i.e. 2 m above the surface. PIR and CM21 outputs are sampled every two seconds and averaged over 2 minutes. CM21 are calibrated with the World Standard Group (WSG) and a shaded reference pyranometer at PMOD/WRC in Davos. The WSG measures the direct *SDR* component, and the shaded reference pyranometer the diffuse *SDR* component. The PIRs were modified at PMOD/WRC to improve uncertainty to  $\pm 3 \text{ W m}^{-2}$  (*Philipona et al.*, 1995). An extended round-robin experiment revealed that PIR measurements remained stable over a long time period (*Philipona et al.*, 1998). PIR and CM21 instruments are calibrated in situ against a Travelling Standard about every three years (see Section 3).

A special ventilation system using slightly preheated air was developed at PMOD/WRC to prevent dew and hoar-frost on domes of radiometers and to reduce the temperature gradient between the instruments body and dome (*Marty et al.*, 2002). Pyranometers are affected by temperature differences between dome and body, which lead to the so called zero-offset (*Wardle and Barton*, 1988). An appropriate ventilation and heating system significantly reduces the atmospheric effects and the zero-offset

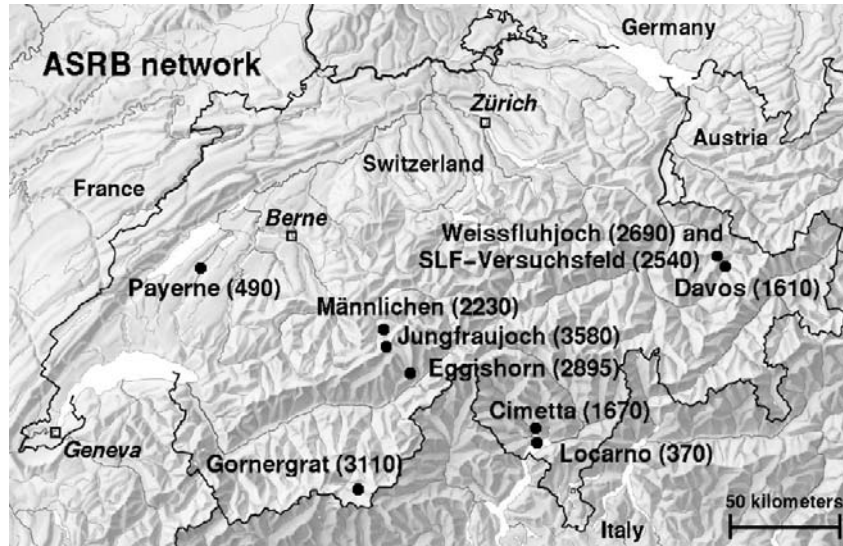


**Figure 2.1:** The Alpine Surface Radiation Budget (ASRB) network in Switzerland, Central Europe (Latitude  $\approx 46^\circ\text{N}$ ). In parenthesis altitudes are given in meter a.s.l.

(Philipona, 2002). The remoteness of the stations and harsh weather conditions did not allow the use of a common mechanical shading disc system to prevent direct solar radiation on PIRs. Instead, all sites are equipped with a fixed shadow band in direction south. The dip of *LDR* due to the shadow at solar noon is used to correct the inadvertent shortwave influence on the *LDR* measurement (Marty, 2000).

All ASRB sites are equipped with the ventilated thermo hygrometer VTP6 (Ruppert, 1991), called THYGAN. The THYGAN measures air temperature and relative humidity at screen level height. The humidity sensor is a mirror dew point hygrometer. Values are obtained every 10 minutes averaged over 40 seconds. The THYGAN functions well also under very cold and stormy alpine weather conditions.

## 2.2 BSRN Network

The BSRN (Baseline Surface Radiation Network) network (Ohmura *et al.*, 1998) is part of the World Climate Research Program (WCRP) and consists of about 30 radiation sites worldwide. The basic measurements at BSRN stations are broadband shortwave and longwave downward radiation (*SDR*, *LDR*), diffuse and direct shortwave radiation, and temperature, relative humidity and air pressure at screen level height. Some stations provide further radiation measurements, e.g. upward radiation fluxes, and/or synoptic observations and/or radiosonde data. Type and setup of radiation instruments and associated ventilation and shading disc systems vary from site to site and are described by McArthur (1998). Data collection, quality control and data delivery are handled by the World Radiation Monitoring Centre (WRMC) at the Institute of Atmospheric and Climate Science at the ETH (IACETH) in Zurich (Gilgen *et al.*, 1995).



## Chapter 3

# Theory of the installation and calibration

### 3.1 Introduction

ASRB longwave downward radiation ( $LDR$ ) measurements are both affected by the influence of direct solar radiation and by the shielding effect of obstacles in the field of view (*Marty*, 2000). The real-time operation of APCADA (see Chapter 4) claims for a real-time correction of the direct solar radiation. Thus a new method was developed to separate the global shortwave downward radiation ( $SDR$ ) into a direct and diffuse part. The ASRB shadowband and surrounding obstacles have an effect on  $LDR$  measurements due to the shielding of the field of view. The application of the ASRB-Travelling Standard (ASRB-TS) at the different locations made it necessary to describe the geometry and to estimate the obstacle influence on  $LDR$ . The theory of the obstacle effect on  $LDR$  is discussed in the following sections.

The longterm investigation of the surface radiation balance over the Alps claims for regular instrument calibration. The ASRB-TS made up of the same instruments than ASRB is used to calibrate ASRB instruments in situ. Thus ASRB instruments don't have to be moved and ASRB setup rests the same all over the time. The ASRB-TS itself is regularly calibrated at PMOD/WRC in Davos. Unfortunately the ASRB-TS instruments were only ventilated, but the air stream was not heated because there were problems to get enough electrical power at some ASRB sites. However *Philipona* (2002) shows that pyranometers have to be ventilated and the air stream has to be slightly heated to measure global shortwave radiation accurately. Hence only the calibration of ASRB pyrgeometers is presented here.

### 3.2 Correction of Direct Solar Radiation Influence on $LDR$

PIR pyrgeometers have to be permanently shaded to avoid the influence of direct solar radiation on raw longwave downward radiation ( $LDR_{raw}$ ) measurements. The effect of the sun on  $LDR_{raw}$  can reach up to  $20 \text{ W m}^{-2}$  for a pyrgeometer (*Marty*, 2000). However it is impossible to shade ASRB PIRs permanently due to the harsh weather conditions in the Alps. A fixed shadowband was installed instead, which allows to determine the effect of direct solar radiation on  $LDR_{raw}$  at solar noon.

#### 3.2.1 Description of Sun Correction Method used in ASRB

*Marty* (2000) presents a method to correct the inadvertent measured direct solar radiation on unshaded ASRB pyrgeometers. The direct solar radiation is calculated from the difference of global shortwave downward radiation ( $SDR$ ) and estimated diffuse  $SDR$  ( $SDR_d$ ). All ASRB sites except Jungfraujoch after 1997 are equipped with a fixed shadow band in direction south, which causes a dip of  $SDR$  and

$LDR_{\text{raw}}$  at solar noon. Therefore,  $SDR_d$  and  $LDR_{\text{raw}}$  are measured without direct solar radiation for about 10 minutes during noontime only. All other  $SDR_d$  values between sunrise and sunset are found with the help of a cubic spline interpolation using the value measured at solar noon. This method is hereinafter referred to as cubic spline method. The corrected  $LDR$  during daytime is calculated by:

$$LDR = LDR_{\text{raw}} - \Delta LDR_{\text{sun}} \quad (3.1)$$

$$\Delta LDR_{\text{sun}} = f \left( \frac{SDR - SDR_d}{1000} \right), \quad (3.2)$$

where  $f$  is a station specific factor.  $f$  is obtained using Eq. 3.2 and measured  $\Delta LDR_{\text{sun}}$  and  $SDR - SDR_d$  values from cloud-free noon situations over one year with a strong shadow dip of  $SDR$  and  $LDR_{\text{raw}}$ . The correction of  $LDR_{\text{raw}}$  with the help of direct solar radiation is hereinafter referred to as  $f$ -correction of  $LDR$ .

### 3.2.2 Real-time Estimation of Direct Solar Radiation

The old daytime  $LDR$  correction using the cubic spline method only allows to postprocess  $SDR$  measurements, because the method depends on the knowledge of  $SDR_d$  at solar noon. However, APCADA is operated real-time, and the direct sun influence on  $LDR_{\text{raw}}$  has therefore to be corrected for each timestep.

A scheme was developed to directly estimate  $SDR_d$  from  $SDR$  measurements based on two minutes data. The occurrence of clouds leads to an increased variability of  $SDR$  analogous to the variability of  $LDR$  described in section 4.4.1. Thus low  $SDR$  variability roughly indicates cloud-free or overcast situations. As a second criterion, the transmissivity  $q$  of  $SDR$  compared to the top of the atmosphere solar irradiance  $SDR_0$  is used:

$$q = \left( \frac{SDR}{SDR_0 \cos \theta} \right)^{\frac{1}{m}}, \quad \cos \theta > 0 \quad (3.3)$$

$$q = 1, \quad \cos \theta \leq 0 \quad (3.4)$$

$$\cos \theta = \cos(H) \cos(\phi) \cos(\delta) + \sin(\phi) \sin(\delta), \quad (3.5)$$

$$SDR_0 = TSI \left( \frac{d_0}{d_{E-S}} \right)^2, \quad (3.6)$$

$$m = \frac{1}{\sin(\epsilon_S) + 0.1500(\epsilon_S + 3.885)^{-1.253}}, \quad (3.7)$$

where  $SDR_0$  depends on the actual ( $d_{E-S}$ ) and average ( $d_0$ ) Earth - Sun distance. The mean total solar irradiance ( $TSI$ ) at the top of the atmosphere has a value of  $1366 \text{ W m}^{-2}$  (Fröhlich and Lean, 1998). The cosine of the zenith angle ( $\theta$ ) is calculated using latitude  $\phi$ , sun declination  $\delta$  and solar hour angle  $H$ . Optical air mass  $m$  (Kasten and Young, 1989) depends on the solar elevation  $\epsilon_S$  in degrees.

A lower limit of  $q$  for cloud-free situations was empirically found using a fourth order polynomial:

$$q_{\text{limit}} = (0.80 + \Delta q) + (0.20 - \Delta q) \left( \frac{t_i - \bar{t}}{t_n - t_0} \right)^4, \quad (3.8)$$

where  $t_i$  roughly indicates the time between sunrise ( $t_0$ ,  $\epsilon \approx -3^\circ$ ) and sunset ( $t_n$ ,  $\epsilon \approx -3^\circ$ ), and  $\bar{t} = t_0 + \frac{t_n - t_0}{2}$  the time of solar noon. A height dependent seasonal transmissivity offset  $\Delta q$  (see Tab. 3.1) had to be introduced to account for increased  $SDR_d$  during the winter half year due to low sun elevation and increased surface albedo due to snow cover.

The measured transmissivity  $q$  is averaged over 10 minutes ( $q_{\text{avg}}$ ) to be compared to  $q_{\text{limit}}$  for every timestep. A difference  $q_{\text{diff}} = q_{\text{avg}} - q_{\text{limit}}$  near zero and low variability indicates cloud-free conditions.

The variability of  $q$  within the past 30 minutes is expressed with two different variables, the standard deviation  $q_{\text{std}}$  and range  $q_r$ :

$$q_r = \frac{q_{i-1,\text{max}} + q_{i,\text{max}} + q_{i+1,\text{max}}}{3} - \frac{q_{j-1,\text{min}} + q_{j,\text{min}} + q_{j+1,\text{min}}}{3} \quad (3.9)$$

The position of the maximum within the last 30 minutes is given by  $i$  ( $i_0, \dots, i_{14}$ ), and  $j$  ( $j_0, \dots, j_{14}$ ) indicates the minimum of  $q$ . If  $i = 0$ , then  $q_{i-1,\text{max}} = q_{i,\text{max}}$ . If  $i = 14$ , then  $q_{i+1,\text{max}} = q_{i,\text{max}}$ . The same applies also for  $j = 0$  and  $j = 14$ .

### Scheme for Real-Time Estimation of $SDR_d$

The three ASRB stations Payerne (PAY), Davos (DAV) and SLF-Versuchsfeld (VSF) are accompanied by  $SDR_d$  measurements using permanently shaded pyranometers on sun tracker systems.  $SDR_d$  in PAY is obtained from the BSRN station, and instruments from PMOD/WRC are running at VSF and DAV. A large set of manually selected days with  $SDR$  and  $SDR_d$  measurements from these sites covering cloud-free, cirrus, broken cloud and overcast situations were used to develop heuristic rules to estimate  $SDR_d$ .  $q_{\text{std}}$  was used as a main parameter to distinct broken cloud from cloud free or overcast conditions. Small values of  $q_{\text{diff}}$  and  $SDR$  variability indicate cloud-free situations or the occurrence of high clouds. Large values of  $q_{\text{diff}}$  and small  $SDR$  variability, however, indicate overcast situations, where  $SDR = SDR_d$ . Cases with broken clouds passing the sun show large  $SDR$  variability and either  $SDR_{d,i}$  is set equal to the last value ( $SDR_{d,i} = SDR_{d,i-1}$ ), or  $SDR_{d,i}$  is calculated solving Eq. 3.3 for  $SDR$  and inserting the minimum of  $q$  within the last 30 minutes ( $q_{\text{min}}$ ):

$$SDR_{d,i} = SDR_0 \cos\theta (q_{\text{min}})^m. \quad (3.10)$$

During winter season, the ratio of  $SDR_d$  and  $SDR$  slightly increases. The first reason is the low solar elevation at noon, which extends the path length through haze layers with intensified  $SDR$  scattering. The second reason is the increase of surface albedo due to snow cover and therefore increase of  $SDR_d$  due to multiple reflection at aerosol and cloud particles. An albedo offset  $\Delta a$  was chosen for varying time periods depending on local snow cover duration characteristics for each ASRB site.

Table 3.1 gives the different values for  $\Delta q$ ,  $\Delta a$  and the season of validity at the different ASRB sites.  $\Delta q$  and  $\Delta a$  are linearly interpolated between zero and the given values in the first and last month of the given season, e.g. in October and March in Payerne. Values found for PAY, DAV and VSF were used to estimate  $\Delta q$  and  $\Delta a$  at the other ASRB stations without  $SDR_d$  measurements. The heuristic scheme to estimate  $SDR_d$  from  $SDR$  measurements is given in Appendix A.

### 3.2.3 Comparison of Estimated and Measured $SDR_d$

#### Example for Single Day in Payerne

The upper part of Figure 3.1 shows an example day in Payerne with changing middle and low clouds in the morning, and thunderstorm in the afternoon. The estimated diffuse shortwave downward radiation ( $SDR_d$  new) follows well  $SDR_d$  measured. The mean difference between  $SDR_d$  new and  $SDR_d$  measured is  $-17.4 \text{ W m}^{-2} \pm 47.6 \text{ W m}^{-2}$ . The difference between the old diffuse method ( $SDR_d$  cubic spline) and  $SDR_d$  measured is  $-24.9 \text{ W m}^{-2} \pm 47.7 \text{ W m}^{-2}$ . Parameters used to estimated  $SDR_d$  are shown in the lower part of Figure 3.1. The mean measured transmissivity  $q_{\text{avg}}$  is compared to the transmissivity limit  $q_{\text{limit}}$  for cloud-free conditions. In the morning  $q_{\text{avg}}$  regularly reaches  $q_{\text{limit}}$ , but  $SDR_d$  is large compared to cloud-free conditions due to the large values of transmissivity range  $q_r$  and  $q_{\text{std}}$  shown in lower part of

**Table 3.1:** Seasonal transmissivity offset  $\Delta q$  and albedo offset  $\Delta a$  used to estimate the diffuse short-wave downward radiation  $SDR_d$  from  $SDR$  measurements.  $SDR_d$  is calculated every two minutes with the help of the scheme given in Appendix A.

Station	$\Delta q$		$\Delta a$	
	Value	Season	Value	Season
LOM	0.07	Oct.–Mar.	0.05	Sep.–Mar.
PAY	0.07	Oct.–Mar.	0.05	Sep.–Mar.
DAV	0.10	Oct.–Mar.	0.07	Nov.–May
CIM	0.10	Oct.–Mar.	0.07	Nov.–Mar.
MAE	0.13	Oct.–Apr.	0.10	Nov.–Apr.
VSF	0.13	Oct.–Jun.	0.10	Nov.–Apr.
WFJ	0.13	Oct.–Jun.	0.10	Nov.–Apr.
EGH	0.13	Oct.–Jun.	0.10	Oct.–May
GOR	0.13	Oct.–Jun.	0.10	Oct.–May
JFJ	0.13	Oct.–Jun.	0.10	Oct.–May

Figure 3.1.  $q_{avg}$  is far below  $q_{limit}$  between 12 UTC and 13 UTC, and after 15:30 UTC, which indicates overcast conditions with  $SDR_d=SDR$ .

### Annual $SDR_d$ Comparison at Three ASRB Sites

Figure 3.2 shows the average daily ( $\pm 4$  hours around solar noon) difference of estimated minus measured  $SDR_d$  in Payerne in 2001. Both estimation methods underestimate  $SDR_d$ . However the difference of the old cubic spline method additionally shows an annual cycle with maximum differences during summer and higher variability.  $SDR_d$  differences of the new method show no obvious annual cycle, and day-to-day variability is clearly reduced. Results for all three investigated ASRB stations are given in Table 3.2. The new diffuse shortwave downward radiation estimation method presented here generally

**Table 3.2:** Mean differences of estimated minus measured  $SDR_d$  at three ASRB sites in 2001.

Station	N	New method		Cubic spline method	
		Mean W m <sup>-2</sup>	Stdev W m <sup>-2</sup>	Mean W m <sup>-2</sup>	Stdev W m <sup>-2</sup>
PAY	359	-14.6	21.5	-44.5	44.4
DAV	341	-34.0	42.9	-51.9	48.9
VSF	340	-27.4	48.7	-68.7	66.6

performs better than the old cubic spline method. Therefore, fixed shadow bands are no longer needed in the future to correct the inadvertent sun influence on  $LDR$  measurements, which prevents the accumulation of hoar frost above the instruments. It also allows to place other radiation instruments nearby without the risk of shadow coverage. As an example, the shadowband on JFJ had to be removed end of 1997 to allow for a dense alignment with other radiation instruments from MeteoSwiss. At solar noon a constant value of  $SDR_d=150$  W m<sup>-2</sup> was used at JFJ since 1997 instead of measured  $SDR_d$  values.

### $LDR$ Correction Error with New $SDR_d$ Method

As described in section 3.2.1,  $SDR_d$  is needed in Eq. 3.2 to correct the direct sun influence on  $LDR_{raw}$  measurements. To estimate the error of the new  $SDR_d$  method on  $\Delta LDR_{sun}$ , the f-correction of  $LDR$

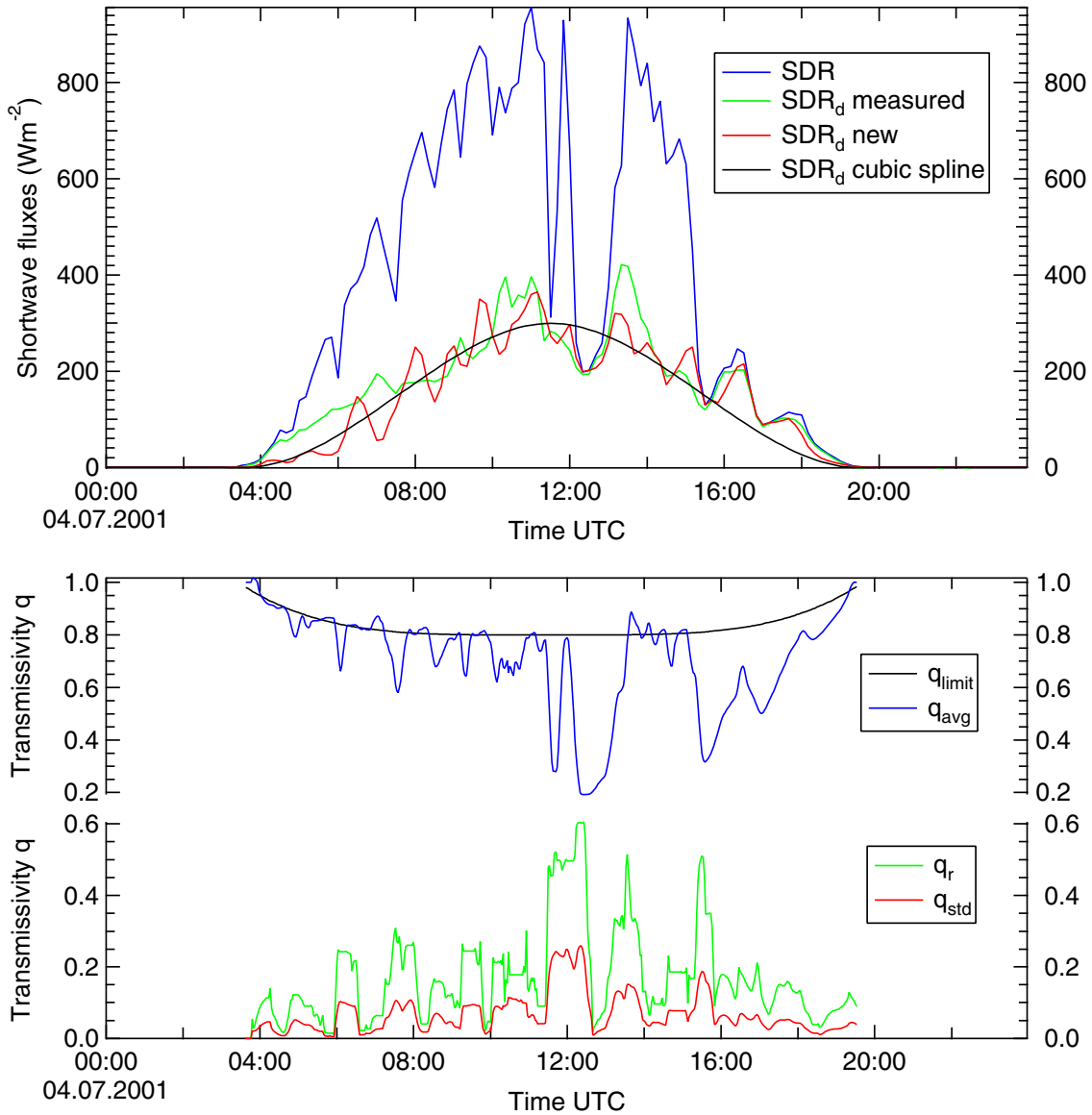


**Figure 3.1:** Example day at Payerne on 04.07.2001. The upper figure compares measured diffuse shortwave downward radiation ( $SDR_d$ ) to the old and new  $SDR_d$  estimation methods ( $SDR_d$  new,  $SDR_d$  cubic spline). The lower figure indicates the mean transmissivity ( $q_{\text{avg}}$ ) and transmissivity limit for cloud-free conditions ( $q_{\text{limit}}$ ) in the upper part, and the lower part shows the range ( $q_r$ ) and Stdev ( $q_{\text{std}}$ ) of  $q$  within the past 30 minutes.

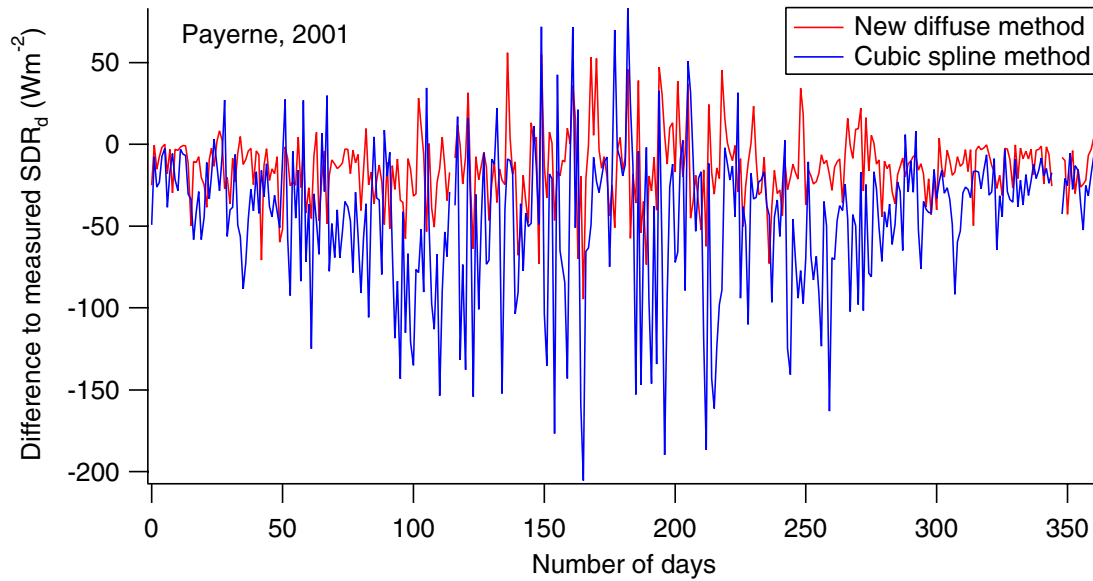


**Figure 3.2:** Annual cycle of  $SDR_d$  difference in Payerne.

was calculated with estimated and measured  $SDR_d$  values in Payerne  $\pm 4$  hours around solar noon for 2001. The mean  $LDR$  difference between the two versions of  $f$ -correction (using estimated  $SDR_d$  minus measured  $SDR_d$ ) was  $-0.16 \text{ W m}^{-2}$  with  $\pm 0.17 \text{ W m}^{-2}$  Stdev. Hence, the error on  $\Delta LDR$  introduced with the new  $SDR_d$  method remains very small.

BSRN pyrgeometers are permanently shaded with an automatic shading disc system. The mean  $LDR$  difference between ASRB and BSRN measurements after  $f$ -correction with measured  $SDR_d$  values was  $0.42 \text{ W m}^{-2}$  with  $\pm 0.78 \text{ W m}^{-2}$  Stdev, and  $0.26 \text{ W m}^{-2} \pm 0.78 \text{ W m}^{-2}$  Stdev after  $f$ -correction with estimated  $SDR_d$ . For comparison the mean ASRB - BSRN difference during nighttime (00 UTC – 03 UTC) for the same days was  $0.71 \text{ W m}^{-2}$  with  $\pm 0.74 \text{ W m}^{-2}$  Stdev. Thus, the similar annually averaged means and standard deviations for ASRB-BSRN  $LDR$  difference in night- and daytime indicate that the  $f$ -correction method is able to accurately correct the direct solar radiation on pyrgeometers. The above mentioned differences are summarized in Table 3.3.

**Table 3.3:** Statistics for  $f$ -correction of direct solar radiation with estimated and measured diffuse shortwave downward radiation ( $SDR_d$ ) and comparison of ASRB and BSRN longwave downward radiation ( $LDR$ ) measurements in Payerne for 2001.

Difference	N	Mean $\text{W m}^{-2}$	Stdev $\text{W m}^{-2}$
$\Delta LDR$ estimated–measured	359	-0.16	0.17
$LDR$ ASRB <sup>a</sup> –BSRN	359	0.42	0.78
$LDR$ ASRB <sup>b</sup> –BSRN	359	0.26	0.78
$LDR$ ASRB–BSRN <sup>c</sup>	362	0.71	0.74

<sup>a</sup> $f$ -correction calculated with  $SDR_d$  measured

<sup>b</sup> $f$ -correction calculated with  $SDR_d$  new

<sup>c</sup>Nighttime only: 00 UTC – 03 UTC

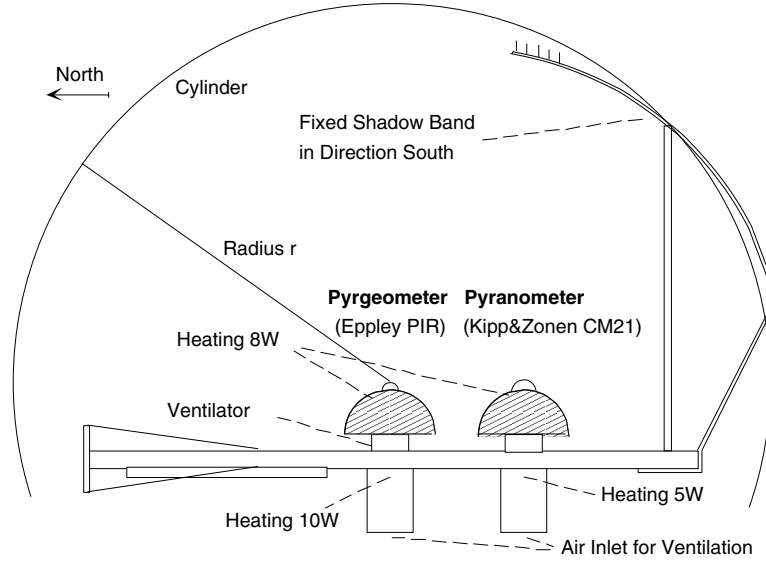


**Figure 3.3:** Standard set-up of the pyrano- and pyrgemeter and their ventilation- and heating system at each ASRB-station. The vertical fixed shadowband in direction south provides a uniform shadow during 20 min around solar noon. Envelope and radius  $r$  of the cylinder for the integration of the shadowband shielding angle are also shown.

### 3.3 Re-evaluation of ASRB Shielding Factor

Marty (2000) determines for all ASRB sites the shielding correction factor  $g$ , which accounts for shielding effects of the shadowband and other obstacles on  $LDR$  measurements (Philipona *et al.*, 1995):  $\Delta LDR = gU_{emf}$ , where  $g$  is given in  $W m^{-2} (mV)^{-1}$  and the PIR thermopile signal  $U_{emf}$  is given in mV. The value of  $g$  mainly depends on the percentage of hemisphere covered by the shadowband and other obstacles, e.g. mast.

The shielding of shadowband and mast was newly calculated for each ASRB station, and the obstacle effect on  $LDR$  estimated from nighttime measurements.

#### 3.3.1 Determination of Sky Shielding

All ASRB sites are equipped with the same shadowband set-up as shown in Figs. 3.3 and 3.4. The mean distance  $r$  between shadowband and pyrgemeter dome is about 82 cm, and shadowband width  $z$  is about 5 cm. The shadowband is approximated as a segment of a cylinder with radius  $r$  and with the pyrgemeter dome located on the cylinder axis to integrate the effective shielding angle  $\Omega_{SB}$  in sr.  $\Omega_{SB}$  is defined in cylindric coordinates as follows:

$$\Omega_{SB} = \int \cos \theta \, d\Omega, \quad (3.11)$$

$$= \int \cos \theta \frac{dA}{r^2}, \quad (3.12)$$

$$= \frac{1}{r^2} \iint \cos \theta \, r \, d\theta \, dz, \quad (3.13)$$

$$= \frac{1}{r} \int_{z_0}^{z_1} dz' \int_{\theta_0}^{\theta_1} \cos \theta' \, d\theta', \quad (3.14)$$

with the mean distance  $r$  between pyrgeometer dome and the shadowband, the zenith angle  $\theta$  and shadowband width  $z$  in cm. The minimum zenith angle  $\theta_0$  at the top of shadowband as seen from the pyrgeometer dome is  $18^\circ = \frac{\pi}{10}$ , and the maximum zenith angle  $\theta_1$  is  $90^\circ = \frac{\pi}{2}$ . Using Eq. 3.14 and the above mentioned values for  $r$ ,  $z$  and  $\theta$  we obtain  $\Omega_{\text{SB}}$  for the shadowband:

$$\Omega_{\text{SB}} = \frac{1}{r} \int_0^{5\text{cm}} dz' \int_{\frac{\pi}{10}}^{\frac{\pi}{2}} \cos \theta' d\theta', \quad (3.15)$$

$$= 0.042. \quad (3.16)$$

Thus, the shadowband shields about  $100 \frac{0.042}{\pi} = 1.3\%$  of the total hemispheric solid angle  $\Omega$ , which is equal to  $\pi$ .

Similarly, the effective shielding angle  $\Omega_{\text{M}}$  of the mast can be calculated using polar coordinates and radius  $r = 1$ :

$$\Omega_{\text{M}} = \int \cos \theta d\Omega, \quad (3.17)$$

$$= \int \cos \theta \frac{dA}{r^2}, \quad (3.18)$$

$$= \int \cos \theta d\theta d\phi, \quad (3.19)$$

$$= \int_{\phi_0}^{\phi_1} d\phi' \int_{\theta_0}^{\theta_1} \cos \theta' d\theta', \quad (3.20)$$

with aperture angle  $\phi$ ,  $\phi_0 = 0$  and  $\theta_1 = \frac{\pi}{2}$ .  $\theta_0$  and aperture angle  $\phi_1$  vary for each site depending on the height and width of the mast.

### 3.3.2 Determination of Obstacle Influence on LDR

The measured raw longwave downward radiation ( $LDR_{\text{raw}}$ ) depends on the mean radiance  $L$  emitted from the total hemispheric solid angle  $\Omega$ :

$$LDR_{\text{raw}} = \Omega L, \quad (3.21)$$

where  $\Omega$  is equal to  $\pi$ . In the presence of an obstacle,  $LDR_{\text{raw}}$  is both influenced by the mean sky radiance  $L_{\text{sky}}$  and by the mean obstacle radiances  $L_{\text{SB}}$  from the shadowband and  $L_{\text{M}}$  from the mast or Sphinx dome at the ASRB-station Jungfraujoch (JFJ):

$$LDR_{\text{raw}} = (\Omega - \Omega_{\text{SB}} - \Omega_{\text{M}})L_{\text{sky}} + \Omega_{\text{SB}}L_{\text{SB}} + \Omega_{\text{M}}L_{\text{M}}. \quad (3.22)$$

$L_{\text{SB}}$  for the shadowband is defined as:

$$L_{\text{SB}} = \frac{\sigma T^4}{\pi}, \quad (3.23)$$

where  $T$  is the air temperature. It was assumed that the temperature  $T$  of the obstacle is equal to the air temperature. For the Sphinx dome at Jungfraujoch and for the masts,  $L_{\text{M}}$  is a combination of obstacle emission and reflection of sky radiance:

$$L_{\text{M}} = \frac{\epsilon_{\text{M}}\sigma T^4}{\pi} + (1 - \epsilon_{\text{M}})L_{\text{sky}}, \quad (3.24)$$



where  $\epsilon_M = 0.95$  is the emissivity of the obstacle. The emissivity  $\epsilon_M$  is equal to 0.95 for all obstacles except for the aluminium Sphinx dome at JFJ. Due to the higher emissivity of aluminium oxide, a mean  $\epsilon_M = 0.35$  was chosen for JFJ.  $L_{\text{sky}}$  can now be determined using Eqs. 3.22, 3.23 and 3.24:

$$L_{\text{sky}} = \frac{LDR_{\text{raw}} - \frac{\sigma T^4}{\pi} (\Omega_{\text{SB}} + \epsilon_M \Omega_M)}{\pi - \Omega_{\text{SB}} - \epsilon_M \Omega_M}. \quad (3.25)$$

The shielding effect of the mast on longwave upward radiation (*LUR*) measurements is treated analogously to the shadowband effect, i.e. radiance is computed with the help of Eq. 3.23.

The obstacle influence on the measured raw longwave downward radiation ( $LDR_{\text{raw}}$ ) is corrected as follows:

$$LDR = LDR_{\text{raw}} - \Delta LDR, \quad (3.26)$$

$$= LDR_{\text{raw}} - (\Omega_{\text{SB}} \Delta L_{\text{SB}} + \Omega_M \Delta L_M), \quad (3.27)$$

with the radiance difference  $\Delta L_{\text{SB}} = L_{\text{SB}} - L_{\text{sky}}$  between shadowband and sky, and  $\Delta L_M = L_M - L_{\text{sky}}$  between mast or Sphinx dome and sky. *LDR* is the corrected longwave downward radiation further used in this work.  $\Delta LDR$  is linearly related to the measured PIR thermopile signal  $U_{\text{emf}}$  given in mV:

$$\Delta LDR = g_0 + g_1 U_{\text{emf}}. \quad (3.28)$$

$\Delta LDR$  as a function of  $U_{\text{emf}}$  was determined for each ASRB-station from all-sky nighttime  $LDR_{\text{raw}}$  measurements over several years. The shielding correction coefficients  $g_0$  given in  $\text{W m}^{-2}$  and  $g_1$  given in  $\text{W m}^{-2}/\text{mV}$  substitute the former shielding correction factor  $g$  used by *Marty* (2000). Table 3.4 summarises the effective shielding angles  $\Omega_{\text{SB}}$  for the shadowband and  $\Omega_M$  for the mast or Sphinx dome, and the shielding correction coefficients  $g_0$  and  $g_1$ . The coefficients are also given for the ASRB-Travelling Standard (ASRB-TS), which is positioned as close as possible to the ASRB instruments during field calibration. The ASRB-TS is made up of the same instruments as ASRB, i.e. Epply PIR pyrgeometer and Kipp&Zonen CM21 pyranometer. Both instruments are ventilated, but not heated. Values  $g_0$  and  $g_1$  for ASRB-TS are estimated from  $g_0$  and  $g_1$  used for the ASRB pyrgeometer. An example for in situ calibration with ASRB-TS is shown in Figure 3.4.

### 3.4 Calibration of Travelling Standard and ASRB Davos

All PIR pyrgeometers used in ASRB including the ASRB-TS are modified (*Philipona et al.*, 1995), i.e. dome temperature is measured by three dome thermistors, and the compensation battery is removed. *LDR* is calculated from the new pyrgeometer equation (*Philipona et al.*, 1995) and corrected with the help of Eq. 3.28 as follows:

$$LDR = \frac{1000 U_{\text{emf}}}{C} (1 + k_1 \sigma T_B^3) + k_2 \sigma T_B^4 - k_3 \sigma (T_D^4 - T_B^4) - (g_0 + g_1 U_{\text{emf}}), \quad (3.29)$$

where *LDR* is the irradiance in  $\text{W m}^{-2}$ ,  $U_{\text{emf}}$  is the PIR thermopile signal given in mV,  $C$  is the sensitivity factor in  $\mu\text{V}(\text{W m}^{-2})^{-1}$ ,  $T_B$  is the body-temperature in Kelvin,  $T_D$  is the dome temperature in Kelvin and  $k_1, k_2, k_3$  are correction factors.

First, correction factors  $k_1, k_2, k_3$  and sensitivity  $C$  were determined in the blackbody source at PMOD/WRC (*Philipona et al.*, 1995). The reference PIR ( $\text{PIR}_{\text{ref}}$ ) pyrgeometer (SN 31463F3) on the roof of PMOD/WRC was calibrated in the blackbody source in October 2001, and ASRB Davos PIR was calibrated in November 2002. In a second step sensitivities  $C$  of ASRB-TS and ASRB Davos were

**Table 3.4:** Effective shielding angle for shadowband ( $\Omega_{\text{SB}}$ ) and mast ( $\Omega_{\text{M}}$ ) at each ASRB-station and shielding correction coefficients  $g_0$  and  $g_1$  for ASRB pyrgeometers and ASRB Travelling Standard (ASRB-TS).

Station	$\Omega_{\text{SB}}$ sr	$\Omega_{\text{M}}$ sr	$g_{\text{ASRB}}$		$g_{\text{ASRB-TS}}$	
			$g_0$ $\text{W m}^{-2}$	$g_1$ $\text{W m}^{-2} (\text{sr}^{-1})$	$g_0$ $\text{W m}^{-2}$	$g_1$ $\text{W m}^{-2} (\text{mV}^{-1})$
Locaro-Monti	0.042	0.004	0	-3.8	0	-3.3
Payerne	0.042	0	0	-3.4	0	-3.0
Davos	0.042	0	-0.1	-3.9	0	-2.9
Davos See	0.062	0	-0.1	-5.3	0	-5.7
Davos out	0.069	0	-0.1	-7.2	0	-7.5
Cimetta	0.042	0.011	-0.1	-4.6	0	-3.8
Männlichen	0.042	0.057	-0.2	-8.3	-0.1	-8.6
SLF-Versuchsfeld	0.042	0	-0.1	-3.6	0	-1.3
Versuchsfeld out	0.069	0	-0.1	-7.2	0	-7.5
Weissfluhjoch	0.042	0.028	-0.1	-6.1	0	-5.5
Weissfluhjoch out <sup>a</sup>	0.089	0	0	-7.4	–	–
Eggishorn	0.042	0.049	-0.2	-7.2	-0.1	-7.0
Gornergrat	0.042	0.049	-0.2	-7.5	-0.1	-7.3
Jungfraujo <sup>b</sup>	0.042	0.167	-0.4	-8.9	–	–
Jungfraujo	0	0.052	0	-1.6	0	-1.6

<sup>a</sup>ASRB Travelling Standard

<sup>b</sup>until November 1997

field-calibrated with  $\text{PIR}_{\text{ref}}$  several times from 2000–03.  $\text{PIR}_{\text{ref}}$  itself participated at two International Pyrgeometer and Absolute Sky-scanning Radiometer Comparisons (IPASRC-I (*Philipona et al.*, 2001) and IPASRC-II (*Marty et al.*, 2003)), where  $\text{PIR}_{\text{ref}}$  was field-calibrated with the Absolute Sky-scanning Radiometer (*Philipona*, 2001).

Different values of  $C$  in the range of  $3\text{--}5 \mu\text{V}(\text{W m}^{-2})^{-1}$  with 0.01 increment were used to calculate  $LDR$  for ASRB-TS ( $LDR_{\text{ASRB-TS}}$ ) or for ASRB PIRs ( $LDR_{\text{ASRB}}$ ) from Eq. 3.29. The sum of the squares of the  $LDR$  differences to  $LDR_{\text{ref}}$  ( $\sum(LDR_{\text{ASRB-TS/ASRB}} - LDR_{\text{ref}})^2$ ) was minimised to find the accurate sensitivities  $C_{\text{ASRB-TS}}$  and  $C_{\text{ASRB}}$ . The shielding correction coefficients  $g_0$  and  $g_1$  for  $\text{PIR}_{\text{ref}}$  on the PMOD/WRC roof are zero.  $C_{\text{ASRB-TS}}$  was calibrated five times at Davos for cloud-free and calm nighttime conditions from 2000–03.  $C_{\text{ASRB}}$  for Davos was calibrated six times for cloud-free and calm nighttime conditions from June 2003 until February 2004. Table 3.5 gives the calibrated sensitivities  $C$  with their maximum deviation in parenthesis, and correction factors  $k_1, k_2, k_3$  used for ASRB-TS, ASRB Davos and  $\text{PIR}_{\text{ref}}$ . A maximum deviation of 0.03 for the sensitivity  $C$  corresponds to about  $0.5 \text{ W m}^{-2}$  mean all-sky  $LDR$  change.

### 3.5 Calibration of ASRB Pyrgeometers

Two different field-calibration campaigns were accomplished for ASRB instruments. A first comparison was done for a few sites in the years 1996/97 by Christoph Marty, and a second comparison was carried out by myself for all ASRB sites except Les Diablerets in the years 2000/01. ASRB and BSRN Payerne were calibrated in 2004. The strong electromagnetic field of a new transmission made the radiation

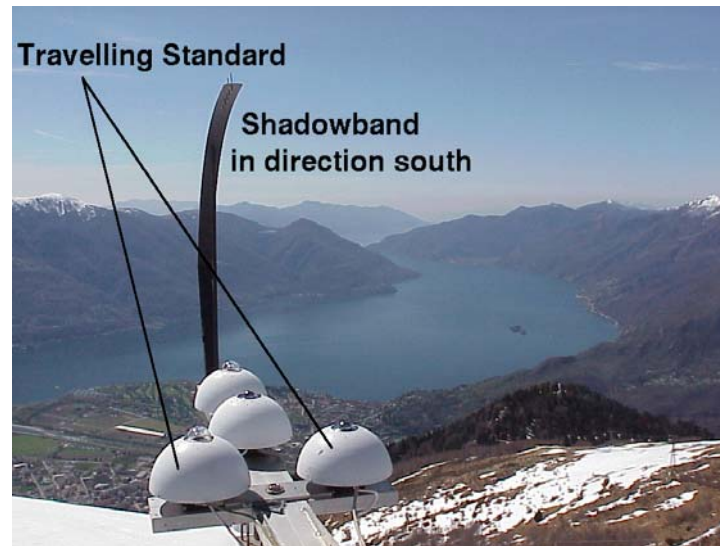


**Figure 3.4:** ASRB Travelling Standard (ASRB-TS) positioned at ASRB-site Cimetta. The ASRB-TS is made up of the same instruments and the same ventilation set-up as standard ASRB-stations. Both ASRB-TS instruments are regularly calibrated at PMOD/WRC in Davos.

**Table 3.5:** Mean sensitivity  $C$  and correction factors  $k_1, k_2, k_3$  for reference PIR pyrometer ( $PIR_{ref}$ ), ASRB Travelling Standard (ASRB-TS) PIR and ASRB Davos PIR. The maximum deviation of  $C$  from several individual calibrations is given in parenthesis.

	PIR <sub>ref</sub>	ASRB-TS	ASRB Davos
PIR coefficients	31463F3	30963F3	30324F3
$C$	3.80	4.25 (0.03)	3.34 (0.02)
$k_1$	0.0766	0.1262	-0.0031
$k_2$	0.9974	1.0007	0.9992
$k_3$	3.39	3.24	3.69

measurements difficult at Les Diablerets. Thus Les Diablerets was abandoned in October 2002. The calibration strategy was changed from the first to the second campaign. Christoph Marty visited the single stations for about one cloud-free day and night, and used the resulting short dataset for PIR calibration. This procedure allowed to calibrate several ASRB sites within a few days.

In the second field calibration campaign, the ASRB Travelling Standard (ASRB-TS) measured for about three weeks at each ASRB station, which increased the chance to measure cloud-free and calm conditions, and increased also the range of measured  $LDR$  values used for calibration of sensitivity  $C$ . The longer dataset allowed also to check for inhomogeneities due to grounding problems of the ASRB-TS.

Sensitivities  $C_{ASRB}$  were determined with the help of  $LDR$  measurements from the ASRB-TS as described in section 3.4. Table 3.6 summarises the sensitivities  $C$  found for all ASRB PIRs. The LUR instruments at the three ASRB sites Davos See, SLF-Versuchsfeld and Davos were not calibrated, and the original sensitivity and correction factors from the blackbody source were used instead.

**Table 3.6:** Individual dates for calibration of ASRB pyrgeometers and calibrated PIR sensitivity  $C$ . In parenthesis the length of time period used for calibration and time offset of the centre of the time period from midnight (0000 UTC) is given in ten minute values.

Station	Dates	$C$
Locaro-Monti	27.2.01(11,-12); 11.3.01(11,0); 15.3.01(11,-12); 3.4.01(11,-12)	3.78
ASRB Payerne	15.3.04(27,-18); 16.3.04(27,12); 17.3.04(27,12); 18.3.04(27,-18)	4.28
BSRN Payerne <sup>a</sup>	15.3.04(27,-18); 16.3.04(27,12); 17.3.04(27,12); 18.3.04(27,-18)	4.05
Cimetta	14.4.01(11,-12); 17.4.01(11,6); 23.4.01(11,-6); 27.4.01(7,-24)	3.64
Männlichen	10.7.01(11,6); 23.7.01(11,-12)	3.72
SLF-Versuchsfeld	7.7.00(27,-12); 17.7.00(27,12); 22.7.00(27,0); 31.7.00(27,12)	3.75
Weissfluhjoch	17.6.00(7,15); 20.6.00(7,6)	3.39
Eggishorn	20.6.01(11,6); 3.7.01(7,0)	3.90
Gornergrat	23.5.01(11,12); 30.5.01(11,-6); 4.6.01(11,6)	3.68
Jungfrauoch	25.7.01(11,-9); 26.7.01(11,-6); 13.8.01(11,6); 14.8.01(7,12)	3.93

<sup>a</sup>Serial No. 30333F3

### 3.5.1 Evaluation of $LDR$ Data from First Field Calibration Campaign

The ASRB pyrgeometers at Eggishorn, Gornergrat and Männlichen were calibrated in situ a first time in 1997, and SLF-Versuchsfeld in 1996. ASRB  $LDR$  measurements from calm and cloud-free nighttime conditions were compared to Travelling Standard  $LDR$  data using Eq. 3.29 and the according sensitivities  $C$  from Tabs. 3.5 and 3.6. Between four and seven hours of  $LDR$  measurements were available for comparison at each site. Mean  $LDR$  differences are listed in Table 3.7.  $LDR$  at Männlichen was slightly disturbed most probably due to ASRB-TS grounding problems. The results in Table 3.7 indicate that ASRB  $LDR$  measurements by modified PIR pyrgeometers remained very stable for several years, which is already shown by *Philipona et al.* (1998) for other modified PIR pyrgeometers.

**Table 3.7:** Mean  $LDR$  difference for data obtained from the first field-calibration campaign.  $LDR$  was calculated with sensitivities  $C$  for ASRB PIRs and ASRB Travelling Standard (ASRB-TS) from Tabs. 3.5 and 3.6.

Station	Date UTC	Difference to ASRB-TS $W m^{-2}$
Männlichen	19.9.97 0030–0510	0.9
SLF-Versuchsfeld	10/11.9.96 2254–0434	0
Eggishorn	17/18.9.97 2234–0314	-0.3
Gornergrat	15/16.9.97 2102–0442	-0.4

## 3.6 Summary

The shielding effect of ASRB shadowband and other obstacles, e.g. mast, was re-evaluated, and the former shielding correction factor  $g$  redefined as a linear equation of the PIR thermopile signal  $U_{emf}$ . First, the ASRB Travelling Standard (ASRB-TS) pyrgeometer was characterised in the PMOD/WRC black-body source, and sensitivity  $C_{ASRB-TS}$  field-calibrated with the reference pyrgeometer on PMOD/WRC roof. Secondly, all ASRB PIR sensitivities except for Davos were calibrated with ASRB-TS in 2000/01.

---

A comparison of ASRB and ASRB-TS *LDR* at four ASRB-stations using new sensitivities and data from the first field-calibration campaign in 1996/97 revealed that *LDR* measurements within ASRB were stable for at least five or six years.



## Chapter 4

# Cloud Amount Detection

### 4.1 Introduction

Methods for the separation of cloud-free and cloudy-sky conditions are necessary to quantify the cloud effect (CE) on measured shortwave and longwave downward radiation (*Philipona et al.*, 2004b). *Marty and Philipona* (2000) presented the Clear-Sky Index (*CSI*) method based on longwave downward radiation, temperature and relative humidity at screen level height to distinct between cloud-free and cloudy-sky 24 hours a day. Comparisons of *CSI* estimates and optical observations at several ASRB stations revealed a systematic underestimation of cloud-free situations by *CSI* during night- and winter-time. Hence, an enhanced version of *CSI* was developed to reduce the mentioned *CSI* cloud-free biases. Furthermore, the enhanced *CSI* version could also be applied to develop an automatic real-time cloud amount detection system, which may be of interest for meteorological services.

Optical observations are still the main source for cloud cover information at the surface worldwide. An increasing number of airports, however, are nowadays equipped with automated surface observation systems (ASOS), where cloud height and cloud cover are assessed by a ceilometer (*Nadolski*, 1995). Ceilometers have the major disadvantage that they are often operated in a fixed direction only. *Aviolat et al.* (1998) improved ceilometer-based cloud amount estimations with the help of longwave downward radiation measurements processed by a neural network. An automatic cloud cover detection method based on IR pyrometers (8–14  $\mu\text{m}$ ) scanning the whole sky within 30 seconds was proposed by *Gillotay et al.* (2002). Hemispheric sky imager (*Long and DeLuisi*, 1998, *Beaubien and Bisberg*, 1999, *Feister et al.*, 2000) have the disadvantage of high equipment investment and extensive data processing. Sky imager systems and other cloud detection methods based on shortwave flux modification by the presence of clouds (*Long and Ackermann*, 2000) are available only for daytime observations.

The Automatic Partial Cloud Amount Detection Algorithm (APCADA) is introduced here, which provides a simple and robust real-time cloud detection method available 24 hours a day. APCADA is based on an enhanced version of the Clear-Sky Index (*CSI*) (*Marty and Philipona*, 2000), which is primarily used to extract cloud-free situations for radiative climate research. Longterm series of longwave downward radiation measurements from several sites worldwide provided an extensive dataset to implement and verify APCADA for different climate zones.

### 4.2 Observational Data

#### 4.2.1 Observed Irradiances

Radiation and meteorological measurements at screen level height from five ASRB (see section 2.1) and two BSRN stations (see section 2.2) were used to develop and implement APCADA. Ten minutes

averages of longwave downward radiation (*LDR*), temperature and relative humidity were applied for investigation. Table 4.1 gives an overview of the investigated sites.

**Table 4.1:** Radiation stations, shortname, radiation network, used dataset, altitude and coordinates.

Station	Abr.	Type	Dataset	Altitude	Coordinates
Kwajalein	KWA	BSRN	2000–2001	10 m	8°43'N, 167°44'E
Ny Ålesund	NYA	BSRN	1999–2001	42 m	78°56'N, 11°57'E
Locarno-Monti	LOM	ASRB	1996–2002	370 m	46°10'N, 8°47'E
Payerne	PAY	ASRB	1996–2002	490 m	46°49'N, 6°57'E
Davos	DAV	ASRB	1996–2002	1610 m	46°49'N, 9°51'E
Weissfluhjoch	WFJ	ASRB	1996–2002	2690 m	46°50'N, 9°49'E
Jungfrauoch	JFJ	ASRB	1996–2002	3580 m	46°33'N, 7°59'E

### 4.2.2 Synoptic Observations

Automatic cloud amount estimations were compared to optical observations at the surface, which are hereinafter referred to as “synoptic observations” (*WMO*, 1993).

At the ASRB sites Payerne (PAY), Locarno-Monti (LOM) and Jungfrauoch (JFJ) synoptic observations are taken every three hours, but only from 06 UTC to 18 UTC at LOM and JFJ. At Davos (DAV) and Weissfluhjoch (WFJ) simplified synoptic observations including total cloud amount and estimations of the optical density of clouds are made every six hours from 06 to 18 UTC.

Synoptic observations are obtained every six hours at the BSRN locations Kwajalein (KWA) and Ny Ålesund (NYA), except midnight (00 UTC) at NYA. Informations about total cloud cover, partial cloud cover and cloud type were used.

The exact synoptic observation time used in Switzerland is 30 to 40 minutes earlier than the designated synoptic hours, e.g. from 1120 to 1130 UTC for 12 UTC observation. Therefore, observations were compared with an APCADA estimated partial cloud amount based on 10 minutes averages of *LDR*, temperature and humidity from 1120 to 1130 UTC. Synoptic observations are taken 10 minutes later in NYA, and 30 minutes later in KWA, i.e. from 1150 to 1200 UTC.

Nighttime synoptic observations are used only if moon elevation is higher than 10 degrees and sun elevation higher than -9 degrees, and moon phase is at least half moon at the same time. This guarantees acceptable light conditions for the observer (*Hahn et al.*, 1995).

## 4.3 Requirements to Automatic Cloud Amount Detection

First of all the concept of “cloud-free” sky has to be introduced here. The *CSI*-method by *Marty and Philipona* (2000) uses the term “clear-sky” to indicate situations without the appearance of clouds. However a cloudless sky still can have strongly varying transmission properties both for short- and longwave radiation mostly due to different aerosol and relative humidity conditions. Measurements of aerosol properties are sparse and often restricted to visible wavelengths. Therefore our definition of a cloud-free sky bases on measured *LDR*, air temperature and humidity at the surface only:

**Cloud-free sky:** *Cloud-free sky conditions are represented by a lack of any detectable signatures in measured LDR caused by clouds, i.e. increased variability and/or increased LDR compared to LDR parametrised from temperature and humidity at screen level height.*



*LDR* variability is further discussed in section 4.4.1 and *LDR* parametrisation is described in section 4.4.2.

Detection of total cloud cover is a standard task for synoptic stations. Are all clouds detectable by *LDR* measurements at the surface? For cloud-free situations about 60% of measured *LDR* stems from the first 100 m, and about 90% from the first 1000 m air column above the surface (Ohmura, 2001, Philipona *et al.*, 2004a). Thus high clouds (cirrus, cirrostratus and cirrocumulus) are expected to have a small effect on *LDR* at the Earth's surface due to large distance and cold emittance temperature. Influence of cirrus clouds on *LDR* in Payerne was investigated with the radiative transfer model MODTRAN v4.0 (Berk *et al.*, 2000) using MODTRAN cirrus cloud model number 18 and cloud-free radiosonde profiles measured in Payerne. The cirrus layer in the model covered the whole sky with 1 km layer thickness and cloud base at 6 km a.s.l. Modeled hemispherically integrated effect on *LDR* was  $4 \text{ W m}^{-2}$  for summer, respectively  $5 \text{ W m}^{-2}$  for winter atmospheres. Hence, *LDR* measured at the Earth's surface is marginally affected by high clouds. Therefore the total cloud amount without high clouds was further investigated. Total cloud amount without high clouds is hereinafter referred to as "partial cloud amount" (*PCA*). *PCA* is not directly observed and has to be inferred from other synoptical observations (WMO, 1993). Such a calculation can be done using information like cloud type ( $C_L$ ,  $C_M$  and  $C_H$  for low, middle and high clouds respectively), total cloud amount ( $N$ ) and partial cloud cover ( $N_h$ ).  $N_h$  is defined as the cloud amount of  $C_L$  or, if no  $C_L$  clouds are present, of  $C_M$  clouds. Cloud type equal zero means that no clouds were observed on the according level. As an example, *PCA* is determined from the following observations in Payerne at 12 UTC on 6 April, 1999:  $N=3$  octas<sup>1</sup>,  $N_h=2$ ,  $C_L=0$ ,  $C_M=3$  and  $C_H=2$ .  $N_h=2$  corresponds directly to the amount of  $C_M$  clouds, because  $C_L$  clouds are missing. Thus, *PCA* is equal to  $N_h$ , i.e. 2 octas. However, *PCA* could not be determined for some cases with 3 different cloud layers. A respective example was observed 3 hours later at 15 UTC:  $N=5$ ,  $N_h=1$ ,  $C_L=5$ ,  $C_M=4$  and  $C_H=2$ . The amount of  $C_L$  clouds is known ( $N_h=1$ ), but the rest of  $N-N_h=4$  octas cloud amount cannot be clearly separated to the both remaining cloud layers ( $C_M$  and  $C_H$ ). Thus, *PCA* remains undefined for this case. *PCA* could be clearly deduced from synoptic observations for about 90% of all daytime (12 UTC) and for more than 95% of all nighttime (00 UTC) cases at all sites except KWA, where only about 40% of all possible *PCA* cases could be calculated.

## 4.4 Automatic Partial Cloud Amount Detection

### 4.4.1 Variability of Longwave Downward Radiation

Cloud-free and totally overcast situations, e.g. fog, are characterised by small *LDR* variations. *LDR* measured at the surface over a period of one hour is strongly influenced by passing broken clouds. To measure *LDR* variability, measurements of the past hour are linearly interpolated, and standard deviation of the residuals to the linear regression (Stdev *LDR*) is calculated. The comparison of Stdev *LDR* with observed *PCA* in Payerne shown in Figure 4.1(a) indicates that *LDR* variability is useful to separate broken cloud from cloud-free or overcast situations.

### 4.4.2 The Improved Clear-Sky Index

The Clear-Sky Index (*CSI*) (Marty and Philipona, 2000) is intended to separate cloudy sky from cloud-free situations based on *LDR*, screen level temperature and water vapour pressure at the Earth's surface.

---

<sup>1</sup>One octa means one-eighth of visible sky surface covered by clouds

The *CSI* is defined as:

$$CSI = \frac{\epsilon_A}{\epsilon_{AC}}, \quad (4.1)$$

$$\epsilon_A = \frac{LDR}{\sigma T^4}, \quad (4.2)$$

$$\epsilon_{AC} = \epsilon_{AD} + (k + 2\sigma_f) \left( \frac{e}{T} \right)^{1/8}, \quad (4.3)$$

where  $\sigma$  is the Stefan-Boltzmann constant,  $T$  the air temperature given in Kelvin,  $\epsilon_{AD}$  an altitude dependent emittance of a completely dry atmosphere,  $e$  water vapour pressure (Pa),  $k$  a location dependent coefficient and  $\sigma_f$  the accordant standard deviation. Water vapour pressure  $e$  is calculated from air temperature  $t_a$  and relative humidity  $RH$  using the following equations:

$$e = \frac{RH}{100} e_s, \quad (4.4)$$

$$e_s = 6.1121 \exp \left( \frac{17.502 t_a}{t_a + 240.97} \right). \quad (4.5)$$

The empirical equation for the saturated water vapour pressure  $e_s$  given in Pa is valid from  $-30^\circ\text{C}$  to  $50^\circ\text{C}$  (Buck, 1981). The air temperature  $t_a$  is given in  $^\circ\text{C}$ , and relative humidity  $RH$  is given in %.  $k$  is fitted to a set of manually selected cloud-free cases. The corresponding confidence level  $2\sigma$  is added to  $k$  in order to include most of the cloud-free situations.  $\epsilon_A$  indicates the apparent emissivity of the sky, and  $\epsilon_{AC}$  an empirical apparent cloud-free emittance.  $CSI \leq 1$  means cloud-free conditions, and  $CSI > 1$  cloudy sky (Marty and Philipona, 2000). Comparisons with synoptic observations revealed that the application of *CSI* during nighttime underestimates the number of cloud-free situations. Further investigations of cloud-free cases with Payerne radiosonde data showed that high *CSI* values are correlated ( $r \approx 0.6$ ) with lapse rate  $\gamma$ , i.e. temperature inversions, near the surface during night- and daytime. Thus, variations of  $\gamma$  with time ( $\gamma(t)$ ) have to be considered for the calculation of *CSI*. However, very few radiation sites regularly measure  $\gamma(t)$ . Further investigations showed that diurnal and annual cycle of  $\gamma(t)$  can be approximated as a periodical function:

$$\gamma(t) = \gamma_0 + \gamma_{\text{amp}} \cos \left( \omega t - \frac{\pi}{4} \right), \quad (4.6)$$

with  $\gamma_0$  the average and  $\gamma_{\text{amp}}$  the amplitude of  $\gamma$ , and  $\omega = 2\pi/P$  with period  $P = 1\text{yr}$  or  $P = 1\text{d}$ . Maximum of  $\gamma(t)$  lags behind maximum solar insolation with approximately  $P/8$  phase shift, i.e. 3 hours, respectively 1.5 months for the diurnal and annual cycle. Thus, we defined  $k$  in Eq. (4.3) as a function of  $\gamma(t)$  and accordingly replaced  $k$  by  $k = k[\gamma(t)] = k(t)$ :

$$k(t) = k_0 + k_{\text{amp}} \cos \left( \omega t - \frac{\pi}{4} \right), \quad (4.7)$$

with  $k_0 = \frac{k_{\text{max}} - k_{\text{min}}}{2}$  and  $k_{\text{amp}} = k_{\text{max}} - k_0$ . Analogous, the constant confidence level  $2\sigma$  in Eq. (4.3) was replaced with a time dependent shift function  $\Delta k(t)$ :

$$\Delta k(t) = \Delta k_0 + \Delta k_{\text{amp}} \cos \left( \omega t - \frac{\pi}{4} \right), \quad (4.8)$$

with  $\Delta k_0 = \frac{\Delta k_{\text{max}} - \Delta k_{\text{min}}}{2}$  and  $\Delta k_{\text{amp}} = \Delta k_{\text{max}} - \Delta k_0$ . Further, we decided to set back the exponent to the original value of  $1/7$  (Brutsaert, 1975) after evaluating fits of Eq. (4.3) to measured cloud-free

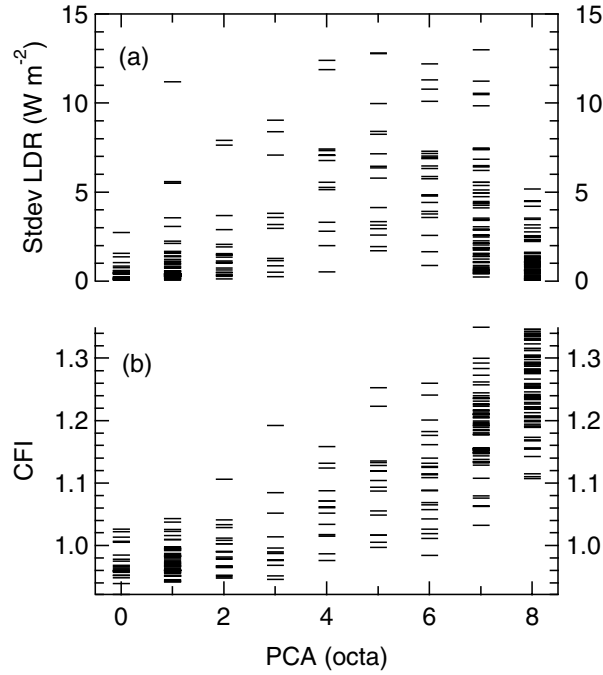


**Figure 4.1:** Variability of longwave downward radiation within the past hour (*Stdev LDR*) (a) and *Cloud-Free Index (CFI)* (b) plotted against partial cloud amount (*PCA*) for 322 daytime observations (12 UTC) in Payerne in 2001. *CFI* allows to separate between cloud-free (0 or 1 octa) and overcast (7 or 8 octas) situations. Compared to cloud-free or overcast conditions, broken cloud amounts (2 to 6 octas) are both characterised by different *CFI* values and large *LDR* variability.

emissivities at several radiation sites. Thus, the apparent cloud-free emissivity  $\epsilon_{AC}$  in Eq. (4.3) is now formulated as:

$$\epsilon_{AC} = \epsilon_{AD} + \left[ k(t) + \Delta k(t) \right] \left( \frac{e}{T} \right)^{1/7}. \quad (4.9)$$

The modified *CSI* using Eq. (4.9) is called *Cloud-Free Index (CFI)*:

$$CFI = \frac{\epsilon_A}{\epsilon_{AC}}. \quad (4.10)$$

Figure 4.1(b) shows how *CFI* can be used to separate cloud-free from overcast observations:  $CFI \leq 1$  normally indicates cloud-free conditions, and  $CFI > 1$  cloudy sky.

#### 4.4.3 Determination of Site Specific Functions $k(t)$ and $\Delta k(t)$

In order to find  $k(t)$  and  $\Delta k(t)$  (Eqs. (4.7) and (4.8)), single values of  $k$  are fitted at the diurnal and annual minimum and maximum of the periodical function  $\gamma(t)$ , i.e. afternoon ( $k_{\text{day}}$ ) and early morning ( $k_{\text{night}}$ ) for diurnal, and Jun.–Sep. ( $k_{\text{summer}}$ ) and Dec.–Mar. ( $k_{\text{winter}}$ ) for annual extrema in the northern hemisphere, and vice versa for the southern hemisphere. Hence, four different values of  $k$  ( $k_{\text{day,summer}}$ ,  $k_{\text{night,summer}}$ ,  $k_{\text{day,winter}}$ ,  $k_{\text{night,winter}}$ ) and for  $\Delta k$  ( $\Delta k_{\text{day,summer}}$ ,  $\Delta k_{\text{night,summer}}$ ,  $\Delta k_{\text{day,winter}}$ ,  $\Delta k_{\text{night,winter}}$ ) have to be fitted to measured cloud-free data to determine  $k(t)$  and  $\Delta k(t)$ .

### Annual Cycle of $k$ and $\Delta k$

We define the annual cycle (1. Jan. – 31. Dec.) of  $k$  for daytime ( $k_{\text{day}}$ ) according to Eq. (4.7):

$$k_{\text{day}} = \bar{k}_{\text{day}} + k_{\text{day,amp}} \cos\left(\omega t - \frac{\pi}{4}\right), \quad (4.11)$$

with  $\bar{k}_{\text{day}} = \frac{k_{\text{day,summer}} + k_{\text{day,winter}}}{2}$  the annual average and  $k_{\text{day,amp}} = k_{\text{day,winter}} - \bar{k}_{\text{day}}$  the annual amplitude of  $k$  for daytime, and  $\omega = 2\pi/P$  with period  $P = 365$  d or  $P = 366$  d. Analogous, we define the annual cycle of shift function  $\Delta k$  for daytime using Eq. (4.8):

$$\Delta k_{\text{day}} = \overline{\Delta k}_{\text{day}} + \Delta k_{\text{day,amp}} \cos\left(\omega t - \frac{\pi}{4}\right), \quad (4.12)$$

with  $\overline{\Delta k}_{\text{day}} = \frac{\Delta k_{\text{day,summer}} + \Delta k_{\text{day,winter}}}{2}$  the annual average and  $\Delta k_{\text{day,amp}} = \Delta k_{\text{day,winter}} - \overline{\Delta k}_{\text{day}}$  the annual amplitude of  $\Delta k$  for daytime. The same definitions are used also for the annual cycles of  $k$  and  $\Delta k$  for nighttime ( $k_{\text{night}}$ ).

### Diurnal Cycle of $k$ and $\Delta k$

In order to calculate the diurnal cycle (0010 Local Time (LT) – 2400 LT) of  $k = k(t)$ , current values out of the annual cycles of  $k_{\text{day}}$  (Eq. (4.11)), and  $k_{\text{night}}$  on the actual day  $i$  were applied:

$$k(t) = \bar{k}_i + k_{i,\text{amp}} \cos\left(\omega t - \frac{\pi}{4}\right), \quad (4.13)$$

with  $\bar{k}_i = \frac{k_{i,\text{night}} + k_{i,\text{day}}}{2}$  the daily average and  $k_{i,\text{amp}} = k_{i,\text{night}} - \bar{k}_i$  the daily amplitude of  $k$ , and  $\omega = 2\pi/P$  with period  $P = 144$  ten minutes values.

The diurnal cycle (0010 LT – 2400 LT) of  $\Delta k$  was calculated analogous:

$$\Delta k(t) = \overline{\Delta k}_i + \Delta k_{i,\text{amp}} \cos\left(\omega t - \frac{\pi}{4}\right), \quad (4.14)$$

with  $\overline{\Delta k}_i = \frac{\Delta k_{i,\text{night}} + \Delta k_{i,\text{day}}}{2}$  the daily average and  $\Delta k_{i,\text{amp}} = \Delta k_{i,\text{night}} - \overline{\Delta k}_i$  the daily amplitude of  $\Delta k$ .

#### 4.4.4 Example Fit of $k$ and $\Delta k$

We applied three successive years (1999–2001) to obtain the different  $k$ - and  $\Delta k$ -values for each radiation site except KWA, where  $CFI$  could be calculated only for the period 2000–2001. To fit  $k_{\text{day,winter}}$  and  $\Delta k_{\text{day,winter}}$  at WFJ, surface measurements of  $LDR$ , temperature and humidity were used three hours ( $\pi/4$ ) after the average sun noon time at 1230 LT in Switzerland.

In the first step, a first guess of 0.480 was chosen for  $\left[k(t) + \Delta k(t)\right]$  in Eq. (4.9) and  $CFI$  was computed using Eqs. (4.9), (4.2) and (4.10). Secondly,  $\text{Stdev } LDR$  was calculated over 2 hours ( $\pm 1$  hour) around 1530 LT ( $\text{Stdev } LDR_{2h}$ ) and  $CFI$  was plotted for all situations with  $\text{Stdev } LDR_{2h} \leq 1$   $\text{W m}^{-2}$  shown in Figure 4.2. Overcast and cloud-free situations are clearly separated by different  $CFI$  values. Thirdly, an upper  $CFI$  limit had to be chosen to exclude all overcast cases and outliers. Outliers are single points with at least 0.01 units distance to the next lower group of points (three and more points). Three outliers are indicated in Figure 4.2. For this example, an upper  $CFI$  limit of 0.99 was chosen to extract the cloud-free cases. From the remaining cases, the apparent cloud-free emissivities  $\epsilon_{AC}$  were plotted against the ratio of water vapour pressure and absolute temperature ( $e/T$ ) in Figure 4.3. Eq. (4.9) with  $\Delta k(t) = 0$  was fitted as  $y$  against  $e/T$ . The value  $k_{\text{day,winter}} = 0.413$  was found for this case (Fig. 4.3).  $\Delta k$  for a single fit is calculated using Eq. (4.9) and the emissivity difference between

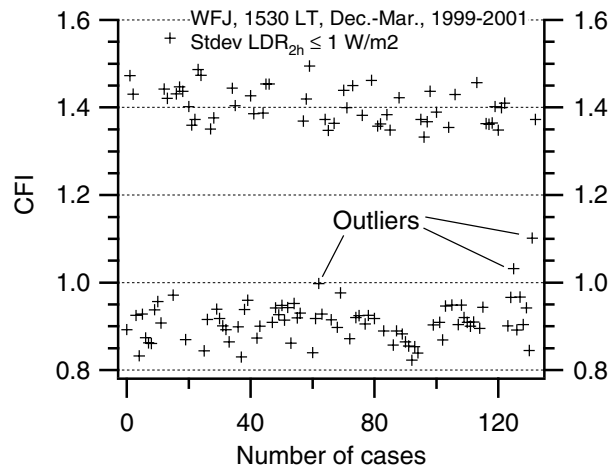


**Figure 4.2:** Calculated Cloud-Free Index (CFI) values plotted for daytime (1530 LT) winter cases with low variability of longwave downward radiation over two hours ( $\text{Stdev LDR}_{2\text{h}} \leq 1 \text{ Wm}^{-2}$ ) at the ASRB station Weissfluhjoch. Cases with CFI values around 1 indicate cloud-free, and cases with  $\text{CFI} \gg 1$  totally overcast conditions.

$y$  and the upper 90% confidence level ( $y_1$ ) of the function fit at the average value of  $e/T = 0.80$  (Fig. 4.3):

$$\Delta k = \frac{\epsilon_{\text{AC},y_1} - \epsilon_{\text{AC},y}}{(e/T)^{1/7}}. \quad (4.15)$$

$\Delta k_{\text{day,winter}} = 0.043$  was calculated for this case.

A dataset of at least 20 cloud-free cases is recommended to fit  $k$  and  $\Delta k$  for each season and daytime. Values of  $\epsilon_{\text{AD}}$ ,  $k$  and  $\Delta k$  for all used radiation sites are given in Tables 4.2 and 4.3.

**Table 4.2:** Station shortname, apparent emissivity  $\epsilon_{\text{AD}}$  of completely dry atmosphere, factors  $k$  and  $\Delta k$  fitted for cloud-free summer cases from Jun.–Sept., 1999–2001.

Sta	$\epsilon_{\text{AD}}$	Summer (Jun.–Sep.)			
		Day		Night	
		$k$	$\Delta k$	$k$	$\Delta k$
KWA	0.23	0.459	0.024	0.477	0.015
NYA	0.23	0.441	0.028	0.449	0.029
LOM	0.23	0.429	0.020	0.458	0.019
PAY	0.23	0.431	0.015	0.475	0.015
DAV	0.22	0.421	0.016	0.457	0.014
WFJ	0.21	0.412	0.017	0.428	0.027
JFJ	0.20	0.403	0.042	0.430	0.040

#### 4.4.5 Estimation of Partial Cloud Amount

PCA in octas is estimated every 10 minutes using CFI and Stdev LDR, which is calculated over the past hour. A heuristic set of rules was formulated to estimate PCA for a large number of 12 UTC synoptic observations in Payerne from 1996–2001. The set of heuristic rules is given in Table 4.4. Using Eq.

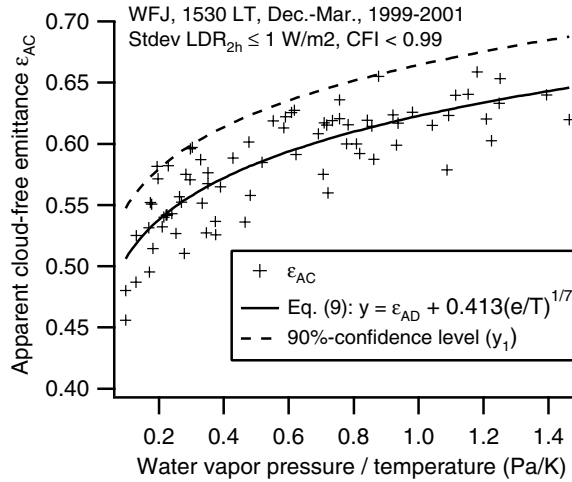


**Figure 4.3:** Apparent emittance of all cases in Fig. 4.2 with  $CFI < 0.99$  as a function of screen level water vapour pressure and temperature. The curve fit represents Eq. (4.9) with  $\Delta k = 0$  and is used to determine  $k$ .

**Table 4.3:** Station shortname, apparent emissivity  $\epsilon_{AD}$  of completely dry atmosphere, factors  $k$  and  $\Delta k$  fitted for cloud-free cases from Dec.–Mar., 1999 – 2001.

Sta	$\epsilon_{AD}$	Winter (Dec.–Mar.)			
		Day		Night	
		$k$	$\Delta k$	$k$	$\Delta k$
KWA	0.23	0.452	0.015	0.474	0.018
NYA	0.23	0.474	0.041	0.479	0.051
LOM	0.23	0.433	0.022	0.459	0.022
PAY	0.23	0.442	0.022	0.481	0.034
DAV	0.22	0.425	0.024	0.458	0.036
WFJ	0.21	0.413	0.043	0.425	0.042
JFJ	0.20	0.395	0.052	0.414	0.053

(4.10) variable  $z$  is defined as:

$$\begin{aligned}
 z &= CFI_{\max} - CFI_{\text{cloud-free}} \\
 &= \frac{\epsilon_{\text{overcast}}}{\epsilon_{AC}} - \frac{\epsilon_{AC}}{\epsilon_{AC}}
 \end{aligned} \tag{4.16}$$

with  $\epsilon_{\text{overcast}} = 1$ . Three threshold limits  $1 + az$ ,  $1 + bz$  and  $1 + cz$  are used to divide  $z$  into different sectors.

A score index was used to optimise the different threshold limits for Stdev  $LDR$  and factors  $a$ ,  $b$  and  $c$  (Tab. 4.4) to get a maximum percentage of cases with minimised difference between estimated and observed  $PCA$ . Score index is defined as  $\text{Score} = 100 \frac{n_{(\pm 1 \text{ octa})}}{n}$  (%), where  $n_{(\pm 1 \text{ octa})}$  is the number of cases with maximum one octa difference between estimation and observation, and  $n$  the total number of cases. Score is defined analogous for maximum zero and two octas difference.

Factors  $a$ ,  $b$  and  $c$  used for  $CFI$  threshold limits were optimized using the score index for maximum one octa  $PCA$  difference. Values found specifically for Payerne are  $a = 0.12$ ,  $b = 0.21$ ,  $c = 0.38$ , but further explorations showed that these values were applicable at all investigated sites. The scheme

using *CFI*, *Stdev LDR* and the heuristic set of rules for estimating *PCA* is called Automatic Partial Cloud Amount Detection Algorithm (APCADA).

**Table 4.4:** Scheme for estimating partial cloud amount (*PCA*) using Cloud-Free Index (*CFI*) and variability of longwave downward radiation (*Stdev LDR*).

<i>CFI</i> ( <i>x</i> )	<i>Stdev LDR</i> ( <i>y</i> ) ( $\text{W m}^{-2}$ )	<i>PCA</i> (octa)
$x \leq 1$	$y \leq 0.5$	0
$x \leq 1$	$0.5 < y \leq 2$	1
$x \leq 1$	$y > 2$	2
$1 < x \leq (1 + az)$	$y \leq 1$	1
$1 < x \leq (1 + az)$	$1 < y \leq 2$	2
$1 < x \leq (1 + az)$	$y > 2$	3
$(1 + az) < x \leq (1 + bz)$	$y \leq 1$	2
$(1 + az) < x \leq (1 + bz)$	$y > 1$	4
$(1 + bz) < x \leq (1 + cz)$	$y \leq 4$	5
$(1 + bz) < x \leq (1 + cz)$	$y > 4$	6
$x > (1 + cz)$	$y > 8$	6
$x > (1 + cz)$	$2 < y \leq 8$	7
$x > (1 + cz)$	$y \leq 2$	8

## 4.5 Results for APCADA Cloud Cover Estimation

### 4.5.1 Comparison of Partial Cloud Amount at ASRB Station Payerne

Observed and APCADA estimated partial cloud amount (*PCA*) were first compared in Payerne for the years 1996–98 to have a dataset independent from the *CFI* calibration period 1999–2001. Figure 4.4 shows different scores for maximum zero, one and two octas difference between estimated and observed *PCA*. Average score for fully matched cases is 53.8% (45.4%–60.6%), and 87.2% (85.2%–88.6%), respectively 94.4% (93.8%–95.3%) for maximum one or two octas difference. Thus, about 95% of all *PCA* estimations agree within  $\pm 2$  octas with synoptic observations during day- and nighttime.

Table 4.5 shows the distribution of estimated and observed *PCA* in Payerne for 12 UTC from 1996–2002. About 45% of all observed or estimated cases are seven or eight octas (overcast), and 26% are zero or one octa (cloud-free or almost cloud-free). Hence, about 30% of all observed cases show 2–6 octas *PCA*. The respective APCADA estimates vary strongly, e.g. they range from zero to seven octas for three octas observed *PCA*. However, only 26 cases (1.1%) show four or more octas difference between APCADA estimation and synoptic observation.

Observed and APCADA estimated *PCA* are shown in Figure 4.5 for a single day in Payerne. The curve of APCADA estimates agrees well with synoptic observations of *PCA*. Four observations are fully matched, three have one octa difference, and one observation shows two octas difference.

### 4.5.2 Performance of APCADA in Different Climate Regions

APCADA was tested at radiation stations on different altitudes in the Alps and for one arctic and one tropical site. Table 4.6 gives the scores for maximum one octa *PCA* difference between estimation and observation. All values are greater than 80%, except for KWA, where the minimum score is about 70%.

**Table 4.5:** Contingency matrix of observed and estimated partial cloud amount (PCA) for Payne given in octas. Percentage of observed PCA for 2272 (=100%) cases at 12 UTC (13 LT) and percentage distribution of estimated PCA for each observed octa.

Observed	%	Estimated								
		0	1	2	3	4	5	6	7	8
0	8.2	67.4	24.1	3.7	1.6	0.5	2.2	0	0.5	0
1	17.9	61.3	28.3	7.9	1.7	0.3	0.5	0	0	0
2	7.4	20.3	40.1	24.0	9.6	3.0	1.2	1.2	0.6	0
3	5.2	9.4	18.8	27.3	20.5	12.0	2.6	6.0	3.4	0
4	4.3	0	13.1	23.2	25.3	15.2	4.0	14.2	4.0	1.0
5	3.3	0	2.7	10.8	12.2	12.2	13.5	24.3	20.3	4.0
6	6.1	0	0	2.9	8.6	10.8	7.2	38.1	23.0	9.4
7	17.4	0	0	0	1.0	1.5	2.8	14.4	45.1	35.2
8	30.2	0	0	0	0	0	1.3	1.0	19.5	78.2

Seasonal score rates are given in Table 4.7 for the ASRB station Locarno-Monti for 12 UTC observations from 1996–2002. Lower scores for maximum zero or one octa PCA difference are found for spring- and summertime, but scores remain stable for maximum two octas difference throughout the year.

**Table 4.6:** Diurnal cycle and daily averages of scores for maximum one octa difference between estimated and observed partial cloud amount.

LT	PAY	LOM	JFJ	DAV	WFJ	NYA	KWA <sup>a</sup>
01	86.6	...	...	...	...	...	83.3
04	86.7	...	...	...	...	...	...
07	87.0	88.1	84.2	92.0	87.2	83.2	76.2
10	88.0	87.6	84.7	...	...	...	...
13	86.9	85.5	82.2	87.6	89.4	82.0	77.7
16	88.0	85.7	82.9	...	...	...	...
19	84.3	87.3	80.6	84.9	83.8	83.0	69.6
22	87.3	...	...	...	...	...	...
Avg	86.9	86.8	82.9	88.2	86.8	82.7	76.7

<sup>a</sup>LT minus 1 hour

**Table 4.7:** Annual cycle of scores for maximum zero, one or two octas difference between estimated and observed partial cloud amount in Locarno-Monti for 12 UTC.

Season	Score			N
	±0 (%)	±1 (%)	±2 (%)	
Winter (Jan. –Mar.)	54.9	87.8	95.2	559
Spring (Apr. –Jun.)	38.9	83.4	95.8	499
Summer (Jul. –Sep.)	34.6	82.8	95.1	512
Autumn (Oct. –Dec.)	55.9	87.2	94.7	564



## 4.6 Discussion

### 4.6.1 Comparison of Observed and Estimated Partial Cloud Amount

Various points complicate the comparison of observed and estimated partial cloud amount (*PCA*):

1. The relation between sky cover and measured *LDR* is disturbed through the synoptic rule that even a small cloud in an almost cloud-free sky leads to one octa cloud amount, even if the cloud covered area is far less than one octa.
2. A major disadvantage of observations is the missing information about hemispherical distribution of cloud amount. Clouds near zenith have a larger influence on *LDR* than clouds near the horizon due to shorter distance and larger radiant intensity, which is proportional to the cosine of the zenith angle. Therefore, small amounts (up to two octas) of convective clouds bound to surrounding mountain chains have no detectable influence on *LDR* and are therefore missed by APCADA. For diurnal cycle, results in Fig. 4.4 indicate that mainly the score for maximum zero octa *PCA* difference is decreased in the early evening (18 UTC) due to the raising number of convective clouds near the horizon and the before mentioned rule for very small clouds. For annual cycle, results in Tab. 4.7 show that the dominance of convective clouds in Switzerland in spring and summer slightly reduces the scores for maximum zero and one octa *PCA* difference, but the score for maximum two octas remains stable for all seasons.
3. Time of observation and observed cloud amounts for the same sky cover slightly vary for each synoptic observer. Hence, observation and estimation of *PCA* can strongly disagree when observations are taken too early or too late.
4. Cirrostratus was observed for most of the outliers with four or more octas *PCA* difference in the upper right corner in Tab. 4.5, but the influence on *LDR* rather indicated a thin altostratus layer. The problem to distinguish between middle and high clouds even intensifies during nighttime, when light conditions are poor. The percentage of outliers with cirrus clouds observed increases during nighttime compared to daytime in Payerne (not shown).

Taking all points mentioned above into account, the overall agreement of estimated and observed *PCA* is astonishingly good for all seasons (Tab. 4.7) and daytimes (Fig. 4.4, Tab. 4.6). Therefore, the assumption of a periodic function for the lapse rate at the surface for the diurnal and annual cycle leads to good agreement between observed and estimated *PCA* at all tested radiation sites.

The availability of APCADA estimated *PCA* depends on the number of simultaneously available *LDR*, temperature and humidity measurements. For the investigated ASRB datasets (Tab. 4.1) APCADA estimated *PCA* were available for 98.9% in Payerne, and still for 95.4% of all possible 10 minutes values at Jungfrauoch, where measurements are taken under harsh alpine weather conditions. At the BSRN station NYA 99.0% of all possible *PCA* estimates were available, and 94.1% at KWA.

### 4.6.2 Comparison of Single Day in Payerne

APCADA was designed for real-time processing and monitoring *PCA*. Figure 4.5 shows the comparison of observed and APCADA estimated *PCA*, which agree with less than one octa difference in average. *PCA* is calculated from *CFI* and Stdev *LDR* according to the rules in Tab. 4.4. APCADA is suitable to detect short-time occurrences of clouds between synoptic observations, e.g. at 1530 UTC. Thus, the high temporal resolution of 10 minutes allows to compare APCADA estimates with cloud cover measurements from other high temporal cloud detection systems at the Earth's surface and from satellite based schemes.

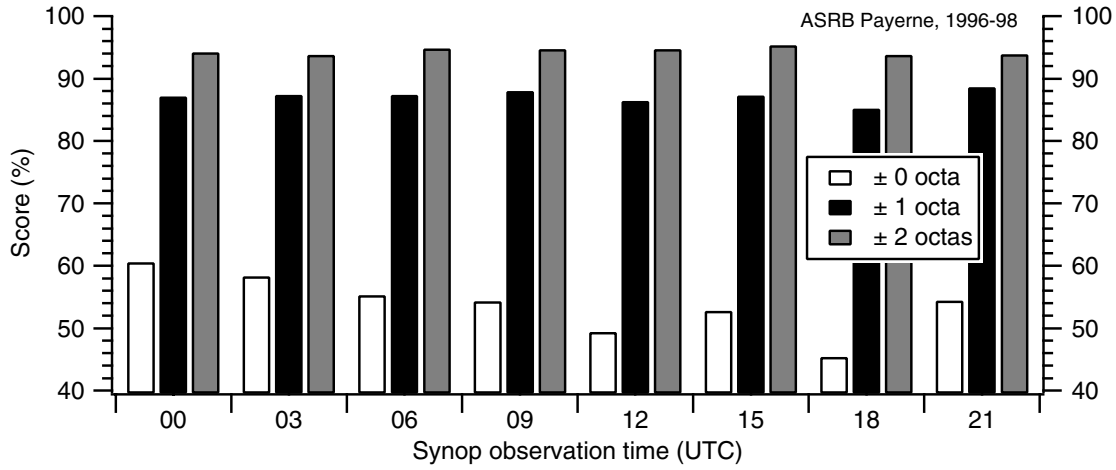


**Figure 4.4:** Diurnal cycle of score index for maximum zero, one or two octas difference between estimated and observed partial cloud amount in Payerne from 1996–98. The score for zero octa difference decreases from about 60 at midnight to 45 in the late afternoon. Score rates for maximum one or two octas difference remain stable all over the day.

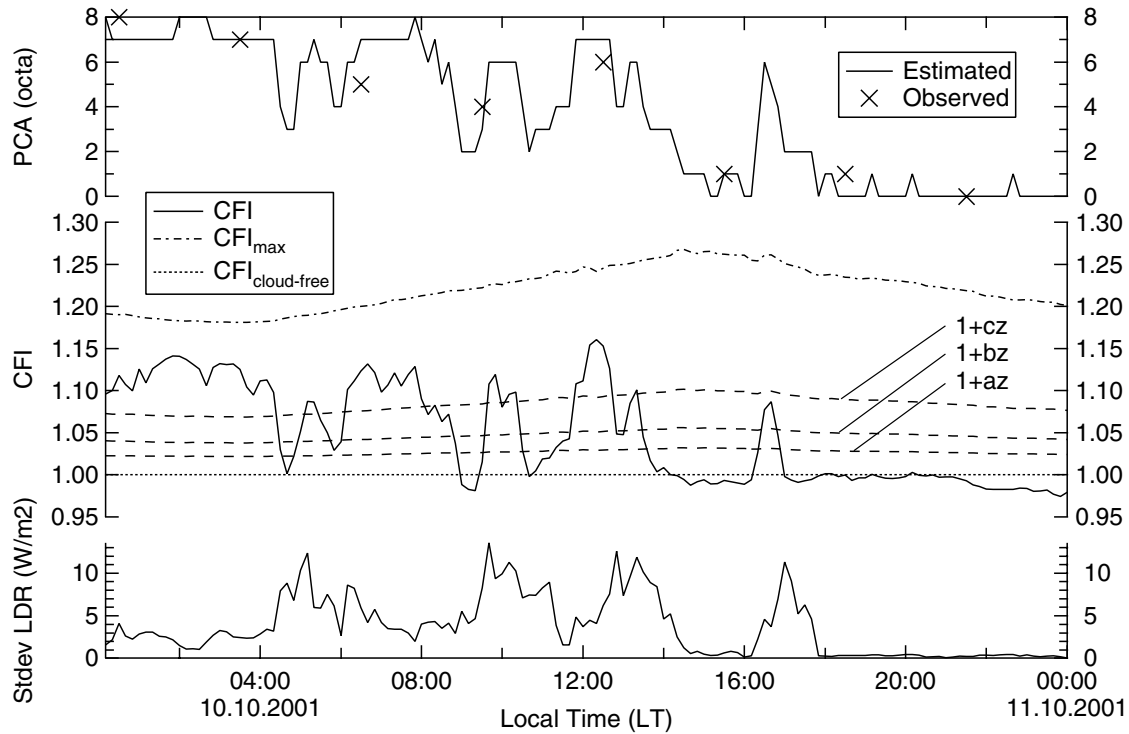


**Figure 4.5:** Comparison of observed and estimated partial cloud amount (PCA) for a single day in Payerne. Overcast (00 UTC – 04 UTC) and mostly cloud-free conditions (18 UTC – 24 UTC) are characterised by small LDR variability (Stdev LDR), but different CFI values. Broken cloud conditions (04 UTC – 18 UTC) show enhanced LDR variability and most of the PCA estimates vary between 2 and 6 octas.

### 4.6.3 Implementation of APCADA in Different Climate Regions

APCADA has been adapted to five radiation stations in the Swiss Alps, one site in the Arctic sea on Spitzbergen and one site in the tropical Pacific ocean. Locations of the different radiation sites in the Alps are distributed over a wide range of altitudes and therefore cover different climate zones with annual mean temperatures from 13° (LOM) to -7° Celsius (JFJ). Topography varies from site to site: LOM and DAV are situated in valleys, and WFJ and JFJ are crest stations with harsh weather conditions. PAY is located on a wide plateau, which is surrounded by the Alps in the south, and the Jura mountains in the north-west. Winter half year (Oct.–Mar.) in Switzerland is predominantly characterized by stratiform clouds, whereas summer half year (Apr.–Sep.) is dominated by convective clouds. Maritime influences dominate the climate at NYA and KWA. Results shown in Fig. 4.4 and Tab. 4.6 show that APCADA was successfully adapted to radiation sites in various climate zones from low to high latitudes. The lowest score rates are found for KWA (Tab. 4.6). Investigations showed that the percentage of broken *PCA* (2–6 octas) in KWA is over 60% compared to about 30% in PAY which decreases the precision of APCADA. The diurnal cycle of the amount of convective clouds in KWA is also reflected in the according score rates: minimum is reached in late afternoon (06 UTC), and maximum at midnight (12 UTC).

### 4.6.4 Cloud Amount Detection without High Clouds

APCADA is able to detect only clouds which have a measurable effect on *LDR*, i.e. increasing *LDR* variability and/or additional effect on *LDR* at the Earth' surface. Hence, the comparison of estimated and observed sky cloud cover had to be restricted to the total amount of clouds without high clouds. Concerning daily weather forecast, informations about cloud amount affecting sunshine duration, i.e. low and middle clouds, are of interest for a broad general public. However, further investigations are needed to combine APCADA with other cloud detection systems during day- and nighttime to include the occurrence of high clouds for climatological studies.

## 4.7 Conclusions

An improved version of the Clear-Sky Index (*CSI*), called Cloud-Free Index (*CFI*), was formulated to reduce the inadvertent diurnal and annual cycle of *CSI* for estimating cloud-free cases. *CFI* is calculated from measurements of longwave downward radiation (*LDR*), temperature and relative humidity at screen level height. A real-time processing system called APCADA (automatic partial cloud detection algorithm) has been developed to automatically estimate partial cloud amount (*PCA*) every 10 minutes during day- and nighttime based on *CFI* and the variability of *LDR*.

APCADA estimated *PCA* was compared with synoptic observations from five radiation sites at different altitudes in the Swiss Alps, from one site in a arctic climate, and from one location with tropical climate. In about 82%–87% of all cases the maximum cloud amount difference between estimate and observation was smaller or equal one octa both during day- and nighttime for high- and midlatitude sites. At the tropical site Kwajalein the according scores range from 70%–83% due to dominance of convective clouds with predominantly 2–6 octas sky cloud cover. Average site percentages for maximum  $\pm 2$  octa cloud amount difference range from 90% up to 95% for all investigated radiation stations.

The implementation of APCADA at a radiation site is independent from the knowledge of synoptic cloud cover observations. Thus, existing *LDR* series of measurements with accompanying temperature and humidity measurements are suitable to be postprocessed by APCADA to investigate the longterm behavior of cloud amount with high temporal resolution. APCADA estimates of *PCA* were available for 94% (KWA) up to 99% (PAY) of all possible 10 minutes data depending on the simultaneous availability of *LDR*, temperature and relative humidity measurements at screen level height.



## Chapter 5

# Homogenisation of Longterm LDR Series

### 5.1 Introduction

The longterm behaviour of measured longwave downward radiation (*LDR*) at the Earth's surface is the most promising key variable for the detection of the greenhouse signal, because it emerges earlier from the background noise than the surface temperature (*Wild and Ohmura, 2001*). Recently published results (*Philipona et al., 2004b*) prove the potential of longterm *LDR* measurements to correlate changes of *LDR* at the surface with changes of air temperature, humidity and shortwave and longwave cloud effect. However the mean expected *LDR* increase of about  $2 \text{ W m}^{-2}$  per decade projected by several coupled GCMs (*Wild et al., 1997*) is rather small, and inhomogeneities in *LDR* series caused by instrument change or failures in the data acquisition system can easily make a detection of the radiation change difficult.

A new method is presented here to test a set of cloud-free and overcast nighttime cases for *LDR* inhomogeneities and to correct erroneous *LDR* measurements with a simple linear function of the longwave net radiation.

### 5.2 Methods

Longterm changes of *LDR* at the surface can be attributed to changes of temperature, total greenhouse gas concentration and cloud cover (*Philipona et al., 2004b*). To distinct these variations from inhomogeneities caused by station relocation, instrument modification or electronic failures in the data acquisition system, a new parameter called *CFI*-saturation was defined, which is mostly invariant to changes of air temperature, humidity and cloud cover. It was assumed that air temperature and humidity measurements from THYGAN (see section 2.1) were reliable for the whole investigated period. Only nighttime cases were investigated to avoid the influence of solar radiation on *LDR* measurements (*Marty, 2000*).

#### 5.2.1 *CFI*-Saturation

The effect of clouds on *LDR* compared to cloud-free conditions can be expressed also in terms of the Cloud-Free Index (*CFI*), which is described in section 4.4.2. Cloud-free conditions are indicated by *CFI* values lower or equal than 1, and overcast situations show *CFI* values close to the maximum possible value  $CFI_{\max} = \frac{\epsilon_{\text{overcast}}}{\epsilon_{\text{AC}}}$  with  $\epsilon_{\text{overcast}} = 1$ . However  $CFI_{\max}$  is not constant and varies with different temperature and humidity at the surface. Hence *CFI* was transformed to the so-called *CFI*-saturation. Hereinafter *CFI*-saturation is referred to as  $CFI_{\text{sat}}$ .  $CFI_{\text{sat}}$  is mostly invariant to changes of air temperature and humidity at the surface both for cloud-free and overcast sky conditions.  $CFI_{\text{sat}}$  is

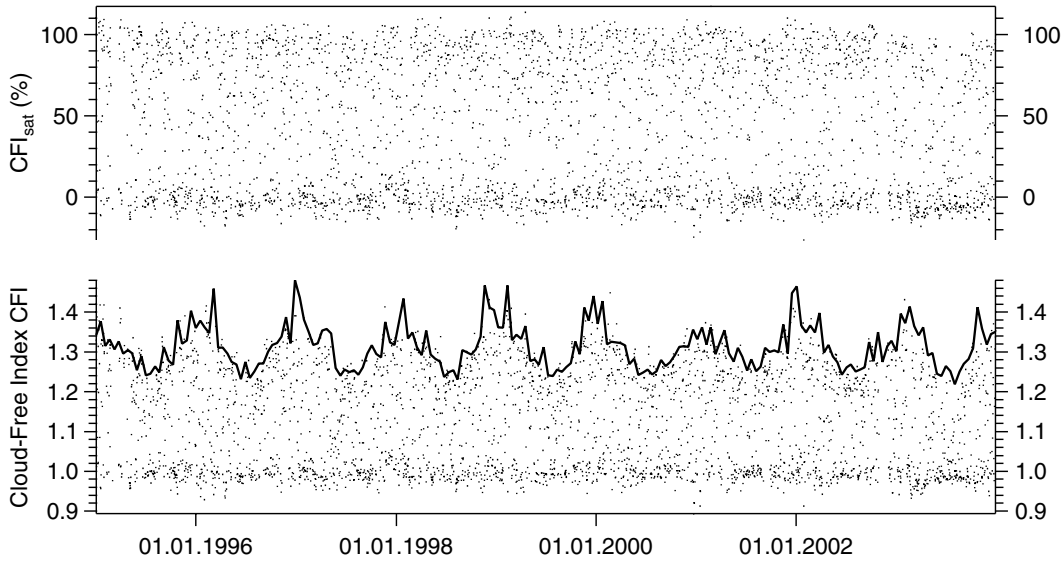


**Figure 5.1:** Mean  $CFI$  and  $CFI_{sat}$  for Davos during nighttime ( $03 \text{ UTC} \pm 1 \text{ hour}$ ). The solid line indicates  $CFI_{max}$ . The annual cycle of  $CFI_{sat}$  is clearly reduced compared to the annual cycle of  $CFI$ .

derived from  $CFI$  (Eq. 4.10) and variable  $z$  (Eq. 4.16):

$$CFI_{sat} = 100 \frac{CFI - 1}{z}, \quad (5.1)$$

with  $z = CFI_{max} - CFI_{cloud-free}$ ,  $CFI_{cloud-free} = \frac{\epsilon_{AC}}{\epsilon_{AC}} = 1$ .  $CFI_{sat}$  is given in percent, and has a value close to 100% for overcast situations, i.e. the longwave emission by clouds reaches saturation, and below 0% for cloud-free conditions. Thus different cloudy sky conditions are characterised by varying degrees of  $CFI$ -saturation.  $CFI_{sat}$  is preferred to  $CFI$  because  $CFI$  shows a strong annual cycle for the maximum  $CFI$  values during overcast situations. As an example,  $CFI$  and  $CFI_{sat}$  are shown in Figure 5.1 for Davos during nighttime ( $03 \text{ UTC} \pm 1 \text{ hour}$ ) from 1995 to 2003.

Temperature and humidity changes have per definition no effect on  $CFI$  (see section 4.4.2), but slightly affect  $CFI_{sat}$  through variable  $z$  in Eq. 5.1. However the variation of  $CFI_{sat}$  caused by temperature and humidity changes was found to be small enough to distinct between inhomogeneities and other variations.

### 5.2.2 $CFI$ -Saturation Inhomogeneities

Calm cloud-free nighttime cases with  $\text{Stdev } LDR_{2h} \leq 1 \text{ W m}^{-2}$  ( $03 \text{ UTC} \pm 1 \text{ hour}$ ) and  $CFI_{sat} < 20\%$  were selected from ASRB  $LDR$  measurements to detect possible  $LDR$  inhomogeneities (see also section 4.4.4). Analogously overcast cases were found with  $\text{Stdev } LDR_{2h} \leq 2 \text{ W m}^{-2}$  and  $CFI_{sat} > 50\%$ . Figure 5.2 shows an example for a homogeneous  $CFI_{sat}$  series measured at Weissfluhjoch, and analogously for Davos with obvious problems at the beginning of 1998, when a clear inhomogeneity occurred.

Inhomogeneities found in  $CFI_{sat}$  series have to be expressed again in terms of  $LDR$  to homogenise the time period of erroneous  $LDR$  measurements.  $LDR$  can be formulated as a function of  $CFI$  using Eqs. 4.10 and 4.2:

$$LDR = \epsilon_{AC} \sigma T^4 CFI. \quad (5.2)$$

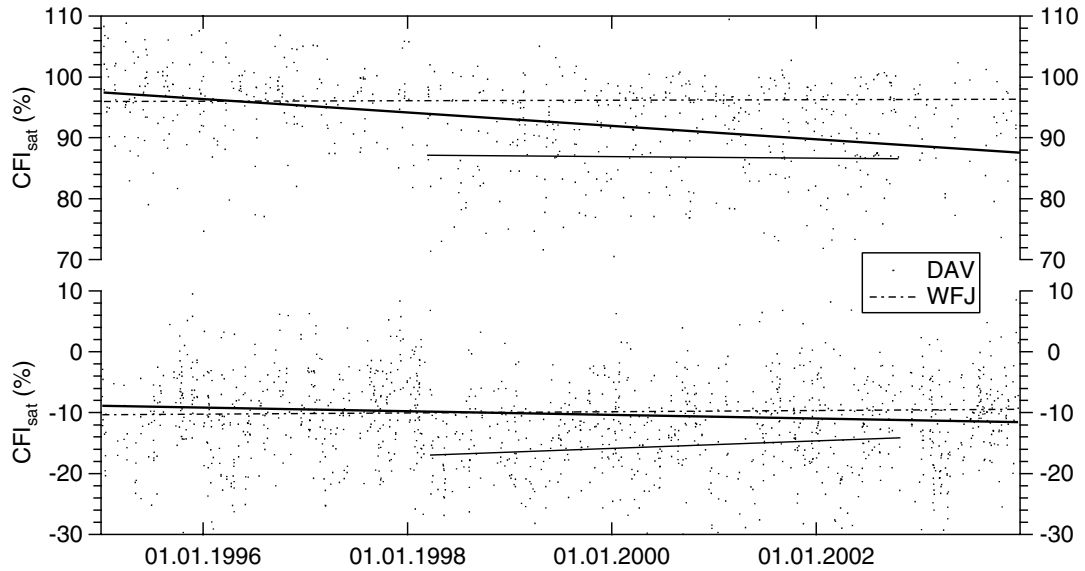


**Figure 5.2:** Average  $CFI_{sat}$  for calm overcast and cloud-free nighttime cases at ASRB Weissfluhjoch and ASRB Davos. Single points indicate nighttime means (03 UTC  $\pm$  1 hour) for Davos, and solid lines indicate trendlines for Davos over the whole period, and separately for the inhomogeneity between 1998 and 2002. The dotted-dashed trendlines for WFJ are also shown.

Then, if we solve for  $CFI$  in Eq. 5.1 and substitute  $CFI$  in Eq. 5.2, we obtain:

$$LDR = \sigma T^4 (1 - \epsilon_{AC}) \frac{CFI_{sat}}{100} + \epsilon_{AC} \sigma T^4. \quad (5.3)$$

From the first derivative of  $LDR$  with respect to  $CFI$ -saturation, we obtain the mean finite increment  $\Delta \overline{LDR}$ :

$$\Delta \overline{LDR} = \sigma \overline{T}^4 (1 - \overline{\epsilon}_{AC}) \frac{\Delta CFI_{sat}}{100}. \quad (5.4)$$

As mentioned in section 5.2.1, changes of temperature and humidity are already included in  $CFI_{sat}$ , and only the derivative with respect to  $CFI_{sat}$  is used to find the according change of  $LDR$  ( $\Delta \overline{LDR}$ ). Mean values of temperature  $T$  ( $\overline{T}$ ) and cloud-free sky emittance  $\epsilon_{AC}$  ( $\overline{\epsilon}_{AC}$ ) within the correction time period are used to calculate the mean  $LDR$  offset  $\Delta \overline{LDR}$ . The difference of the mean  $CFI_{sat}$  ( $\overline{CFI_{sat}}$ ) values between the reference time period and correction time period was used to calculate  $\Delta CFI_{sat}$ :  $\Delta CFI_{sat} = \underbrace{\overline{CFI_{sat}}}_{\text{Reference}} - \underbrace{\overline{CFI_{sat}}}_{\text{Correction}}$ .

For the calculation of  $\Delta LDR$  in overcast situations, it is recommended to have a second  $LDR$  series from a second backup pyrgeometer or a neighbouring site to avoid to wrongly correct an existing longterm  $LDR$  trend for overcast situations. Otherwise  $\Delta \overline{LDR}$  should be evaluated only when obvious breaks occur in the  $CFI_{sat}$  series.

### 5.2.3 Correction of Inhomogeneous $LDR$ Series

Cloud-free and overcast situations are well-defined sky conditions and can be used to determine  $CFI_{sat}$ , and hence  $LDR$ -inhomogeneities. Erroneous longwave downward radiation ( $LDR_{err}$ ) values are corrected with a linear function of the longwave net radiation ( $LNR$ ):  $LNR = LDR_{err} - LUR$ .  $LUR$  is approximated

with the help of the PIR body temperature  $T_{\text{PIR}}$  and Plank's law:  $LUR = \sigma T_{\text{PIR}}^4$ . The correction term  $\Delta LDR_{\text{corr}}$  is used to correct  $LDR_{\text{err}}$  as follows:

$$LDR = LDR_{\text{err}} + \Delta LDR_{\text{corr}} \quad (5.5)$$

$$\Delta LDR_{\text{corr}} = c_1 + c_2 \frac{LNR - \overline{LNR}_{\text{ovc}}}{(-\overline{LNR}_{\text{cfr}})}, \quad (5.6)$$

with  $\overline{LNR}_{\text{ovc}}$  the mean longwave net radiation for all calm overcast situations, and analogously  $\overline{LNR}_{\text{cfr}}$  the mean longwave net radiation for all calm cloud-free situations within the correction time period.  $c_1$  and  $c_2$  are defined as  $c_1 = \Delta \overline{LDR}_{\text{ovc}}$  and  $c_2 = \Delta \overline{LDR}_{\text{ovc}} - \Delta \overline{LDR}_{\text{cfr}}$ , where  $\Delta \overline{LDR}$  is calculated using Eq. 5.4.  $\Delta LDR_{\text{corr}}$  has to be added to all  $LDR$  measurements within the correction time period to accomplish the  $LDR$  correction. Arguments for defining  $\Delta LDR_{\text{corr}}$  as a function of  $LNR$  are discussed later in section 5.4. Table 5.1 lists the parameters used to calculate  $\Delta \overline{LDR}$  in Eq. 5.4 for cloud-free and overcast situations at ASRB Davos and Jungfraujoch. Table 5.2 summarises the parameters used for the calculation of  $\Delta LDR_{\text{corr}}$  (Eq. 5.6) for the same stations.

**Table 5.1:** Parameters for calculation of  $LDR$  correction  $\Delta \overline{LDR}$  at ASRB stations Davos and Jungfraujoch for cloud-free and overcast nighttime situations.

Sta	Correction time period	$\Delta \overline{LDR}_{\text{cfr}}$			$\Delta \overline{LDR}_{\text{ovc}}$		
		$\sigma \overline{T}^4$ W m <sup>-2</sup>	$\overline{\epsilon}_{\text{AC}}$ 1	$\Delta \overline{CFI}_{\text{sat}}$ %	$\sigma \overline{T}^4$ W m <sup>-2</sup>	$\overline{\epsilon}_{\text{AC}}$ 1	$\Delta \overline{CFI}_{\text{sat}}$ %
DAV	01.09.94–04.03.98	310.9	0.753	-2.8	320.7	0.775	6.6
DAV	05.03.98–17.08.98	337.0	0.780	6.4	327.1	0.781	-2.0
DAV	18.08.98–01.11.02	316.2	0.757	3.6	324.8	0.779	-2.2
JFJ	01.10.95–27.11.97	287.0	0.637	-2.6	279.9	0.684	-2.4

**Table 5.2:** Correction time period and parameters for  $LDR$  correction term  $\Delta LDR_{\text{corr}}$  (Eq. 5.6) as a function of longwave net radiation ( $LNR$ ). Units are given in W m<sup>-2</sup>.

Sta	Correction time period	$\Delta LDR_{\text{corr}}$		$\overline{LNR}_{\text{cfr}}$	$\overline{LNR}_{\text{ovc}}$
		$c_1$	$c_2$		
DAV	01.09.94–04.03.98	-4.8	-2.6	-81	-3
DAV	05.03.98–17.08.98	1.4	-3.3	-85	-9
DAV	18.08.98–01.11.02	1.6	-1.2	-86	-9
JFJ	01.10.95–27.11.97	-2.1	0.6	-112	1

### 5.3 Comparison of uncorrected and corrected $LDR$ series

#### 5.3.1 ASRB Station Davos

The upper part of Figure 5.3 shows the uncorrected  $CFI_{\text{sat}}$  values for calm overcast and cloud-free nights in Davos. Only linear regressions of  $CFI_{\text{sat}}$  are plotted for VSF and WFJ. The solid lines indicate the mean  $CFI_{\text{sat}}$  level of the reference time period (2003), and the mean level of the two periods with erroneous  $LDR$  measurements from 1995 to 1998, and 1998 to 2002.

The lower part of Figure 5.3 shows the  $LDR$  series for Davos corrected with the help of Eq. 5.6 and parameters given for the different correction time periods given in Tab. 5.2. The linear regression



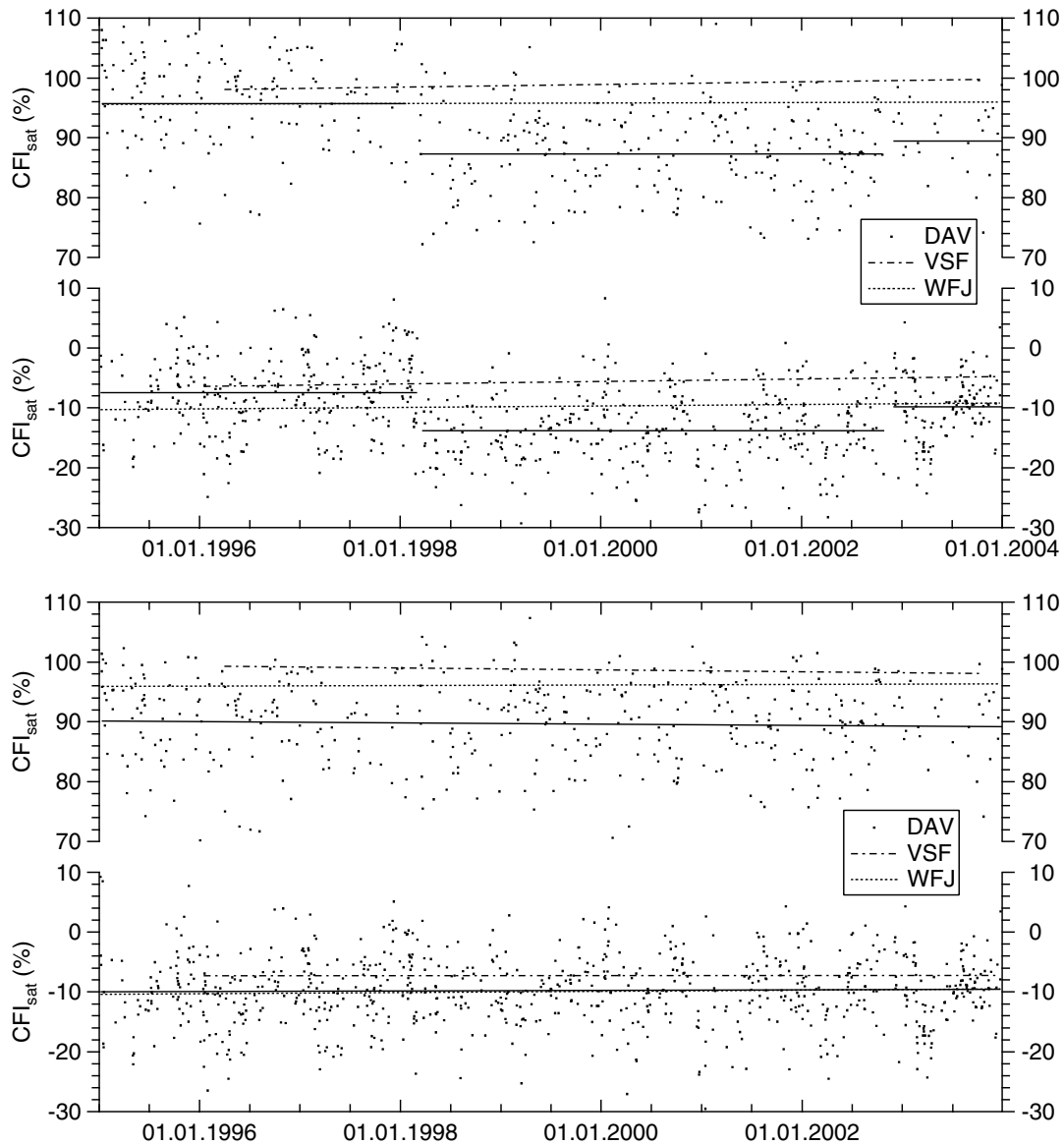


**Figure 5.3:** *Uncorrected (upper figure) and corrected (lower figure) CFI-saturation ( $CFI_{\text{sat}}$ ) in Davos for cloud-free ( $CFI_{\text{sat}} \approx -10\%$ ) and overcast ( $CFI_{\text{sat}} \approx 90\%$ ) nighttime (02–04 UTC) conditions. Single dots indicate nighttime (03 UTC  $\pm$  1 hour) means of  $CFI_{\text{sat}}$ . The solid lines for Davos in the upper figure give the mean  $CFI_{\text{sat}}$ -values for the reference period 2003, and the two correction periods from 1995 to 1998, and from 1998 to 2002. The solid lines in the lower figure indicate the trendlines for  $CFI_{\text{sat}}$  in Davos after correction. Different dashed or dotted trendlines for Weissfluhjoch (WFJ) and SLF-Versuchsfeld (VSF) are shown for comparison.*

for cloud-free DAV cases agrees well with WFJ and also with VSF, whereas the linear regression for overcast situations in Davos is clearly lower than for WFJ and VSF. WFJ and VSF are peak locations, which are often surrounded by clouds during overcast conditions. Therefore values of  $CFI$ -saturation are close to 100 % for WFJ and VSF. Davos, however, is located in a valley, and cloud base is normally above the station which is indicated by lower  $CFI$ -saturation values during overcast conditions.

### 5.3.2 ASRB Station Jungfraujoch

A positive  $CFI_{\text{sat}}$  offset in the order of 4% is shown in the upper part of Figure 5.4 from the beginning of measurements in 1995 until November 1997, when the ASRB site was relocated. The mean  $CFI_{\text{sat}}$  level for the time period with erroneous  $LDR$  measurements and for the reference period are shown. The linear trend after  $LDR$  correction for cloud-free conditions is very similar to the trend of EGH, which is a neighbouring ASRB site with comparable altitude.

## 5.4 Discussion

### 5.4.1 Reasons for $LDR$ Inhomogeneities

Different inhomogeneities have different effects on cloud-free or overcast situations. As an example, the Sphinx dome at Jungfraujoch covered a large portion of the ASRB instruments field of view before the ASRB instruments were relocated by about 20 meters in the end of November 1997. In cloud-free situations with a large net loss of longwave radiation, the surface temperature of the Sphinx dome is clearly higher than the apparent temperature of the sky. Hence the ASRB pyrgeometer overestimated  $LDR$  under cloud-free conditions before the end of 1997. However the Sphinx dome's temperature is roughly the same than the apparent sky temperature for totally overcast situations, and hence the influence of the obstacle to  $LDR$  is smaller.

An example for a radiation site with several periods of erroneous  $LDR$  measurements was shown for the  $CFI$ -saturation series in Davos (Fig. 5.3, upper part). Davos was maintained differently from the other ASRB sites: the ASRB logger was part of a data acquisition system using a modem with a coax ring, where several data loggers from other radiation instruments could be reached with the same phone number, but a different address. The ASRB data acquisition system had to be changed two times, because quality control of various radiation fluxes revealed problems. The first change was done on the 4th of March 1998, where a resistance was removed from the multiplexer. This change is visible as a first strong inhomogeneity in the  $CFI_{\text{sat}}$  series in the beginning of 1998. A few months later, on the 17th of August, the old CR10 data logger was exchanged for a new CR10X data logger. This caused another inhomogeneity, which is clearly visible in the daytime (14–16 UTC)  $CFI_{\text{sat}}$  series (not shown). The last important change was performed end of October 2002, where the ASRB instruments were moved to a small hill 100 m away from PMOD/WRC, and with approximately the same height a.s.l. as before. The ASRB pyrgeometer was calibrated in situ several times from 2000 to 2004 with the reference Eppley pyrgeometer (serial 31463F3), and it was additionally calibrated once in November 2003 with the CG4-pyrgeometer (serial FT005) from the new travelling standard. These calibrations showed that the ASRB pyrgeometer measured correctly since November 2002 at the new position, but measured too high in the beginning until March 1998, and too low between March 1998 and October 2002. All mentioned inhomogeneities were caused by electronic failures in the data acquisition system, and affirm the need of a possibly single-used and well grounded data logger setup for  $LDR$  instruments.

We found different reasons for  $LDR$  inhomogeneities at the investigated ASRB sites: relocation with changed field of view at Jungfraujoch and electronic failures in the data acquisition system in Davos. All found  $LDR$  inhomogeneities are influencing cloud-free and overcast conditions differently. Cloud-free

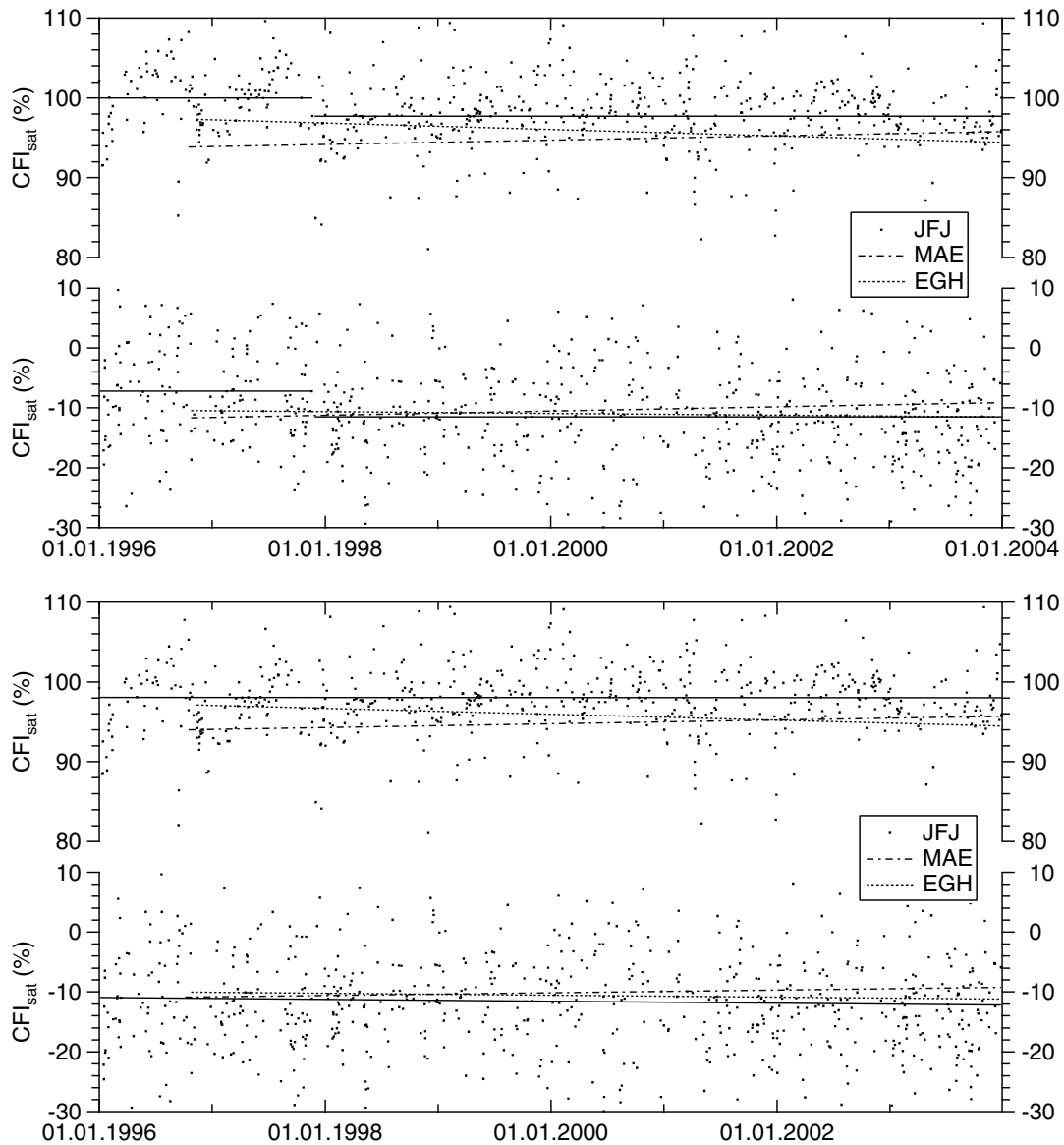


**Figure 5.4:** *Uncorrected (upper figure) and corrected (lower figure) CFI-saturation ( $CFI_{\text{sat}}$ ) at Jungfraujoch for cloud-free ( $CFI_{\text{sat}} \approx -10\%$ ) and overcast ( $CFI_{\text{sat}} \approx 90\%$ ) nighttime (02–04 UTC) conditions. Single dots indicate nighttime (03 UTC  $\pm$  1 hour) means of  $CFI_{\text{sat}}$ . The solid lines for Jungfraujoch in the upper figure give the mean  $CFI_{\text{sat}}$ -values for the reference period 1998 to 2003, and the correction period from 1995 to 1997. The solid lines in the lower figure indicate the trendlines for  $CFI_{\text{sat}}$  at Jungfraujoch after correction. Different dashed or dotted trendlines for Männlichen (MAE) and Eggishorn (EGH) are shown for comparison.*

and overcast skies are mainly characterised by strongly differing *LNR* values. Therefore the equation for *LDR* correction (see Eq. 5.6) was formulated as a function of *LNR* to correct cloud-free and overcast situations separately.

### 5.4.2 Limitations of Longterm *LDR* Series Correction

The following requirements have to be met for the application of the *LDR* correction method described in the preceding sections:

- Adaptability of *CFI*-method (see section 4.4.2) to a *LDR* site, i.e. station with regular diurnal and annual temperature gradient conditions at the surface, or stations where the factors  $k$  and  $\Delta k$  could be determined directly from temperature gradient measurements with high temporal resolution
- Sufficient number ( $> 20$ ) of calm cloud-free and overcast nighttime cases inside and outside the time period with erroneous *LDR* measurements
- Neighbouring  $CFI_{\text{sat}}$  series for comparison of overcast *CFI*-saturation trends

## 5.5 Conclusions

A simple method was presented to homogenise longterm *LDR* series based on a newly introduced parameter called *CFI*-saturation, which is mostly invariant to changes of air temperature and humidity both for cloud-free and overcast situations, but sensitive to *LDR* inhomogeneities. Examples for *LDR* inhomogeneities caused by instrument relocation with different field of view of the radiation instruments before and after relocation and *LDR* offsets induced by electronic failures in the data acquisition system were shown. The *LDR* correction equation was formulated as a function of the longwave net radiation, because most of the *LDR* inhomogeneities are assumed to affect *LDR* measurements differently during cloud-free or overcast sky conditions.

## Chapter 6

# Comparison of Observed and Modeled Longwave Downward Radiation

### 6.1 Introduction

Radiative transfer models (RTMs) play an important role on the energy balance in general circulation models (GCMs) and numerical weather prediction models (NWP). Both applications demand large computational resources and simplified radiation schemes are used. An investigation of radiation transfer schemes in different GCMs shows large differences in globally averaged longwave downward radiation (*LDR*) (Wild *et al.*, 2001) compared to *LDR* measurements of the Baseline Surface Radiation Network (BSRN) (Ohmura *et al.*, 1998). For cloud-free and cold atmospheric conditions GCMs most underestimate *LDR*, whereas at higher ambient temperature, e.g. in the tropics, some GCMs tend to overestimate the *LDR*. A similar comparison of *LDR* forecasts by the ECMWF model and surface observations (Chevallier and Morcrette, 2000) shows a cloud-free *LDR* underestimation with a strong diurnal cycle for mid-latitude sites.

The progress of computing power over the last years improves the chance to replace simplified radiative transfer schemes with more accurate radiation models. However Dutton (1993) revealed that the application of the more complex RTM LOWTRAN at four different radiation sites from the pole to the tropics still shows deficiencies of modelled *LDR* especially for cold and dry cloud-free conditions.

In the following sections the comparison of modelled and observed cloud-free *LDR* is described. *LDR* observations are obtained from the Alpine Surface Radiation Budget (ASRB) network in the Alps (Marty *et al.*, 2002). Modelled *LDR* is provided by the complex radiative transfer model MODTRAN v4.0 (Berk *et al.*, 2000) and by the non-hydrostatic NWP model named Lokal Modell “LM” (Doms and Schättler, 2004). LM is used in its operational configuration called alpine model “aLMo” at the Federal Office of Meteorology and Climatology (MeteoSwiss) in Zurich. aLMo uses a simplified RTM due to computation time reasons. The performance of both RTMs is shown, and the sources of *LDR* error and *LDR* sensitivities for various model input parameters are discussed.

### 6.2 Observational Data

#### 6.2.1 ASRB Data

Ten minutes averages of irradiance measurements from the ASRB network (see section 2.1) and BSRN station Payerne (see section 2.2) were used for *LDR* comparison. Besides Payerne six further ASRB stations were investigated. Table 6.1 gives an overview of ASRB sites used for *LDR* comparison.

**Table 6.1:** ASRB stations, abbreviation, altitude, aLMO gridpoint altitude and coordinates.

Station	Abr	Altitude	Gridpoint	Coordinates
Payerne	PAY	490 m	531 m	46°49'N, 6°57'E
Davos	DAV	1610 m	1785 m	46°49'N, 9°51'E
Cimetta	CIM	1670 m	1282 m	46°12'N, 8°48'E
Männlichen	MAE	2230 m	2416 m	46°37'N, 7°57'E
Versuchsfeld	VSF	2540 m	2051 m	46°50'N, 9°49'E
Gornergrat	GOR	3110 m	3077 m	45°59'N, 7°47'E
Jungfrauoch	JFJ	3580 m	3086 m	46°33'N, 7°59'E

## 6.2.2 Cloud-Free Situations

For the comparison of measured and computed *LDR* a set of cloud-free nighttime (23 UTC) and daytime (11 UTC) cases from 1996–2001 was identified with an improved version (see section 4) of the Clear-Sky Index method presented by *Marty and Philipona* (2000). Situations with estimated cloud amount not exceeding one octa for the investigated time  $\pm 2$  hours were used in nighttime, and additionally, low variability of measured global shortwave downward radiation (*SDR*) was required in daytime. Thus, clouds with a measurable effect on *LDR* (or *SDR*) were excluded. 30 min averages of *LDR*, temperature and relative humidity from 2250 to 2320 UTC, respectively from 1050 to 1120 UTC were used. These periods were chosen to coincide modelled *LDR* based on radiosonde launches at 2300 UTC, respectively 1100 UTC. We also applied naked-eye observations of horizontal visibility ( $V_{\text{obs}}$ ) obtained between 2320 and 2330 UTC and 1120 and 1130 UTC.

## 6.3 Models and Experiments

### 6.3.1 MODTRAN and Input Data

MODTRAN v4.0 (*Berk et al.*, 2000) is a widely used radiative transfer model for various radiance computations. The performance of MODTRAN *LDR* computations has been investigated at two different pyrogeometer intercomparisons (*Philipona et al.*, 2001, *Marty et al.*, 2003).

In our application of MODTRAN *LDR* was calculated with the help of the Gaussian quadrature using computed radiances at 3 different zenith angles. Wavelength range spanned from 2  $\mu\text{m}$  to 300  $\mu\text{m}$ , with 2  $\text{cm}^{-1}$  resolution from 2  $\mu\text{m}$  to 6  $\mu\text{m}$  (5000  $\text{cm}^{-1}$  to 1666  $\text{cm}^{-1}$ ), and from 6  $\mu\text{m}$  to 300  $\mu\text{m}$  (1666  $\text{cm}^{-1}$  to 33  $\text{cm}^{-1}$ ) with 1  $\text{cm}^{-1}$  resolution.

Vertical radiosonde profiles measured by SRS 400 radiosondes (*Richner*, 1999) in Payerne were assimilated in MODTRAN to compute *LDR*. SRS 400 radiosonde profiles are obtained every 12 hours since April 1990. The relative humidity profile up to 10 km a.s.l. was read into the model. Temperature and pressure up to the end of the radiosonde profile at about 35 km height were applied. Average seasonal profiles of temperature, relative humidity and pressure for winter, summer and autumn in Payerne combined with standard seasonal MODTRAN atmospheres were added up to 100 km a.s.l. for all missing altitudes. The values for the concentrations of greenhouse gases were supplied as far as possible from the observations. At Payerne ozone-sondes are launched three times a week. The observed total ozone was linearly interpolated for days without ozone-sondes. A simplified yearly cycle of  $\text{CO}_2$  in Switzerland with an amplitude of 10 ppm and a minimum in middle of August was superposed by a linear increase of 2  $\text{ppm}(\text{yr})^{-1}$  starting with 364 ppm in the beginning of 1996.  $\text{CO}_2$  values were taken from the Climate Monitoring & Diagnostics Laboratory (CMDL) station Schauinsland (48°0'N, 8°0'E, 1205 m a.s.l.) in southern Germany (*GLOBALVIEW-CO<sub>2</sub>*, 2002). For other trace gases like methane

MODTRAN mid-latitude summer (May–October) or winter (November–April) profiles were applied. To account for aerosol effects on *LDR* the MODTRAN rural aerosol model was used in Payerne and Locarno-Monti, and the tropospheric aerosol model was applied at all other ASRB-sites. The standard MODTRAN aerosol models can be modified by the surface meteorological range  $V$ , which is used instead of the horizontal visibility  $V_{\text{obs}}$  in MODTRAN.  $V$  is defined by the Koschmieder formula (*Kneizys et al.*, 1996)  $V = \frac{1}{\beta} \ln \frac{1}{\epsilon}$ , where  $\beta$  is the extinction coefficient evaluated at  $0.55 \mu\text{m}$ , and  $\epsilon$  is the threshold contrast, set equal to 0.02.  $V$  and horizontal visibility  $V_{\text{obs}}$  are related by the empirical relation  $V = (1.3 \pm 0.3) V_{\text{obs}}$ . In Payerne and Locarno-Monti the default mean value of  $V = 23 \text{ km}$  in MODTRAN was replaced by the mean observed horizontal visibility during day- and nighttime. At all other ASRB sites the standard model value for  $V$  was replaced by estimates for the mean  $V$  varying from 50 km (Cimetta) to 120 km (Jungfrauoch). Multiple scattering effects in MODTRAN were considered with the activation of Isaacs two-stream algorithm (*Isaacs et al.*, 1987). Investigations showed that the usage of the more complex DISORT model was not mandatory because only slightly different results were found compared to the Isaacs algorithm.

### 6.3.2 aLMo

The "alpine model" (aLMo) is a non-hydrostatic weather prediction model operational at MeteoSwiss since April 2001 (*Doms and Schättler*, 2004). It was possible however to re-run the model for cloud-free cases back to 1999. aLMo is based on the Local Model (LM) developed in the frame of COSMO (COnsortium for Small scale MOdelling of the five national weather services of Germany, Switzerland, Italy, Greece and Poland). For this study aLMo based on LM version 2.18 was applied. aLMo runs in a configuration of 385x325 grid points with a horizontal grid mesh of 7 km on a NEC SX-5 at the ETH High Performance Computing Centre CSCS (Swiss Centre for Scientific Computing at Lugano/Manno). It has 45 levels up to 23 km a.s.l., whereof 19 layers lie within the first 2 km. aLMo incorporates the radiative transfer scheme formulated by Ritter and Geleyn (*Ritter and Geleyn*, 1992). The scheme is based on the solution of the  $\delta$ -two-stream version (*Zdunkowski et al.*, 1980) of the radiative transfer equations incorporating the effects of scattering, absorption and emission by cloud droplets, aerosols, and gases in each part of the spectrum. The thermal spectrum from 4.64 to  $104.5 \mu\text{m}$  is divided into five spectral intervals. The absorption properties of  $\text{H}_2\text{O}$ ,  $\text{CO}_2$ ,  $\text{O}_3$  and  $\text{N}_2\text{O}$  are described with the  $k$ -distribution method (*Stephens*, 1984). The aLMo forecast provides the longwave net radiation  $LNR = LDR - LUR$  and ground temperature  $T_g$  at the lower boundary of the model atmosphere. *LDR* at the surface can now be found with the help of the lower boundary condition of the radiative transfer scheme (*Ritter and Geleyn*, 1992):

$$LDR = \frac{LNR + \sigma T_g^4}{\epsilon_g}, \quad (6.1)$$

where  $\epsilon_g = 0.996$  is the model ground emissivity. It is important to note that aLMo version 2.18 does only provide a ground temperature, but not a skin temperature, which could be compared directly to the emission temperature of the surface obtained from ASRB longwave upward radiation (*LUR*) measurements.

aLMo forecasts of atmospheric profiles, ground temperature and *LDR* operationally span over 48 hours with outputs for each forecast hour. In most cases aLMo vertical profiles 11 hours (+11h) after initiation of the aLMo forecast run were used. Only +11h-forecasts with zero cloud cover for low and middle clouds, but any high clouds were used for *LDR* night- and daytime comparisons. About 15% of all used aLMo cases contained high clouds, and about 7% showed more than 50% high cloud coverage.

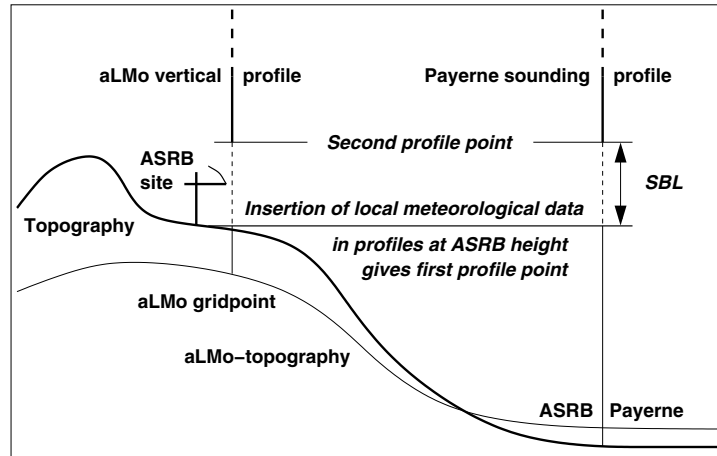


**Figure 6.1:** Scheme for insertion of measured meteorological data into aLMo vertical- or Payerne sounding profile at ASRB-station height. The original profile below ASRB height is skipped and measured surface parameters are inserted as the first profile point. MODTRAN interpolates temperature, humidity and pressure in the Surface Boundary Layer (SBL) up to the second profile point, where the vertical profiles are assumed to start from. The SBL thickness varies from 100 to 400 m.

### 6.3.3 Assimilation of Atmospheric Profiles in MODTRAN

#### Sounding Profile

Generally, 56 layers in the vertical from the surface to 100 km a.s.l. were used for MODTRAN LDR calculation. To insert radiosonde profiles the measured profile was reduced to about 36 layers between surface and 6 km a.s.l. by optimizing the absolute humidity profile. Between 6 km and up to 35 km a.s.l. radiosonde values were used at fixed altitude levels when available.

For Payerne the original sounding profile could be applied without modifications of the lowest layers. At all other seven ASRB stations Payerne radiosonde profiles were assumed to represent the atmosphere above the Surface Boundary Layer (SBL) for cloud-free situations all over Switzerland. For peak locations like Jungfrauoch, the SBL depth was set to about 100 m, and to about 400 m for valley locations like Davos. To account for the local SBL, measured temperature, absolute humidity and pressure were inserted at ASRB height to replace the free atmosphere values. Our application of MODTRAN incorporates also the skin temperature of the surface 2 m below the level of surface measurements. The skin temperature is obtained from LUR measurements in Payerne, Davos and SLF-Versuchsfeld. The temperature is calculated by Stefan-Boltzmann law with emissivity equal to one. At the other sites the skin temperature is set equal to the measured 2 m temperature. The insertion of measured meteorological data is schematically shown in Fig. 6.1. The unknown temperature and absolute humidity profiles in the SBL above the ASRB-station are interpolated linearly, respectively exponentially by MODTRAN.

#### aLMo Vertical Profile

The complex terrain over the Alps is still poorly resolved due to the aLMo horizontal grid mesh of seven km. Thus altitude differences between the nearest aLMo gridpoint and ASRB station can reach 500 m (see Tab. 6.1). Two different strategies were used to apply aLMo vertical profiles in alpine terrain: (i) Insertion of measured surface data in aLMo profile as indicated in Fig. 6.1. The lowest part of the aLMo profile is skipped up to the second profile point, if the height of the aLMo gridpoint is below ASRB-station height. If the height of the aLMo gridpoint is above ASRB-station height, then the two



bottommost profile levels are also skipped to remove the model SBL. The measured surface temperature, absolute humidity and pressure are inserted at ASRB-station height, and interpolated by MODTRAN to the second profile point for the radiation computation. (ii) Assimilation of original aLMo vertical profile in MODTRAN, but height correction of computed *LDR* with a seasonally different *LDR* height gradient. The height correction is explained in the following section.

### 6.3.4 Height Correction of Computed *LDR*

*LDR* computed by MODTRAN/aLMo and aLMo *LDR* forecasts were corrected with an average summer and winter cloud-free *LDR* gradient due to the height difference between the aLMo gridpoint and the ASRB station. Measured cloud-free gradients out of a 4-years ASRB dataset showed an average cloud-free gradient of  $-3.9 \text{ W m}^{-2}(100 \text{ m})^{-1}$  for summer and  $-2.7 \text{ W m}^{-2}(100 \text{ m})^{-1}$  for winter (Marty, 2000). This fits well to the average value of  $-2.8 \text{ W m}^{-2}(100 \text{ m})^{-1}$  found by Wild *et al.* (1995) using GCM calculations. To compare with measured surface temperature, aLMo 2 m temperature forecasts were height corrected with a mean lapse rate of  $0.65^\circ(100 \text{ m})^{-1}$ , but relative humidity was not changed.

### 6.3.5 Description of *LDR* Model Experiments

Radiative transfer model runs using different input data were accomplished for Payerne during night- and daytime, and for all other ASRB-sites during nighttime only. Table 6.2 gives an overview of nine different *LDR* computation runs. Model runs 3. and 8. (aLMo *LDR* forecasts) were provided by MeteoSwiss. The other model runs were accomplished at PMOD/WRC.

**Table 6.2:** Overview of different longwave downward radiation (*LDR*) computation model runs in Payerne and at six ASRB stations.

Model Runs	Model run name	Model		Vertical profile				Comparison at	
		MODTRAN	aLMo	Sounding org <sup>a</sup>	ins <sup>b</sup>	aLMo org	ins	Payerne	ASRB
1.	MODTRAN/Sond	x		x				x	
2.	MODTRAN/aLMo	x				x		x	
3.	aLMo forecast		x			x		x	
4.	MODTRAN/aLMo_ins	x					x	x	
5.	MODTRAN/Sond	x		x					x
6.	MODTRAN/Sond_ins	x			x				x
7.	MODTRAN/aLMo	x				x			x
8.	aLMo forecast		x			x			x
9.	MODTRAN/aLMo_ins	x					x		x

<sup>a</sup>Original profile

<sup>b</sup>Modified profile with surface data inserted

The model runs in Tab. 6.2 are grouped into 4 different *LDR* experiments:

1. Model run 1. is used to compare MODTRAN *LDR* computations based on sounding profiles with ASRB *LDR* measurements in Payerne
2. Model runs 2./3. and 7./8. are investigated to compare aLMo *LDR* forecasts with MODTRAN computations using the same aLMo vertical profile forecasts as input data

3. Model runs 1. and 2. allow to investigate the performance of measured and forecasted vertical profiles used for MODTRAN *LDR* computations
4. Model runs 5./6., 2./4. and 7./9. allow to investigate the benefit of surface data insertion into measured and forecasted vertical profiles

## 6.4 LDR Computation Experiments

Results for *LDR* model runs 1. to 4. in Payerne are shown in Table 6.3. Table 6.4 gives results for *LDR* model runs 5. to 9. at six ASRB stations (CIM, DAV, GOR, JFJ, MAE and VSF). Cloud-free cases with aLMo forecasts available were applied only. The different *LDR* model runs are further discussed in the

**Table 6.3:** Mean *LDR* difference (computed minus observed) and mean standard deviation for 54 nighttime- and 31 daytime cases in Payerne from 2000–01. Values are given in  $W m^{-2}$ .

Run name (No.)	Nighttime		Daytime	
	Diff	Stdev	Diff	Stdev
MODTRAN/sond (1.)	3.6	4.4	-3.1	5.3
MODTRAN/aLMo (2.)	-2.6	7.2	-2.8	7.5
aLMo forecast (3.)	-20.0	7.6	-3.6	11.9
MODTRAN/aLMo_ins (4.)	-2.3	4.4	1.2	5.2
MODTRAN/sond <sup>a</sup>	1.5	3.5	-3.2	3.6

<sup>a</sup>274 night- and 94 daytime cases from 1996 to 2001

**Table 6.4:** Mean *LDR* difference (computed minus observed) and mean standard deviation for about 17 nighttime cases at six ASRB stations from 2000–01. Values are given in  $W m^{-2}$ .

Run name (No.)	Diff	Stdev
MODTRAN/sond (5.)	1.8	7.9
MODTRAN/sond_ins (6.)	-1.7	6.1
MODTRAN/aLMo (7.)	-3.8	5.7
aLMo forecast (8.)	-25.8	7.2
MODTRAN/aLMo_ins (9.)	-2.8	4.4

following sections.

### 6.4.1 Experiment 1.: Performance of MODTRAN

Results from *LDR* model run 1. from 1996 to 2001 are shown in Fig. 6.2. ASRB *LDR* observations and MODTRAN computations using Payerne soundings agree very well with small scattering for nighttime (Fig. 6.2a). However, the gradient of the linear regression for nighttime indicates that MODTRAN tends to overestimate *LDR* at high *LDR* values, i.e. at high ambient temperatures. A slightly negative bias is indicated for *LDR* computed for daytime (Fig. 6.2b), but with a gradient close to one.

For each cloud-free night- or daytime case the *LDR* difference between model and observation was calculated, and the statistics are given in Tab. 6.3.

The number of cloud-free nighttime cases is about three times larger than for daytime. This discrepancy is mainly caused by the additional removal of cases with cirrus clouds using *SDR* measurements

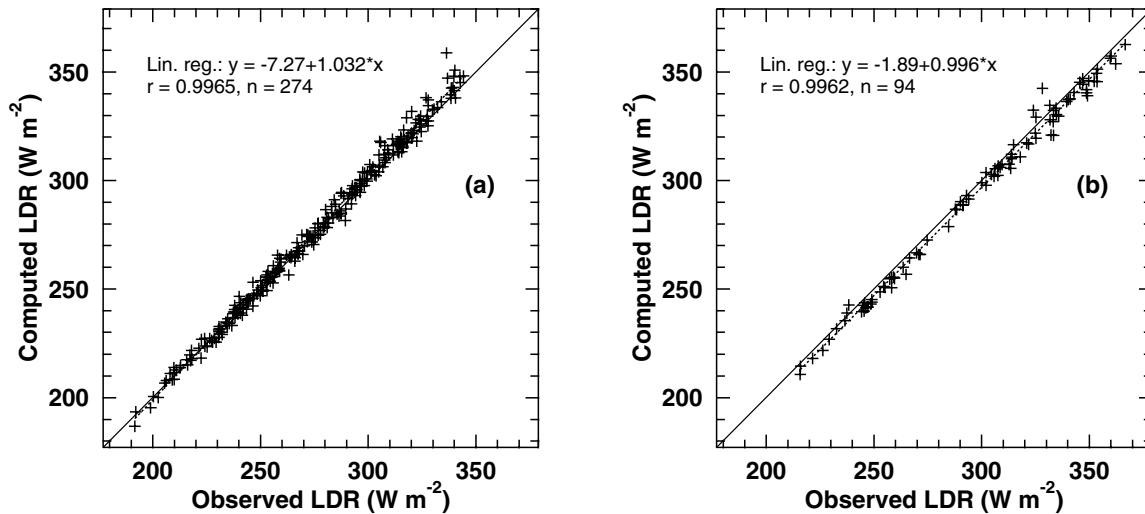


**Figure 6.2:** Results from *LDR* model run 1. are compared to (a) 274 night- and (b) 94 daytime ASRB observations in Payerne from 1996–2001.

during daytime. Thus it is probable that the set of nighttime cases is a mixture between cloud-free cases and cases with thin cirrus clouds. The influence of cirrus clouds on *LDR* was investigated using MODTRAN (see Section 4.3). These investigations showed that the effect of cirrus clouds on *LDR* is small. Additionally the standard deviations for night- and daytime *LDR* differences in Tab. 6.3 are very similar. This also indicates that nighttime cases with thin cirrus clouds hardly have any effect on *LDR* at the Earth's surface.

#### Uncertainty of *LDR* Comparison in Payerne

On the observational side the ASRB pyrgeometers measuring the *LDR* were modified at PMOD/WRC to improve uncertainty to  $\pm 2 \text{ W m}^{-2}$  (Philipona *et al.*, 1995). With regard to absolute measurements this uncertainty was confirmed during the first and second international pyrgeometer and absolute sky-scanning radiometer comparison (Philipona *et al.*, 2001, Marty *et al.*, 2003), where pyrgeometers, Atmospheric Emitted Radiance Interferometer (AERI) and radiation transfer model calculations were compared to absolute sky-scanning radiometer (ASR) measurements (Philipona, 2001).

On the modelling side numerous parameters influence the MODTRAN *LDR* computation. Table 6.5 gives an overview of the *LDR* sensitivity of MODTRAN for various input parameters. Table 6.6 shows mean temperature within the first km and column Integrated Water Content (*IWC*) for all night- and daytime cases used for the sensitivity study. The SRS 400 radiosonde used in Payerne has an absolute uncertainty of  $\pm 0.1 \text{ K}$  for the temperature sensor and  $\pm 2\%$  for the relative humidity sensor (Richner, 1999). The sum of sensitivities (a) and (b) in Tab. 6.5 explains 1.2 to  $1.3 \text{ W m}^{-2}$  of the uncertainty for the *LDR* comparison in Payerne (Fig. 6.2). Aerosol properties are modified by the inclusion of the surface meteorological range *V*. The sensitivities (l) and (m) for *V* don't vary linearly with  $\pm 5 \text{ km}$  changes and contribute up to  $0.7 \text{ W m}^{-2}$  to the *LDR* comparison uncertainty. Only minor contributions to the *LDR* comparison uncertainty in the order of  $0.1$  to  $0.2 \text{ W m}^{-2}$  are expected from the two observed greenhouse gases  $\text{CO}_2$  and ozone.

Assuming that all mentioned uncertainties are independent from each other, we can sum the observational ( $2 \text{ W m}^{-2}$ ) and modelling uncertainties together ( $2 + 1.3 + 0.7 + 0.2$ ) and we get a maximum (worst case) uncertainty for *LDR* model run 1. of  $4.2 \text{ W m}^{-2}$ . The combined standard uncertainty (root

**Table 6.5:** Mean sensitivities of MODTRAN longwave downward radiation (*LDR*) computations. 274 cloud-free nighttime (23 UTC) and 94 cloud-free daytime (11 UTC) sounding profiles in Payerne from 1996 to 2001 were individually modified. Mean *LDR* sensitivities and standard deviation were separately calculated for night- and daytime. Sensitivities are given in  $W m^{-2}$ .

Parameter	Modification	Nighttime-Sensitivity		Daytime-Sensitivity	
		Mean	Stdev	Mean	Stdev
(1 a.) Temperature <sup>a</sup>	±0.1K	±0.58	0.12	±0.61	0.11
(1 b.) Rel. humidity	±2%	±0.72	0.27	±0.74	0.25
(2 a.) Temperature <sup>b</sup>	±0.1K	±0.31	0.12	±0.35	0.06
(2 b.) Abs. humidity	±0.1gm <sup>-3</sup>	±0.54	0.10	±0.60	0.12
(3 a.) Temperature <sup>c</sup>	±0.1K	±0.24	0.05	±0.24	0.05
(3 b.) Abs. humidity	±0.1gm <sup>-3</sup>	±1.98	1.77	±1.97	1.24
(4) CO <sub>2</sub>	±10%	±0.33	0.08	±0.43	0.08
(5) Ozone	±10%	±0.17	0.05	±0.18	0.05
(6) Aerosols	-100%	-2.07	0.50	-1.37	0.27
(7 a.) <i>V</i> <sup>d</sup>	-5km	0.71	0.20	0.25	0.07
(7 b.) <i>V</i>	+5km	-0.43	0.12	-0.18	0.05

<sup>a</sup>Modification from surface up to tropopause

<sup>b</sup>Modification linearly decreasing to zero within first 4 km of the sounding profile

<sup>c</sup>Same then <sup>b</sup>, but calculation starting at 3000 m a.s.l.

<sup>d</sup>Surface meteorological range

**Table 6.6:** Mean temperature (*T*) within the first km above given altitude and total Integrated Water Content (*IWC*) up to 100 km a.s.l. from night- and daytime soundings used for sensitivity study (Tab. 6.5) in Payerne.

		0.49 km a.s.l		3 km a.s.l	
		<i>T</i> (K)	<i>IWC</i> (mm m <sup>-2</sup> )	<i>T</i> (K)	<i>IWC</i> (mm m <sup>-2</sup> )
Daytime	N	280.3	14.42	273.2	3.25
Night	274	280.3	14.42	273.2	3.25
Day	94	289.9	13.26	275.1	3.10

sum of squares) results to  $2.5 W m^{-2}$ , which is smaller than the found mean standard deviations shown in Tab. 6.3 for 274 night- and 94 daytime cloud-free cases. This indicates that further inaccuracies exist, e.g. a too coarse vertical resolution of temperature and humidity profiles in the first 100 m, where about 60% of *LDR* are originating from (Ohmura, 2001).

Differences of modelled and observed *LDR* show a positive linear trend to overestimate *LDR* at higher ambient temperatures. Further comparisons are needed to investigate whether this positive trend is caused by MODTRAN, by the involved meteorological data or by inaccuracies of the *LDR* measurements.

#### 6.4.2 Experiment 2.: Comparison of MODTRAN and aLMo Radiative Transfer Model

Results from model runs 2. and 3. are shown in Figure 6.3 and statistics are given in Table 6.3. *LDR* values from both model runs are height corrected. The aLMo forecast (model run 3.) substantially underestimates *LDR* by about  $20 W m^{-2}$  for nighttime. *LDR* differences decrease towards warmer ambient temperature (Fig. 6.3a). An even more pronounced decrease of the *LDR* differences towards higher ambient temperatures is indicated in Fig. 6.3b) for daytime. Hence a strong diurnal cycle of the

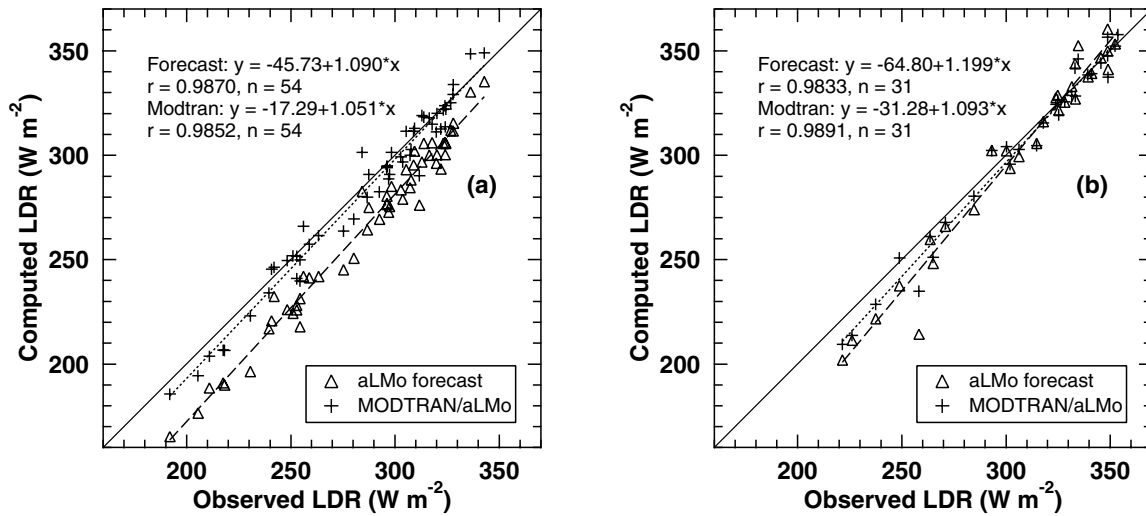


**Figure 6.3:** MODTRAN computed LDR using +11 hours aLMo profile- (model run 2.) and aLMo LDR forecasts (model run 3.) compared to (a) night- and (b) daytime ASRB observations in Payerne for 2000–01.

mean LDR difference is indicated for aLMo LDR forecasts compared to observations.

Similar results are obtained for LDR comparison at six ASRB stations (Tab. 6.8): the application of aLMo forecasted vertical profile within MODTRAN (model run 4.) and height correction of computed LDR values results in a strongly reduced bias and uncertainty ( $-2.4 \pm 5.7 \text{ W m}^{-2}$ ) compared to the mean aLMo LDR forecast (model run 5.) bias and uncertainty ( $-27 \pm 7.7 \text{ W m}^{-2}$ ).

MODTRAN computed LDR in Payerne using the same aLMo vertical profile (model run 2.) than aLMo uses to forecast LDR delivers substantially reduced LDR differences and a smaller positive linear trend compared to aLMo forecasts. Further investigations revealed that the best correlation for LDR differences  $\Delta LDR_{\text{aLMo-ASRB}}$  (aLMo forecast minus observation) is found with IWC ( $\text{mm m}^{-2}$ ) of the first km above the surface. The linear regressions are  $\Delta LDR_{\text{aLMo-ASRB}} = -13.7 + 1.68 \text{ IWC}$ ,  $r = 0.52$  for daytime and  $\Delta LDR_{\text{aLMo-ASRB}} = -9.9 + 1.01 \text{ IWC}$ ,  $r = 0.40$  for nighttime. Hence the mean LDR bias between aLMo forecast and observation reduces by about  $1 \text{ W m}^{-2}$  for an increase of IWC by  $1 \text{ mm m}^{-2}$ . Although the correlation  $r = 0.40$  is very weak for nighttime, there seem to exist insufficiencies in the description of the water vapour absorption/emission in the aLMo radiative transfer scheme compared to MODTRAN transfer calculations (see Tab. 6.3, run 2.).

### Example Day for Cloud-Free Conditions in Payerne

LDR model runs 2. and 3. base on the same vertical profile forecasted by aLMo. The representation of aerosols and gas concentrations of carbon dioxide and ozone is slightly different between MODTRAN and aLMo. These small model differences are assumed to produce mean LDR biases smaller than  $1 \text{ W m}^{-2}$  using sensitivities (4), (5) and (6) in Tab. 6.5.

Our application of MODTRAN incorporates the skin temperature of the ground as described in section 6.3.3. The aLMo radiation scheme, however, uses the ground temperature forecasted by the aLMo soil model as the surface boundary condition (Ritter and Geleyn, 1992). The hourly outputs for aLMo vertical profiles and aLMo forecasts allowed to compare cloud-free diurnal cycles of LDR and temperature in Payerne.

The 25th of June 2001 is shown in Fig. 6.4 as an example for an observed and forecasted cloud-free

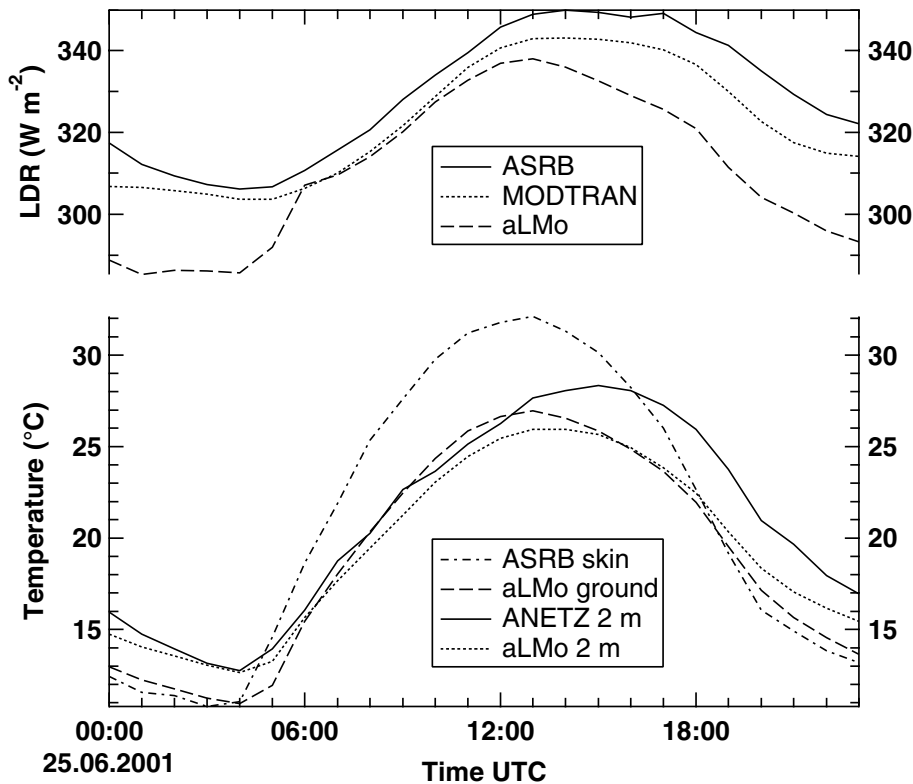


**Figure 6.4:** Cloud-free diurnal cycle of longwave downward radiation (*LDR*) and ground and 2 m temperatures in Payerne at 25th of June 2001. MODTRAN *LDR* was calculated with model run 2., and aLMO *LDR* with model run 3.

day. Measured ASRB skin temperatures calculated from observed *LUR* using Stefan-Boltzmann's law with emissivity equal one and ANETZ 2 m temperatures show large differences up to 6 K. However, aLMO forecasted ground and 2 m temperatures follow each other within  $\pm 2$  K. Thus the aLMO ground temperature reacts slower to fast temperature changes at the surface due to strong insolation compared to the skin temperature calculated from ASRB *LUR* measurements. The aLMO forecast (model run 3.) underestimates *LDR* for colder temperatures in the order of  $-25$  to  $-30$   $\text{W m}^{-2}$  with the maximum deviation around midnight. The minimum offset with  $-5$   $\text{W m}^{-2}$  is reached between sunrise and noon. aLMO *LDR* and air temperature decline too early after solar noon compared to ASRB and ANETZ measurements. The MODTRAN *LDR* calculation using aLMO vertical profile forecasts (model run 2.) delivers smaller negative *LDR* biases between  $-3$  and  $-10$   $\text{W m}^{-2}$ . Larger differences are also found in the afternoon. Thus the aLMO vertical profile forecast is possibly too cold and/or too dry all over the day. This is further discussed in the following section.

The small negative *LDR* biases found for MODTRAN/aLMO computations (Figs. 6.3 and 6.4) suggest that the large negative offset of aLMO *LDR* forecasts is not primarily caused by temperature and/or humidity biases in the aLMO profile forecasts.

### 6.4.3 Experiment 3.: Comparison of Measured and Forecasted Vertical Profiles

Results from model runs 1. and 2. (see Tab. 6.3) were used to investigate the influence of measured and forecasted vertical profiles on *LDR* differences in Payerne. Aerosol properties and greenhouse gas concentrations were identical for both MODTRAN runs. The average temperature and absolute

humidity conditions within the first km above surface are given in Tab. 6.7. *LDR* values from model run 2. had to be height corrected. For nighttime aLMO slightly underestimates both the temperature and the absolute humidity near the surface. The sensitivities for MODTRAN input parameters (Tab. 6.5) allow to estimate the *LDR* bias caused by temperature and humidity differences. The expected *LDR* difference relative to the sounding meteorological conditions is calculated using sensitivity (2 a.) for temperature, and sensitivity (2 b.) for absolute humidity. Added together the estimated irradiance differences due to temperature and humidity differences agree within  $\pm 1.5 \text{ W m}^{-2}$  to the differences between model run 1. and 2. in Tab. 6.3 for night- and daytime. Hence, differences between measured and modelled temperature and humidity vertical profiles explain most of the *LDR* biases.

**Table 6.7:** Average temperature ( $T$ ) and absolute humidity ( $U$ ) within the first km of the sounding- and aLMO profiles from 54 cloud-free night- (23 UTC) and 30 cloud-free daytime (11 UTC) cases in Payerne from 2000–01. Resulting irradiance difference is defined by multiplying the differences with the accordant sensitivity for temperature (2 a.) and absolute humidity (2. b) in Tab. 6.5.

Profile	Night		Day	
	$T$ (°C)	$U$ (g m <sup>-3</sup> )	$T$ (°C)	$U$ (g m <sup>-3</sup> )
Radiosonde	11.34	7.44	14.08	6.66
aLMO	10.58	6.49	12.90	7.14
Difference	-0.76	-0.95	-1.18	0.48
Irradiance difference (W m <sup>-2</sup> )	-2.4	-5.2	-4.1	2.9

Model run 1. revealed a mean bias of  $-3.2 \text{ W m}^{-2}$  (Tab. 6.3, Fig. 6.2b) in Payerne for daytime. The sounding mean absolute humidity of the first km is about 7% lower than the mean absolute humidity of the aLMO vertical profile for daytime (Tab. 6.7). This may indicate that the radiosonde humidity sensor underestimated the water vapour content near the surface for cloud-free conditions with strong insolation. Results shown by Haase *et al.* (2003) also indicate a sounding dry bias. However further investigations are needed to compare different measurements of the cloud-free water vapour content in the lower atmosphere.

#### 6.4.4 Experiment 4.: Insertion of Measured Surface Data

Payerne sounding profiles were applied together with MODTRAN to calculate *LDR* at six ASRB stations for cloud-free night- and daytime cases from 1996 to 2001. Thus compared to the results in Table 6.4, where only cases with accordant aLMO forecasts could be investigated, a larger number of cloud-free situations was available for night- and also daytime. Model run 5. uses the original vertical profile at the accordant ASRB height. Model run 6., however, calculates *LDR* with a modified vertical profile with measured surface meteorological parameters inserted (see section 6.3.3). Table 6.8 summarizes results of *LDR* comparison at different ASRB sites.

Results of model run 5. show that the application of original sounding values leads to a mean positive bias of  $3.1 \text{ W m}^{-2}$  for nighttime, and a strong mean underestimation of  $-9.4 \text{ W m}^{-2}$  for daytime. The local daytime atmosphere over the Alps is strongly influenced by thermal convection caused by strong insolation. Local daytime conditions are particularly different from Payerne sounding profile at ASRB station Cimetta, which is located on the south side of the Alps. Stdev's are rather high both for night- and daytime, and thus the accuracy of *LDR* calculation for cloud-free situations using sounding data is low. Model run 6. additionally applies measured surface meteorological parameters to take local effects

**Table 6.8:** Mean *LDR* difference (computed minus observed) and mean standard deviation for about 59 nighttime- and 25 daytime cases for six ASRB stations from 1996 to 2001. Values are given in  $W m^{-2}$ .

Sta	MODTRAN/sond (5.)				MODTRAN/sond_ins (6.)			
	Nighttime		Daytime		Nighttime		Daytime	
	Diff	Stdev	Diff	Stdev	Diff	Stdev	Diff	Stdev
DAV	8.8	7.4	-11.0	9.4	-4.1	5.9	-5.1	8.0
CIM	-3.6	8.3	-17.9	12.3	-5.5	6.2	-14.6	9.8
MAE	2.8	8.9	-7.5	9.9	1.2	8.1	-4.0	7.8
VSF	2.7	9.5	-5.4	11.5	-1.0	7.5	-4.5	8.6
GOR	4.5	8.8	-5.1	9.1	3.5	8.5	-1.6	8.1
JFJ	3.1	8.4	-9.5	8.3	1.5	7.7	-9.4	7.9
Avg	3.1	8.6	-9.4	10.1	-0.7	7.4	-6.5	8.4

into account. The accuracy of modeled *LDR* is improved in the order of 1 to 2  $W m^{-2}$  for night- and daytime, and mean *LDR* differences are reduced by 2.4, respectively 2.9  $W m^{-2}$  for night- and daytime.

Similar effects of surface parameter insertion are also found for aLMo vertical profiles in Payerne (Tab. 6.3, runs 2. and 4.), and at six ASRB stations (Tab. 6.4, runs 7. and 9.). Accuracies are improved between 1.3 and 2.8  $W m^{-2}$ , and mean *LDR* differences are reduced in the order of 1  $W m^{-2}$ .

The application of modified aLMo forecasted vertical profiles (model run 9.) instead of modified Payerne soundings (model run 6.) improves the mean accuracy of *LDR* computation from 6.1 to 4.4  $W m^{-2}$  (Tab. 6.4). This accuracy is equal to the nighttime accuracy of MODTRAN *LDR* calculations using sounding data at Payerne (Tab. 6.4). Hence MODTRAN *LDR* computations using aLMo forecasted vertical profiles and measured surface data at six ASRB stations performs similarly compared to modeled *LDR* in Payerne using measured sounding profiles. Altitude differences between aLMo grid-points and ASRB stations can therefore be addressed successfully with the insertion of local surface measurements.

## 6.5 Summary

Cloud-free longwave downward radiation (*LDR*) obtained from the Alpine Surface Radiation Budget (ASRB) was compared to *LDR* calculations from two different radiative transfer models (RTMs). The first RTM is MODTRAN v4.0, which approximates the absorption bands with a moderate resolution. The second RTM is part of the numerical weather prediction model “aLMo” at MeteoSwiss and is restricted to a low number of absorption bands due to computational efficiency. Four different *LDR* experiments were carried out: 1. to test the performance of the MODTRAN; 2. to compare both RTMs using the same atmospheric input data; 3. to assess the quality of atmospheric input data; and 4. to investigate the influence of measured surface data in MODTRAN.

Experiment 1. revealed that MODTRAN v4.0 computed *LDR* using Payerne soundings agrees well with ASRB *LDR* observations in Payerne with  $1.5 \pm 3.5 W m^{-2}$  mean difference (modelled minus observed) for nighttime, and  $-3.2 \pm 3.6 W m^{-2}$  mean difference for daytime from 1996 to 2001. The slightly larger bias for daytime is possibly caused by a dry bias of the radiosonde at noontime. Sensitivities for various MODTRAN input parameters were determined for night- and daytime and an estimate of the mean *LDR* modelling uncertainty equal to 2.5  $W m^{-2}$  was found. This uncertainty estimate is about 1  $W m^{-2}$  lower than the uncertainty determined for Payerne and indicates that uncertainty estimates for some of the parameters may be too low for cloud-free conditions.



Large differences between aLMo *LDR* forecasts and observations in the order of  $-20$  to  $-25 \text{ W m}^{-2}$  were found from experiment 2. for Payerne and six other ASRB stations. The *LDR* bias shows a strong diurnal and annual cycle with a maximum bias for cold and dry atmospheric conditions. However MODTRAN computed *LDR* using the same aLMo vertical profile forecast shows a negative offset in the order of  $-3 \text{ W m}^{-2}$  only, indicating slightly too cold and/or too dry conditions in the forecasted vertical profile. The aLMo forecast bias is weakly correlated ( $r \approx 0.45$ ) to the mean sounding Integrated Water Content (*IWC*) of the first km above the surface. Thus the large *LDR* bias could be caused on the one hand by insufficiencies in the description of water vapour absorption/emission in the aLMo radiative transfer model, and by underestimation of temperature and/or humidity in the aLMo vertical profile forecast on the other hand. About 80% of the bias is due to inaccuracies in the model absorption, and about 20% due to biases in temperature and humidity in the aLMo vertical profile forecast.

Differences of mean temperature and humidity conditions at the surface and within the first km above surface explain most of the *LDR* differences between MODTRAN *LDR* computations and observations in experiment 3., where soundings or aLMo vertical profiles were applied as input data. Vertical profile forecasts from aLMo for cloud-free situations are slightly too cold and too dry leading to a mean negative *LDR* of about  $-3 \text{ W m}^{-2}$  from MODTRAN calculations. Sounding data is accurate for nighttime, but is probably also too dry for cloud-free conditions during daytime.

The insertion of local surface meteorological parameters in soundings or aLMo profiles improved uncertainty of *LDR* differences between model and observation in experiment 4. by about 1 to  $2 \text{ W m}^{-2}$ , and also reduced mean *LDR* differences. The combination of aLMo forecasted vertical profiles and surface data with MODTRAN at six ASRB stations provides accurate *LDR* computations with uncertainty comparable to Payerne, where soundings were available as atmospheric input data.



## Chapter 7

# Greenhouse Effect in the Alps

### 7.1 Introduction

The mean global temperature rise at the Earth's surface during the past decades is most likely related to an enhanced greenhouse effect (*Mitchell et al., 1995, Tett et al., 1999, Houghton et al., 2001*). First observational determinations of the cloud-free greenhouse effect and top of the atmosphere (ToA) cloud effect are based on satellite measurements (*Raval and Ramanathan, 1989, Gupta et al., 1993, Inamdar and Ramanathan, 1997, Slingo et al., 1998*). Recent studies (*Philipona et al., 2004a,b*) investigate the greenhouse- and cloud effect at the Earth's surface based on ASRB radiation measurements in the Alps.

In the following sections a detailed study of the surface radiation budget at two ASRB stations from 1995 to 2003 is presented with a special focus on the effect of clouds and surface albedo. Further the cloud-free and all-sky greenhouse effect is determined with the help of measured longwave upward radiation (*LUR*) at the surface, MODTRAN computed ToA longwave outgoing radiation (*LOR*) and longwave cloud effect (*LCE*) at the surface.

### 7.2 Greenhouse- and Cloud Radiative Effect

The greenhouse effect (*G*) is defined as the longwave upward radiation (*LUR*) from the Earth's surface at a certain location minus the longwave outgoing radiation (*LOR*) leaving the Earth at ToA above that location (*Raval and Ramanathan, 1989*). The all-sky greenhouse effect (*G<sub>all</sub>*) at the Earth's surface is defined as (*Philipona et al., 2004a*):

$$G_{\text{all}} = G_{\text{cfr}} + LCE, \quad (7.1)$$

where *G<sub>cfr</sub>* is the cloud-free greenhouse effect, and *LCE* the longwave cloud effect at the surface. To describe the effects of clouds on surface observations, the cloud radiative forcing (*CF*) has been defined by *Charlock and Ramanathan (1985)*. The term "cloud forcing" was substituted by "cloud effect", because the term "forcing" should be used to indicate parameters which tend to disturb a given equilibrium. Therefore the net cloud effect *NCE* at the Earth's surface is defined as:

$$NCE = TNR_{\text{all}} - TNR_{\text{cfr}}, \quad (7.2)$$

where *TNR* is the total net radiation at the surface. Cloud-free conditions were evaluated with the help of the Automatic Partial Cloud Amount Detection Algorithm (APCADA, see chapter 4). Ten minutes values with zero octa partial cloud amount were assumed to be cloud-free. The total net radiation at the

surface is calculated from the net shortwave and longwave fluxes:

$$TNR = SNR + LNR, \quad (7.3)$$

$$= (SDR - SUR) + (LDR - LUR), \quad (7.4)$$

$$= THR - LUR, \quad (7.5)$$

where  $SDR$  and  $SUR$  are shortwave downward, respectively upward radiation,  $LDR$  the longwave downward radiation, and  $THR$  is the total heating radiation. Therefore  $NCE$  can be written also as the sum of a shortwave and longwave part:

$$NCE = SCE + LCE, \quad (7.6)$$

where  $SCE$  and  $LCE$  are the shortwave, respectively longwave cloud radiative effect.  $SCE$  is calculated from all-sky and cloud-free shortwave net radiation ( $SNR$ ) with  $SCE = SNR_{\text{all}} - SNR_{\text{cfr}}$ . The same applies also for  $LCE$ . The determination of  $SCE$  and  $LCE$  has one major problem: the cloud-free moments are irregularly distributed with time, which affects both  $SNR_{\text{cfr}}$  and  $LNR_{\text{cfr}}$ . Thus  $SNR$  values were first transformed to a net transmissivity  $q_{\text{net}}$  using Eq. 3.3 with  $SNR$  instead of  $SDR$ , and the annual mean all-sky and cloud-free net transmissivities  $q_{\text{net,all}}$  and  $q_{\text{net,cfr}}$  were calculated. Finally the annual mean values for  $q_{\text{net,all}}$  and  $q_{\text{net,cfr}}$  were then transformed back to  $SNR_{\text{all}}$  and  $SNR_{\text{cfr}}$  with the help of Eq. 3.3 for every ten minutes value throughout the year, and the annual mean values of  $SNR_{\text{all}}$  and  $SNR_{\text{cfr}}$  were computed. A similar procedure was applied also for  $LCE$ :  $LNR$  values were first transformed to a modified net Cloud-Free Index ( $CFI_{\text{net}}$ ) with the help of Eqs. 4.10 and 4.2:

$$CFI_{\text{net}} = \frac{\epsilon_A \sigma T^4 - LUR}{\epsilon_{AC} \sigma T^4 - LUR}, \quad (7.7)$$

$$= \frac{LNR}{\epsilon_{AC} \sigma T^4 - LUR}. \quad (7.8)$$

Then annual mean values of  $CFI_{\text{net,all}}$  and  $CFI_{\text{net,cfr}}$  were calculated, and finally transformed back to annual mean values of  $LNR_{\text{all}}$  and  $LNR_{\text{cfr}}$  as described before for  $SCE$ .

### 7.2.1 Modelling of Greenhouse Effect

The radiative transfer model MODTRAN (see section 6.3.1) proved to be able to compute cloud-free longwave downward radiation ( $LDR_{\text{cfr}}$ ) very accurately using sounding profiles and surface temperature and humidity (see section 6.4.1). Thus MODTRAN was assumed to be able to compute also the cloud-free longwave outgoing radiation ( $LOR_{\text{cfr}}$ ) at ToA. Measured cloud-free sounding profiles and  $LUR$  from 274 night- and 94 daytime cases in Payerne (1996–2001) were assimilated in MODTRAN as described in section 6.3.3, and  $LOR_{\text{cfr}}$  was computed above Payerne. Payerne sounding profiles and measured surface parameters from 59 night- and 25 daytime cloud-free cases (1996–2001) were used to compute  $LOR_{\text{cfr}}$  above the ASRB station SLF-Versuchsfeld. The cloud-free greenhouse effect ( $G_{\text{cfr}}$ ) can now be found if  $LOR_{\text{cfr}}$  is subtracted from the measured cloud-free longwave upward radiation ( $LUR_{\text{cfr}}$ ) at the surface. Figure 7.1 shows the relations between  $G_{\text{cfr}}$  and  $LUR_{\text{cfr}}$  for Payerne during day- and nighttime. The correlation coefficients for the four relations are between 0.968 (Payerne, nighttime) and 0.996 (Versuchsfeld, daytime). The standard deviations of residuals to the linear regression trend line are 4.1  $\text{W m}^{-2}$ , respectively 5.1  $\text{W m}^{-2}$  for night- and daytime in Payerne, and 3.0  $\text{W m}^{-2}$ , respectively 4.0  $\text{W m}^{-2}$  for night- and daytime at SLF-Versuchsfeld.

The main reason for the very high correlation between the cloud-free greenhouse effect ( $G_{\text{cfr}}$ ) and cloud-free longwave upward radiation ( $LUR_{\text{cfr}}$ ) at the Earth's surface is the dominant role of  $LUR_{\text{cfr}}$  within the  $LOR_{\text{cfr}}$  spectrum. Figure 7.2 shows an example for  $LUR_{\text{cfr}}$  spectra at different heights in the atmosphere.  $LOR_{\text{cfr}}$  is still dominated by the surface emission in the atmospheric window, i.e. from 8

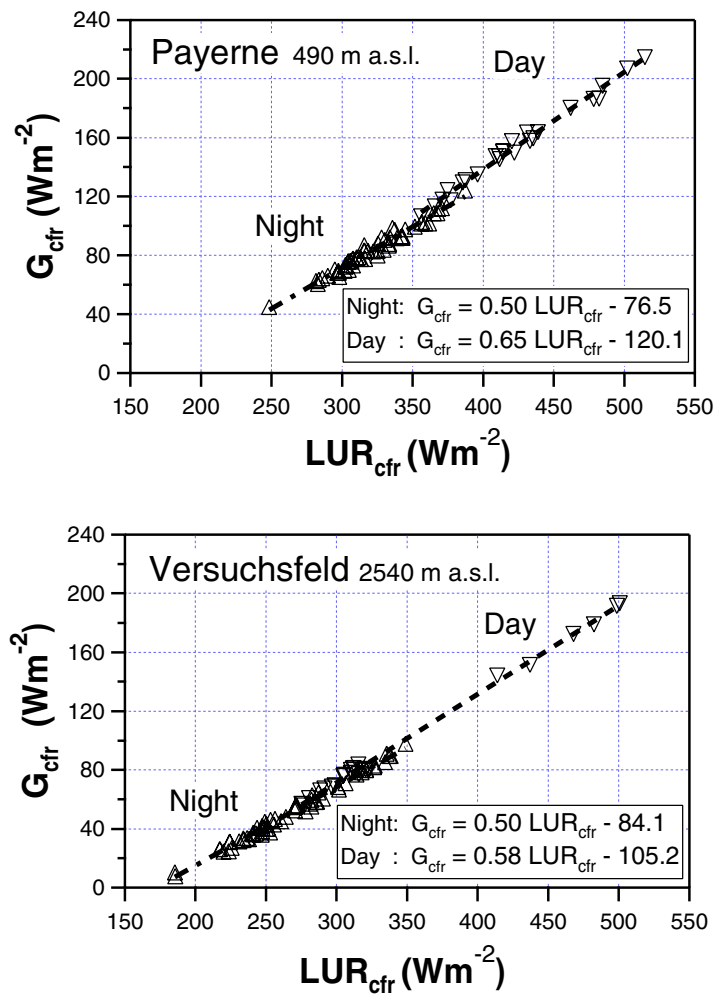


**Figure 7.1:** MODTRAN computed cloud-free greenhouse effect ( $G_{cfr}$ ) versus measured cloud-free longwave upward radiation ( $LUR_{cfr}$ ) at two ASRB stations during day- and nighttime.

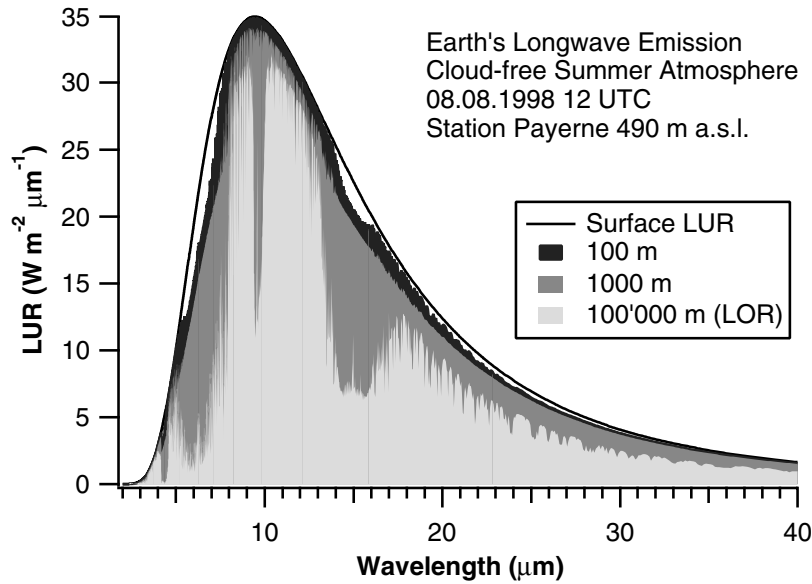


**Figure 7.2:** Cloud-free Longwave upward radiation ( $LUR_{\text{cfr}}$ ) spectra seen from different levels above ground in Payerne. The cloud-free longwave outgoing radiation ( $LOR_{\text{cfr}}$ ) at the top of atmosphere (ToA) is dominated by surface emission in the atmospheric window (8–12  $\mu\text{m}$ ).

to 12  $\mu\text{m}$ . The  $LOR_{\text{cfr}}$  spectrum mainly differs from the surface emission spectrum in the near water vapour bands around 6  $\mu\text{m}$  and in the broad  $\text{CO}_2$  band at 15  $\mu\text{m}$ .

### 7.3 Surface Radiation Balance

The ASRB stations Payerne, Davos and SLF-Versuchsfeld are additionally equipped with instruments to measure the reflected shortwave and outgoing longwave radiation. Outgoing fluxes in Payerne are provided by the BSRN station and were available from 1995 to 2002. The outgoing fluxes in Davos were measured a few hundred meters apart from the observatory in Davos down on a field near the lake of Davos until end of 2002. Thus only measurements from the low-land site Payerne (490 m a.s.l.) and from the alpine site SLF-Versuchsfeld (2540 m a.s.l.) were applied to investigate in detail several radiation and surface meteorological quantities from 1995 to 2003.

*Philipona et al.* (2004a) show that the period 1995–2002 is characterised by a strong increase of 2 m temperature (+0.82°C) and absolute humidity (+0.21  $\text{g m}^{-3}$  or +4.4%) at eight ASRB stations from Locarno-Monti (370 m a.s.l.) to Jungfrauoch (3580 m a.s.l.). How are temperature and water content changes related to the radiation balance at the surface? Figure 7.3 shows the time evolution of annual mean radiation quantities in Payerne (1995–2002) and at SLF-Versuchsfeld (1996–2003). The longwave upward radiation ( $LUR$ ) and total heating radiation ( $THR$ ) (see section 7.2) are increasing in the order of 5 to 10  $\text{W m}^{-2}$  at both stations (Figures 7.3 a) and e)). A two-side t-test with seven degrees of freedom was applied to test whether the increasing trend was significantly different from zero (P-value > 0.95). All  $THR$  and  $LUR$  increases are significant except for  $THR$  at Payerne, where the P-value was 0.89 only. The total net radiation ( $TNR$ ) is almost constant in Payerne (PAY), but increasing at SLF-Versuchsfeld (VSF) especially due to the exceptionally warm summer in the year 2003.

Which radiation quantities cause the increase of  $THR$ ? Figures 7.3 b) and f) show the all-sky shortwave net radiation ( $SNR$ ) and surface albedo ( $= 100 \frac{SUR}{SDR}$ ). Albedo was computed for solar zenith angles  $\theta < 80^\circ$  only. Albedo has decreased at both stations, with an extreme low value of about 54% at VSF

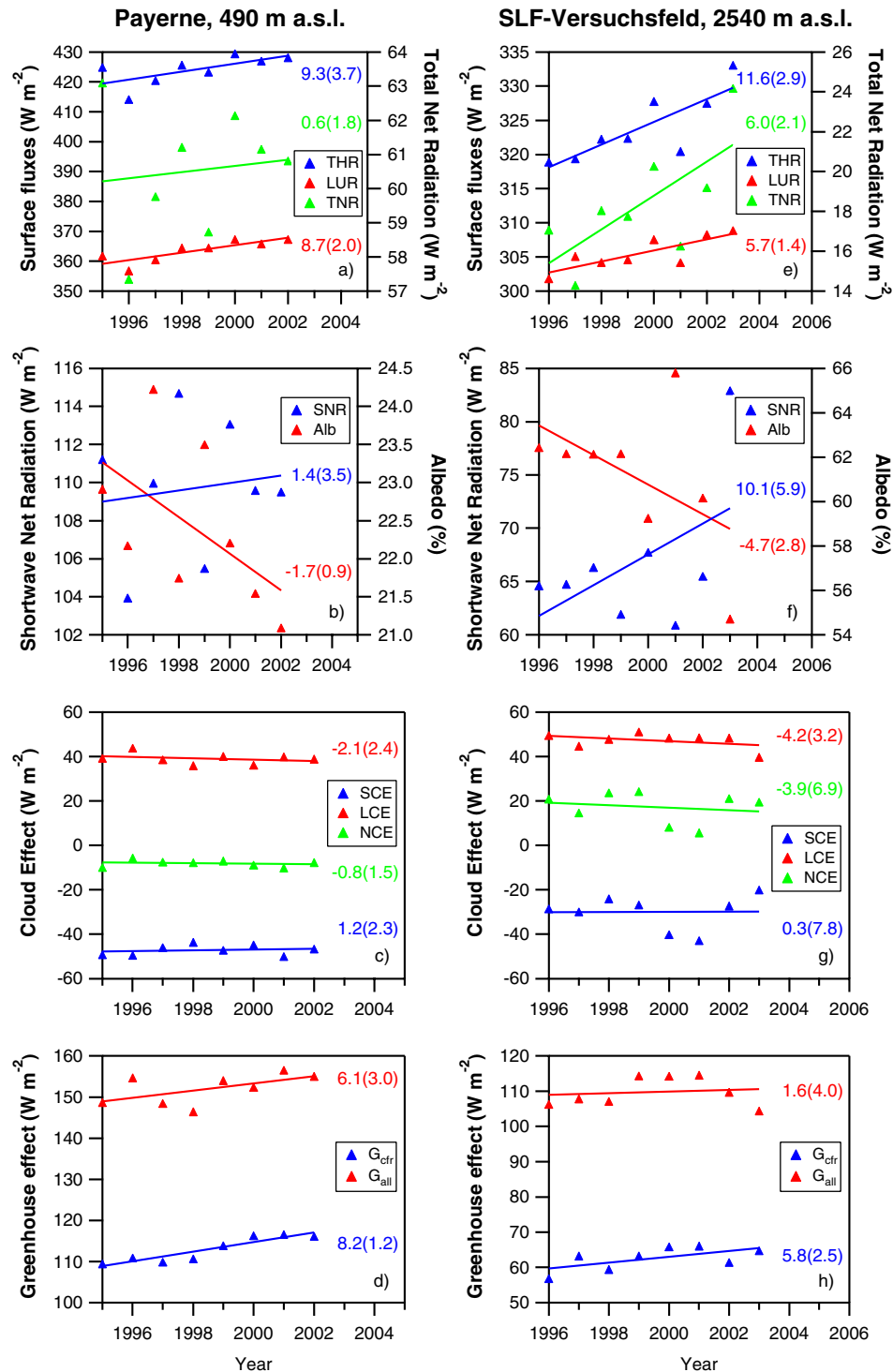


**Figure 7.3:** Annual mean all-sky values of shortwave net radiation (SNR), albedo (Alb), total heating radiation (THR), longwave upward radiation (LUR), total net radiation (TNR), shortwave and longwave cloud effect (SCE;LCE), net cloud effect (NCE), cloud-free and all-sky greenhouse effect ( $G_{cfr}$ ;  $G_{all}$ ). Numbers indicate changes over the periods with values in parenthesis representing the standard deviation of residuals to the linear regression trend line.

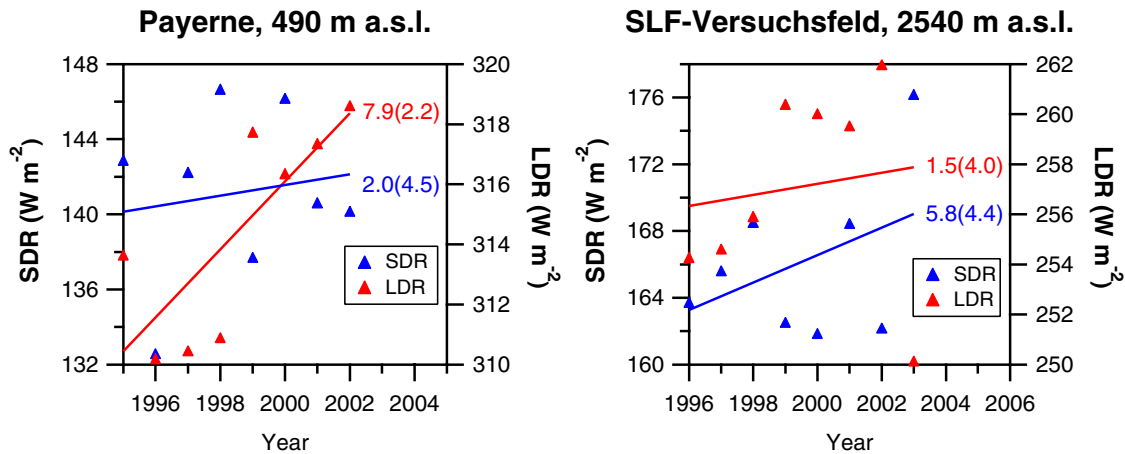


**Figure 7.4:** Annual mean all-sky values of shortwave downward radiation ( $SDR$ ) and longwave downward radiation ( $LDR$ ). Numbers indicate changes over the periods with values in parenthesis representing the standard deviation of residuals to the linear regression trend line.

in 2003. The number of days with snow cover (daily maximum of albedo  $> 60\%$ ) in Payerne decreased from about 22 days in 1995 to 8 days in 2002, i.e. a reduction of more than 60%. However days with snow cover in Payerne occur during wintertime, where  $SDR$  is rather low, and a change of snow cover duration hardly affects the annual mean shortwave net radiation ( $SNR$ ). At VSF the duration of snow cover shortened from about 287 days in 1996 to 268 days in 2003, i.e. a reduction of 6.3%. In contrast to Payerne the reduction of snow cover takes place in summer where  $SDR$  is large, and where a change of the albedo strongly influences  $SNR$ . Further investigations revealed that the change of albedo explains most of the increase of  $SNR$  at both locations. Therefore the net change of the shortwave downward radiation ( $SDR$ ) and shortwave cloud effect ( $SCE$ ) has to be close to zero.

Which role play the clouds on the increase of  $THR$ ? Figures 7.3 c) and g) give the shortwave- ( $SCE$ ), longwave- ( $LCE$ ) and net ( $NCE$ ) cloud effect.  $SCE$  and  $LCE$  in Payerne both slowly converge towards zero, i.e. cloud cover slightly decreased from 1995 to 2002, but  $NCE$  remained almost stable for the whole period. Larger year-to-year variability of the different  $CE$  is indicated for VSF. The year 2003 clearly shows the compensating effect of  $LCE$  and  $SCE$ : less clouds means less reflection of  $SDR$  by clouds, but also less longwave emission by clouds. The trends of  $SCE$  for both stations are small, and therefore the change of shortwave downward radiation ( $SDR$ ) has to be small as mentioned before in the last paragraph. The net cloud effect ( $NCE$ ) at VSF decreases and thus clouds tend to damp the strong increase of  $THR$ .

The last remaining quantity left to cause the increase of the total heating radiation ( $THR$ ) is the longwave downward radiation ( $LDR$ ). Figure 7.4 shows annual mean all-sky  $SDR$  and  $LDR$  at Payerne and at SLF-Versuchsfeld.  $LDR$  regularly increases except for the year 2003, where the summer half year was dominated by cloud-free conditions.  $LDR$  dropped by about  $12 \text{ W m}^{-2}$  compared to the trend of the previous years. Similarly the longwave cloud effect  $LCE$  also dropped by about  $9 \text{ W m}^{-2}$ . Thus the strong negative  $LDR$  bias in 2003 is mainly caused by a change of cloudiness.  $SDR$  at VSF shows an accordant positive bias of about  $10 \text{ W m}^{-2}$  for 2003, but remained stable at PAY and at VSF for the other years.

The investigation of all-sky and cloud-free  $LDR$  at eight ASRB stations from 1995 to 2002 (Philipona *et al.*, 2004a) revealed that  $LDR_{\text{cfr}}$ , i.e.  $LDR_{\text{all-sky}} - LCE$ , uniformly increased by 3.2 to  $5.6 \text{ W m}^{-2}$  at all sites. Mean annual  $LDR_{\text{cfr}}$  and temperature values are highly correlated between 0.88 and 0.97. Philipona and Dürr (2004) show that a mean total increase of  $1.5 \text{ W m}^{-2}$  remains if the effect of in-



creased temperature on  $LDR_{\text{cfr}}$  is removed from 1995 to 2003. This remaining total increase is highly correlated (0.88) with the absolute humidity and corroborates the dominant role of water vapour for greenhouse radiative warming.

## 7.4 Greenhouse Effect in the Alps

In the previous section the increase of the cloud-free longwave downward radiation ( $LDR_{\text{cfr}}$ ) was found to be the largest contribution to the strong increase of total heating radiation ( $THR$ ) in the ASRB network. The day- and nighttime relations between cloud-free greenhouse effect ( $G_{\text{cfr}}$ ) and cloud-free longwave upward radiation ( $LUR_{\text{cfr}}$ ) in Figure 7.1 were used to calculate  $G_{\text{cfr}}$  from  $LUR_{\text{cfr}}$  measurements at the ASRB stations Payerne (PAY) and SLF-Versuchsfeld (VSF). The all-sky greenhouse effect  $G_{\text{all}}$  can then be found using Eq. 7.1, i.e. adding the longwave cloud effect ( $LCE$ ) to  $G_{\text{cfr}}$ . Figures 7.3 d) and h) show the all-sky and cloud-free greenhouse effect at PAY and VSF. A two-side t-test revealed a significant increase of  $G_{\text{cfr}}$  in PAY with a P-value of 0.98, but a not-significant increase of  $G_{\text{cfr}}$  at VSF with a P-value of 0.88. Increases of  $G_{\text{all}}$ , however, are smaller due to the decreasing longwave cloud effect ( $LCE$ ) at both sites.

*Philipona et al. (2004a)* show that  $LDR_{\text{cfr}}$  is also highly correlated with  $G_{\text{cfr}}$ . This fact was used to determine  $G_{\text{cfr}}$  from surface measurements of  $LDR_{\text{cfr}}$  at eight ASRB stations. The annual mean altitude gradient is  $-2.3 \text{ W m}^{-2}(100 \text{ m})^{-1}$  for  $G_{\text{cfr}}$ , and for  $G_{\text{all}}$   $-1.8 \text{ W m}^{-2}(100 \text{ m})^{-1}$ . Comparable results are found between Payerne (490 m a.s.l.) and SLF-Versuchsfeld (2540 m a.s.l.) for the altitude gradients of the greenhouse effect calculated from  $LUR$ :  $-2.0 \text{ W m}^{-2}(100 \text{ m})^{-1}$  for  $G_{\text{cfr}}$  and  $-1.7 \text{ W m}^{-2}(100 \text{ m})^{-1}$  for  $G_{\text{all}}$ .

## 7.5 Summary

A detailed surface radiation budget study at the low-land ASRB station Payerne (PAY) (490 m a.s.l.) and at the alpine ASRB station SLF-Versuchsfeld (VSF) (2540 m a.s.l.) revealed that

- the total heating radiation ( $THR$ ) and longwave upward radiation ( $LUR$ ) significantly increased over the period 1995 to 2003, but the total net radiation ( $TNR$ ) remained stable except for VSF in 2003,
- the length of snow cover duration and therefore the albedo substantially decreased at both stations, but the consequences of albedo reduction are more pronounced at VSF because the albedo decrease takes place mostly during summer,
- the change of albedo explains most of the all-sky shortwave net radiation ( $SNR$ ) increase, whereas the shortwave cloud effect ( $SCE$ ) and shortwave downward radiation ( $SDR$ ) remained stable,
- the longterm longwave and shortwave cloud effects tend to compensate each other with a remaining net cloud effect ( $NCE$ ) close to zero,
- the cloud-free greenhouse effect ( $G_{\text{cfr}}$ ) at the surface has substantially increased over Switzerland during the period 1995 to 2003,
- the all-sky greenhouse effect ( $G_{\text{all}}$ ) rises more slowly compared to  $G_{\text{cfr}}$  due to a slight decrease of the longwave cloud effect ( $LCE$ ),
- the altitude gradient of  $G_{\text{cfr}}$  is  $-2.0 \text{ W m}^{-2}(100 \text{ m})^{-1}$ , and  $-1.7 \text{ W m}^{-2}(100 \text{ m})^{-1}$  for  $G_{\text{all}}$ .



# Chapter 8

## Conclusions

### 8.1 Synthesis

The main objective of this thesis was to investigate changes of radiation balance, albedo and cloud- and greenhouse effect in the Alps. Emphasis was mainly laid on the investigation of longwave radiation fluxes.

The most important steps to fulfill these goals were the continuation of accurate radiation measurements within the ASRB network and the improvement and development of methods to guarantee high quality all-sky and cloud-free radiation data.

#### 8.1.1 Maintenance of ASRB Network

The stability of the data acquisition system in Davos could be improved and data loss reduced. The annual mean availability of radiation data is normally more than 98% at all ASRB sites. The shading effect of obstacles was re-evaluated for all ASRB sites. ASRB instruments were calibrated in situ with a Travelling Standard in 2000 and 2001. The comparison with a former calibration done by Ch. Marty in 1996/97 revealed that PIR pyrgeometers remained very stable all over the years.

#### 8.1.2 Detection of Cloud-Free Sky

The Clear-Sky Index (*CSI*) shows a systematic underestimation of cloud-free conditions during nighttime. A new version of *CSI*, the Cloud-Free Index (*CFI*), accounts for the diurnal and annual mean variation of the lapse rate at the surface to improve the detection of cloud-free sky. The Automatic Partial Cloud Amount Detection Algorithm (*APCADA*) was developed based on *CFI* and variability of the longwave downward radiation to provide real-time cloud cover estimates in octas and 24 hours a day. *APCADA* represents a robust and stable method for cloud cover detection tested from arctic to tropical sites, and cloud cover investigations are possible for existing longwave downward radiation time series.

#### 8.1.3 Estimation of Diffuse Shortwave Downward Radiation

The operating of *APCADA* requires the real-time correction of the direct sun influence on *LDR* measurements. However the direct solar radiation is not measured at ASRB, and the diffuse shortwave downward radiation ( $SDR_d$ ) was estimated from *SDR* instead. Comparisons with measurements of  $SDR_d$  in Payerne, Davos and SLF-Versuchsfeld showed reduced mean differences and uncertainty compared to the old  $SDR_d$  method based on the shading of the shadowband at solar noon. Therefore the shadowband is not further required at ASRB stations.

### 8.1.4 Homogenisation of *LDR* Time Series

The longterm reliability of *LDR* measurements is the key factor to detect changes of the greenhouse effect at the Earth's surface. Relocation of instruments with changing field of view, instrument modification or electronic failures in the data acquisition system may severely reduce the quality of *LDR* time series. A new method based on the Cloud-Free Index (*CFI*), and temperature and humidity measurements at the surface is presented, which is able to detect also small *LDR* inhomogeneities.

### 8.1.5 Longwave Downward Radiation Modelling

Radiative Transfer Models (RTMs) play an important role in General Circulation Models (GCMs) and Numerical Weather Prediction (NWP) models. RTMs often have to be simplified to reduce computation time. A simplified RTM used in the NWP model aLMo at MeteoSwiss was compared to cloud-free *LDR* computations with the complex radiative transfer model MODTRAN using observed sounding profiles from Payerne and aLMo forecasted atmospheric profiles. The longwave downward component of the RTM used in aLMo showed a negative bias in the order of  $-20 \text{ W m}^{-2}$  during nighttime, and a strong diurnal variation of the *LDR* bias. However the computation of MODTRAN *LDR* using aLMo atmospheric forecasts delivered a substantially reduced *LDR* error. Thus the aLMo radiative scheme itself has to be modified to improve *LDR* computation.

### 8.1.6 Radiation Budget, Cloud- and Greenhouse Effect

Radiation measurements from 1995 to 2003 allowed to investigate the year-to-year variation of several radiative components at the Earth's surface. The low-land ASRB station Payerne (490 m a.s.l.) and the alpine ASRB site SLF-Versuchsfeld (2540 m a.s.l.) measure both downward and upward shortwave, respectively longwave, fluxes. The total heating radiation (*THR*) and the longwave upward radiation (*LUR*) strongly increased at both sites. Part of the *THR* increase is caused by the reduction of days with snow cover, i.e. decline of surface albedo. The net cloud effect (*NCE*) and shortwave downward radiation (*SDR*) remained stable. The largest part of the *THR* increase is caused by an increase of the longwave downward radiation (*LDR*). This is a consequence of the intensifying cloud-free and all-sky greenhouse effect ( $G_{\text{cf}}$  and  $G_{\text{all}}$ ) due to rising greenhouse gas concentrations. Thus the short time period of eight years shows strong evidence of an enhanced cloud-free and all-sky greenhouse effect over Switzerland.

## 8.2 Outlook

Results from eight years of ASRB measurements approve that the Alps represent a unique region to investigate the altitude dependency and local distribution of various radiation parameters. ASRB measurements may be also suitable to detect radiation budget changes due to enhanced greenhouse gas forcing. It is planned to integrate the ASRB network in the new SwissMetNet, which is going to replace the old automatic network (ANETZ) from MeteoSwiss. If the number of ASRB sites has to be reduced, then the radiation measurements at the following stations should be carried on at least: Locarno-Monti, Cimetta, Davos, SLF-Versuchsfeld and Jungfrauoch. Results from the field calibration of ASRB instruments suggest to proceed with the proved calibration method using a Travelling Standard, and to implement the same quality and correction procedures in Zurich as used here in Davos to guarantee the homogeneity of ASRB radiation data in the future. Field calibration and homogenization of ASRB global shortwave measurements still remains an open task.

Longterm ASRB data series open up the possibility to describe radiation and cloud climatologies over the Alps on a monthly basis. Surface measurements can be used to validate satellite based surface

---

radiation retrievals. There is also an urgent need to compare the cloud-free and all-sky greenhouse effect at the surface with satellite measurements. Combinations of APCADA cloud cover estimates and satellite cloud retrievals have the potential to provide a 3-D cloud dataset for the validation of regional climate and weather prediction models. Future investigations should also concentrate on the specific influence of different cloud species on radiation balance, e.g. cirrus clouds. The reason is that large uncertainties still exist about the role of clouds for climate change.



## Appendix A

### Code for diffuse SDR estimation

```
1.  if ( q_std > 0.08 )
2.    if ( q_r > 0.30 )
3.      if ( q_diff > 0.30 )
4.        SDR_d,i = q_min^m*TSI*cos(z)
5.      else
6.        SDR_d,i = SDR_d,i-1
7.      endif
8.    else
9.      if (( q_diff >= 0.25 )&&( q_std < 0.12 ))
10.        SDR_d,i = SDR
11.      else
12.        if (( q_diff < 0.05 )&&( q_r > 0.10 ))
13.          SDR_d,i = (0.50+alb_offset)*SDR
14.        else
15.          SDR_d,i = (0.40+alb_offset)*SDR
16.        endif
17.      endif
18.    endif
19.  else
20.    if (( q_diff < 0.05 )&&( q_r > 0.20 ))
21.      SDR_d,i = SDR_d,i-1
22.    else
23.      if (( q_std < 0.04)&&( q_diff < 0.15 ))
24.        if ( q_diff < 0 )
25.          q_diff = 0
26.        endif
27.        SDR_d,i = (0.10+2*q_diff+alb_offset)*SDR
28.      else
29.        if (( q_diff < 0.10 )&&(q_r <= 0.10))
30.          SDR_d,i = (0.25+alb_offset)*SDR
31.        else
32.          if (( q_diff < 0.15 )&&(q_r > 0.10))
33.            SDR_d,i = (0.40+alb_offset)*SDR
34.          else
35.            if (q_r > 0.25)
```

```
36.         SDR_d,i = SDR_d,i-1
37.     else
38.         SDR_d,i = SDR
39.     endif
40. endif
41. endif
42. endif
43. endif
44. endif
```

**Legend** (see also section (3.2.2)):  $q\_std = q_{std}$ ,  $q\_r = q_r$ ,  $q\_diff = q_{diff}$ ,  $SDR\_d, i = SDR_{d,i}$ ,  $q\_min = q_{min}$ ,  $m = \text{airmass}$ ,  $z = \text{zenith angle } \theta$ ,  $alb\_offset = \Delta a$ .



# List of Figures

2.1	The Alpine Surface Radiation Budget (ASRB) network in Switzerland, Central Europe (Latitude $\approx 46^\circ\text{N}$ ). In parenthesis altitudes are given in meter a.s.l. . . . .	16
3.1	Example day at Payerne on 04.07.2001. The upper figure compares measured diffuse shortwave downward radiation ( $SDR_d$ ) to the old and new $SDR_d$ estimation methods ( $SDR_d$ new, $SDR_d$ cubic spline). The lower figure indicates the mean transmissivity ( $q_{avg}$ ) and transmissivity limit for cloud-free conditions ( $q_{limit}$ ) in the upper part, and the lower part shows the range ( $q_r$ ) and Stdev ( $q_{std}$ ) of $q$ within the past 30 minutes. . . . .	21
3.2	Annual cycle of $SDR_d$ difference in Payerne. . . . .	22
3.3	Standard set-up of the pyrano- and pygeometer and their ventilation- and heating system at each ASRB-station. The vertical fixed shadowband in direction south provides a uniform shadow during 20 min around solar noon. Envelope and radius $r$ of the cylinder for the integration of the shadowband shielding angle are also shown. . . . .	23
3.4	ASRB Travelling Standard (ASRB-TS) positioned at ASRB-site Cimetta. The ASRB-TS is made up of the same instruments and the same ventilation set-up as standard ASRB-stations. Both ASRB-TS instruments are regularly calibrated at PMOD/WRC in Davos. . . . .	27
4.1	Variability of longwave downward radiation within the past hour (Stdev $LDR$ ) (a) and Cloud-Free Index ( $CFI$ ) (b) plotted against partial cloud amount ( $PCA$ ) for 322 daytime observations (12 UTC) in Payerne in 2001. $CFI$ allows to separate between cloud-free (0 or 1 octa) and overcast (7 or 8 octas) situations. Compared to cloud-free or overcast conditions, broken cloud amounts (2 to 6 octas) are both characterised by different $CFI$ values and large $LDR$ variability. . . . .	35
4.2	Calculated Cloud-Free Index ( $CFI$ ) values plotted for daytime (1530 LT) winter cases with low variability of longwave downward radiation over two hours (Stdev $LDR_{2h} \leq 1 \text{ Wm}^{-2}$ ) at the ASRB station Weissfluhjoch. Cases with $CFI$ values around 1 indicate cloud-free, and cases with $CFI \gg 1$ totally overcast conditions. . . . .	37
4.3	Apparent emittance of all cases in Fig. 4.2 with $CFI < 0.99$ as a function of screen level water vapour pressure and temperature. The curve fit represents Eq. (4.9) with $\Delta k = 0$ and is used to determine $k$ . . . . .	38
4.4	Diurnal cycle of score index for maximum zero, one or two octas difference between estimated and observed partial cloud amount in Payerne from 1996–98. The score for zero octa difference decreases from about 60 at midnight to 45 in the late afternoon. Score rates for maximum one or two octas difference remain stable all over the day. . . .	42

- 4.5 Comparison of observed and estimated partial cloud amount (*PCA*) for a single day in Payerne. Overcast (00 UTC – 04 UTC) and mostly cloud-free conditions (18 UTC – 24 UTC) are characterised by small *LDR* variability (Stdev *LDR*), but different *CFI* values. Broken cloud conditions (04 UTC – 18 UTC) show enhanced *LDR* variability and most of the *PCA* estimates vary between 2 and 6 octas. . . . . 42
- 5.1 Mean *CFI* and *CFI<sub>sat</sub>* for Davos during nighttime (03 UTC  $\pm$  1 hour). The solid line indicates *CFI<sub>max</sub>*. The annual cycle of *CFI<sub>sat</sub>* is clearly reduced compared to the annual cycle of *CFI*. . . . . 46
- 5.2 Average *CFI*-saturation (*CFI<sub>sat</sub>*) for calm overcast and cloud-free nighttime cases at ASRB Weissfluhjoch and ASRB Davos. Single points indicate nighttime means (03 UTC  $\pm$  1 hour) for Davos, and solid lines indicate trendlines for Davos over the whole period, and separately for the inhomogeneity between 1998 and 2002. The dotted-dashed trendlines for WFJ are also shown. . . . . 47
- 5.3 Uncorrected (upper figure) and corrected (lower figure) *CFI*-saturation (*CFI<sub>sat</sub>*) in Davos for cloud-free (*CFI<sub>sat</sub>*  $\approx$  –10%) and overcast (*CFI<sub>sat</sub>*  $\approx$  90%) nighttime (02–04 UTC) conditions. Single dots indicate nighttime (03 UTC  $\pm$  1 hour) means of *CFI<sub>sat</sub>*. The solid lines for Davos in the upper figure give the mean *CFI<sub>sat</sub>*-values for the reference period 2003, and the two correction periods from 1995 to 1998, and from 1998 to 2002. The solid lines in the lower figure indicate the trendlines for *CFI<sub>sat</sub>* in Davos after correction. Different dashed or dotted trendlines for Weissfluhjoch (WFJ) and SLF-Versuchsfeld (VSF) are shown for comparison. . . . . 49
- 5.4 Uncorrected (upper figure) and corrected (lower figure) *CFI*-saturation (*CFI<sub>sat</sub>*) at Jungfraujoch for cloud-free (*CFI<sub>sat</sub>*  $\approx$  –10%) and overcast (*CFI<sub>sat</sub>*  $\approx$  90%) nighttime (02–04 UTC) conditions. Single dots indicate nighttime (03 UTC  $\pm$  1 hour) means of *CFI<sub>sat</sub>*. The solid lines for Jungfraujoch in the upper figure give the mean *CFI<sub>sat</sub>*-values for the reference period 1998 to 2003, and the correction period from 1995 to 1997. The solid lines in the lower figure indicate the trendlines for *CFI<sub>sat</sub>* at Jungfraujoch after correction. Different dashed or dotted trendlines for Männlichen (MAE) and Eggishorn (EGH) are shown for comparison. . . . . 51
- 6.1 Scheme for insertion of measured meteorological data into aLMo vertical- or Payerne sounding profile at ASRB-station height. The original profile below ASRB height is skipped and measured surface parameters are inserted as the first profile point. MODTRAN interpolates temperature, humidity and pressure in the Surface Boundary Layer (SBL) up to the second profile point, where the vertical profiles are assumed to start from. The SBL thickness varies from 100 to 400 m. . . . . 56
- 6.2 Results from *LDR* model run 1. are compared to (a) 274 night- and (b) 94 daytime ASRB observations in Payerne from 1996–2001. . . . . 59
- 6.3 MODTRAN computed *LDR* using +11 hours aLMo profile- (model run 2.) and aLMo *LDR* forecasts (model run 3.) compared to (a) night- and (b) daytime ASRB observations in Payerne for 2000–01. . . . . 61
- 6.4 Cloud-free diurnal cycle of longwave downward radiation (*LDR*) and ground and 2 m temperatures in Payerne at 25th of June 2001. MODTRAN *LDR* was calculated with model run 2., and aLMo *LDR* with model run 3. . . . . 62
- 7.1 MODTRAN computed cloud-free greenhouse effect (*G<sub>cf</sub>*) versus measured cloud-free longwave upward radiation (*LUR<sub>cf</sub>*) at two ASRB stations during day- and nighttime. . . 69

---

7.2	Cloud-free Longwave upward radiation ( $LUR_{\text{cfr}}$ ) spectra seen from different levels above ground in Payerne. The cloud-free longwave outgoing radiation ( $LOR_{\text{cfr}}$ ) at the top of atmosphere (ToA) is dominated by surface emission in the atmospheric window (8–12 $\mu\text{m}$ ). . . . .	70
7.3	Annual mean all-sky values of shortwave net radiation ( $SNR$ ), albedo ( $Alb$ ), total heating radiation ( $THR$ ), longwave upward radiation ( $LUR$ ), total net radiation ( $TNR$ ), shortwave and longwave cloud effect ( $SCE;LCE$ ), net cloud effect ( $NCE$ ), cloud-free and all-sky greenhouse effect ( $G_{\text{cfr}};G_{\text{all}}$ ). Numbers indicate changes over the periods with values in parenthesis representing the standard deviation of residuals to the linear regression trend line. . . . .	71
7.4	Annual mean all-sky values of shortwave downward radiation ( $SDR$ ) and longwave downward radiation ( $LDR$ ). Numbers indicate changes over the periods with values in parenthesis representing the standard deviation of residuals to the linear regression trend line. . . . .	72



# List of Tables

1	Abbreviations and acronyms used in this study . . . . .	11
3.1	Seasonal transmissivity offset $\Delta q$ and albedo offset $\Delta a$ used to estimate the diffuse shortwave downward radiation $SDR_d$ from $SDR$ measurements. $SDR_d$ is calculated every two minutes with the help of the scheme given in Appendix A. . . . .	20
3.2	Mean differences of estimated minus measured $SDR_d$ at three ASRB sites in 2001. . . . .	20
3.3	Statistics for f-correction of direct solar radiation with estimated and measured diffuse shortwave downward radiation ( $SDR_d$ ) and comparison of ASRB and BSRN longwave downward radiation ( $LDR$ ) measurements in Payerne for 2001. . . . .	22
3.4	Effective shielding angle for shadowband ( $\Omega_{SB}$ ) and mast ( $\Omega_M$ ) at each ASRB-station and shielding correction coefficients $g_0$ and $g_1$ for ASRB pyrgeometers and ASRB Travelling Standard (ASRB-TS). . . . .	26
3.5	Mean sensitivity $C$ and correction factors $k_1, k_2, k_3$ for reference PIR pyrgeometer ( $PIR_{ref}$ ), ASRB Travelling Standard (ASRB-TS) PIR and ASRB Davos PIR. The maximum deviation of $C$ from several individual calibrations is given in parenthesis. . . . .	27
3.6	Individual dates for calibration of ASRB pyrgeometers and calibrated PIR sensitivity $C$ . In parenthesis the length of time period used for calibration and time offset of the centre of the time period from midnight (0000 UTC) is given in ten minute values. . . . .	28
3.7	Mean $LDR$ difference for data obtained from the first field-calibration campaign. $LDR$ was calculated with sensitivities $C$ for ASRB PIRs and ASRB Travelling Standard (ASRB-TS) from Tabs. 3.5 and 3.6. . . . .	28
4.1	Radiation stations, shortname, radiation network, used dataset, altitude and coordinates. . . . .	32
4.2	Station shortname, apparent emissivity $\epsilon_{AD}$ of completely dry atmosphere, factors $k$ and $\Delta k$ fitted for cloud-free summer cases from Jun.–Sept., 1999–2001. . . . .	37
4.3	Station shortname, apparent emissivity $\epsilon_{AD}$ of completely dry atmosphere, factors $k$ and $\Delta k$ fitted for cloud-free cases from Dec.–Mar., 1999 – 2001. . . . .	38
4.4	Scheme for estimating partial cloud amount ( $PCA$ ) using Cloud-Free Index ( $CFI$ ) and variability of longwave downward radiation (Stdev $LDR$ ). . . . .	39
4.5	Contingency matrix of observed and estimated partial cloud amount ( $PCA$ ) for Payerne given in octas. Percentage of observed $PCA$ for 2272 (=100%) cases at 12 UTC (13 LT) and percentage distribution of estimated $PCA$ for each observed octa. . . . .	40
4.6	Diurnal cycle and daily averages of scores for maximum one octa difference between estimated and observed partial cloud amount. . . . .	40
4.7	Annual cycle of scores for maximum zero, one or two octas difference between estimated and observed partial cloud amount in Locarno-Monti for 12 UTC. . . . .	40
5.1	Parameters for calculation of $LDR$ correction $\overline{\Delta LDR}$ at ASRB stations Davos and Jungfraujoch for cloud-free and overcast nighttime situations. . . . .	48

5.2	Correction time period and parameters for $LDR$ correction term $\Delta LDR_{\text{corr}}$ (Eq. 5.6) as a function of longwave net radiation ( $LNR$ ). Units are given in $\text{W m}^{-2}$ . . . . .	48
6.1	ASRB stations, abbreviation, altitude, aLMo gridpoint altitude and coordinates. . . . .	54
6.2	Overview of different longwave downward radiation ( $LDR$ ) computation model runs in Payerne and at six ASRB stations. . . . .	57
6.3	Mean $LDR$ difference (computed minus observed) and mean standard deviation for 54 nighttime- and 31 daytime cases in Payerne from 2000–01. Values are given in $\text{W m}^{-2}$ . . . . .	58
6.4	Mean $LDR$ difference (computed minus observed) and mean standard deviation for about 17 nighttime cases at six ASRB stations from 2000–01. Values are given in $\text{W m}^{-2}$ . . . . .	58
6.5	Mean sensitivities of MODTRAN longwave downward radiation ( $LDR$ ) computations. 274 cloud-free nighttime (23 UTC) and 94 cloud-free daytime (11 UTC) sounding profiles in Payerne from 1996 to 2001 were individually modified. Mean $LDR$ sensitivities and standard deviation were separately calculated for night- and daytime. Sensitivities are given in $\text{W m}^{-2}$ . . . . .	60
6.6	Mean temperature ( $T$ ) within the first km above given altitude and total Integrated Water Content ( $IWC$ ) up to 100 km a.s.l. from night- and daytime soundings used for sensitivity study (Tab. 6.5) in Payerne. . . . .	60
6.7	Average temperature ( $T$ ) and absolute humidity ( $U$ ) within the first km of the sounding- and aLMo profiles from 54 cloud-free night- (23 UTC) and 30 cloud-free daytime (11 UTC) cases in Payerne from 2000–01. Resulting irradiance difference is defined by multiplying the differences with the accordant sensitivity for temperature (2 a.) and absolute humidity (2. b) in Tab. 6.5. . . . .	63
6.8	Mean $LDR$ difference (computed minus observed) and mean standard deviation for about 59 nighttime- and 25 daytime cases for six ASRB stations from 1996 to 2001. Values are given in $\text{W m}^{-2}$ . . . . .	64

# Bibliography

- Aviolat, F., T. Cornu, and D. Cattani, Automatic clouds observation improved by an artificial neural network, *J. Atmos. Ocean. Technol.*, 15(1), 114–126, 1998.
- Beaubien, M., and A. Bisberg, A new ccd-based instrument for the automatic determination of cloud cover, in *10th Atmospheric Radiation Conference*, pp. 482–485, AMS, Madison, Wisconsin, 1999.
- Berk, A., G. P. Anderson, P. K. Acharya, J. H. Chetwynd, L. S. Bernstein, E. P. Shettle, M. W. Matthew, and S. M. Adler-Golden, *MODTRAN4 users manual*, Air Force Res. Lab., Space Vehicle Dir., Air Force Mater. Command, Hanscom Air Force Base, Mass., 2000.
- Brutsaert, W., On a derivable formula for longwave radiation from clear sky, *Water Resour. Res.*, 11(3), 742–744, 1975.
- Buck, A. L., New equation for computing water vapour pressure and enhancement factor, *J. Appl. Meteorol.*, 20(12), 1527–1532, 1981.
- Charlock, T. D., and V. Ramanathan, The albedo field and cloud radiative forcing produced by a general circulation model with internally cloud optics, *J. Atmos. Sci.*, 42, 1408–1429, 1985.
- Chevallier, F., and J.-J. Morcrette, Comparison of model fluxes with surface and top-of-the-atmosphere observations, *Mon. Weather Rev.*, 128(11), 3839–3852, 2000.
- Doms, G., and U. Schättler (Eds.), *Consortium for Small Scale Modelling (COSMO) Newsletter No. 4*, COSMO, [Available at: <http://cosmo-model.cscs.ch/> > Publications], 2004.
- Dutton, E. G., An extended comparison between LOWTRAN7 computed and observed broadband thermal irradiances: Global extreme and intermediate surface conditions, *J. Atmos. Ocean. Technol.*, 10(3), 326–336, 1993.
- Feister, U., J. Shields, M. Karr, R. Johnson, K. Dehne, and M. Woldt, Ground-based cloud images and sky radiances in the visible and near infrared region from whole sky imager measurements, in *Proc. of Climate Monitoring - Satellite Application Facility Training Workshop*, pp. 79–88, DWD, EUMETSAT and WMO, Dresden, 2000.
- Fröhlich, C., and J. Lean, The sun's total irradiance: cycles, trends and related climate change uncertainties since 1976, *Geophys. Res. Lett.*, 25(23), 4377–4380, 1998.
- Fröhlich, C., R. Philipona, and Ch. Marty, Untersuchung des Oberflächenstrahlungshaushaltes in den Alpen und im Vergleich zum schweizerischen Mittelland, Schlussbericht NFP 31, ISBN 3 7281 2504 0, 1998.

- Gilgen, H., C. Whitlock, F. Koch, G. Müller, A. Ohmura, D. Steiger, and R. Wheeler, Technical plan for BSRN (Baseline Surface Radiation Network) Data management, Version 2.1 (final), *Tech. Rep. WMO/TD No. 443*, WCRP/WMO, 1995.
- Gillotay, D., T. Besnard, and F. Zanghi, A systematic approach of the cloud cover by thermic infrared measurements, in *Proc. of 18th conference on Weather Analysis and Forecasting*, pp. 292–295, AMS, Fort Lauderdale, FL, USA, 2002.
- GLOBALVIEW-CO<sub>2</sub>, *Cooperative Atmospheric Data Integration Project - Carbon Dioxide*, CD-ROM, NOAA CMDL, Boulder, Colorado, [Also available on Internet via anonymous FTP to ftp.cmdl.noaa.gov, Path: ccg/co2/GLOBALVIEW], 2002.
- Gupta, S. K., W. F. Staylor, W. L. Darnell, A. C. Wilber, and N. A. Ritchey, Seasonal variation of surface and atmospheric cloud radiative forcing over the globe derived from satellite data, *J. Geophys. Res.*, *98*, 20,761–20,778, 1993.
- Haase, J., M. Ge, H. Vedel, and E. Calais, Accuracy and variability of GPS tropospheric delay measurements of water vapor in the western mediterranean, *J. Appl. Meteorol.*, *42*(11), 1547–1568, 2003.
- Hahn, C. J., S. G. Warren, and J. London, The effect of moonlight on observation of cloud cover at night, and application of cloud climatology, *J. Climate*, *8*(5), 1429–1446, 1995.
- Heimo, A., R. Philipona, C. Fröhlich, Ch. Marty, and A. Ohmura, The Swiss atmospheric radiation monitoring network CHARM, *Tech. Rep. WMO/TD No. 877*, WCRP/WMO, 1998.
- Houghton, J. T., Y. Ding, D. J. Griggs, M. Noguer, P. J. van den Linden, X. Dai, K. Maskell, and C. A. Johnson, *Climate Change 2001: The Scientific Basis*, Intergovernmental Panel of Climate Change, Cambridge Univ. Press, Cambridge, 2001.
- Inamdar, A. K., and V. Ramanathan, On monitoring the atmospheric greenhouse effect from space, *Tellus*, *49B*, 216–230, 1997.
- Isaacs, R. G., W. C. Wang, R. D. Worsham, and S. Goldenberg, Multiple scattering LOWTRAN and FASCODE models, *Appl. Opt.*, *26*, 1272–1281, 1987.
- Kasten, F., and A. T. Young, Revised optical air mass tables and approximation formula, *Appl. Opt.*, *28*(22), 4735–4738, 1989.
- Kneizys, F. X., et al., The MODTRAN 2/3 report and LOWTRAN 7 model, *Tech. rep.*, Phillips Laboratory, Hanscom AFB, MA, 1996.
- Long, C. N., and T. P. Ackermann, Identification of clear skies from broadband pyranometer measurements and calculation of downwelling shortwave cloud effects, *J. Geophys. Res.*, *105*, 15,609–15,626, 2000.
- Long, C. N., and J. DeLuisi, Development of an automated hemispheric sky imager for cloud fraction retrievals, in *Proc. of 10th Symp. On Meteorological Observations and Instrumentation*, pp. 215–218, AMS, Phoenix, Arizona, USA, 1998.
- Marty, Ch., Surface radiation, cloud forcing and greenhouse effect in the Alps, Ph.D. thesis, Institute of climate research ETH Zürich, 2000.
- Marty, Ch., and R. Philipona, The clear-sky index to separate clear-sky from cloudy-sky situations in climate research, *Geophys. Res. Lett.*, *27*, 2649–2652, 2000.



- Marty, Ch., R. Philipona, C. Fröhlich, and A. Ohmura, Altitude dependence of surface radiation fluxes and cloud forcing in the Alps: results from the alpine surface budget network, *Theor. Appl. Climatol.*, *72*, 137–155, 2002.
- Marty, Ch., et al., Downward longwave irradiance uncertainty under arctic atmospheres: Measurements and modeling, *J. Geophys. Res.*, *108*(D12), 4358, doi:10.1029/2002JD002937, 2003.
- McArthur, L. J. B., Baseline surface radiation network (BSRN). Operations manual, *Tech. Rep. WMO/TD No. 879*, WRCP/WMO, 1998.
- Mitchell, J., T. Johns, J. Gregory, and S. Tett, Climate response to increasing levels of greenhouse gases and sulphate aerosols, *Nature*, *376*, 501–505, 1995.
- Nadolski, V., United States moves ahead with deployment of the automated surface observing system, *OACI J.*, *50*(8), 10–11, 1995.
- Ohmura, A., Physical basis for the temperature-based melt-index method, *J. Appl. Meteorol.*, *40*, 753–761, 2001.
- Ohmura, A., et al., Baseline surface radiation network (BSRN/WCRP): New precision radiometry for climate research, *Bull. Amer. Meteorol. Soc.*, *79*, 2115–2136, 1998.
- Philipona, R., Sky-scanning radiometer for absolute measurements of atmospheric long-wave radiation, *Appl. Opt.*, *40*, 2376–2383, 2001.
- Philipona, R., Underestimation of solar global and diffuse radiation measured at Earth's surface, *J. Geophys. Res.*, *107*(D22), doi:10.1029/2002JD002396, 2002.
- Philipona, R., and B. Dürr, Greenhouse forcing outweighs solar dimming - driving rapid temperature rise over land, *Geophys. Res. Lett.*, submitted, 2004.
- Philipona, R., C. Fröhlich, and Ch. Betz, Characterization of pyrgeometers and the accuracy of atmospheric long-wave radiation measurements, *Appl. Opt.*, *34*, 1598–1605, 1995.
- Philipona, R., B. Dürr, and Ch. Marty, Greenhouse effect and altitude gradients over the Alps - by surface longwave radiation measurements and model calculated LOR, *Theor. Appl. Climatol.*, *77*, 1–7, doi:10.1007/s00704-004-0038-7, 2004a.
- Philipona, R., B. Dürr, Ch. Marty, A. Ohmura, and M. Wild, Radiative forcing - measured at Earth's surface - corroborate the increasing greenhouse effect, *Geophys. Res. Lett.*, *31*, doi:10.1029/2003GL018765, 2004b.
- Philipona, R., et al., The baseline surface radiation network pyrgeometer round-robin calibration experiment, *J. Atmos. Ocean. Technol.*, *15*, 687–696, 1998.
- Philipona, R., et al., Atmospheric longwave irradiance uncertainty: Pyrgeometers compared to an absolute sky-scanning radiometer, AERI and radiative transfer model calculations, *J. Geophys. Res.*, *106*, 28,129–28,141, 2001.
- Raval, A., and V. Ramanathan, Observational determination of the greenhouse effect, *Nature*, *342*, 758–761, 1989.
- Richner, H., Grundlagen aerologischer Messungen speziell mittels der Schweizer Sonde SRS 400, *Tech. Rep. 61*, Federal Office of Meteorology and Climatology, Postfach 514, CH-8044, Zürich, Switzerland, 1999.

- Ritter, B., and J.-F. Geleyn, A comprehensive radiation scheme for numerical weather prediction models with potential applications in climate simulations, *Mon. Weather Rev.*, 120(2), 303–325, 1992.
- Ruppert, P., THYGAN, Beschreibung der Funktion und der Technik, *Tech. Rep. 164*, Federal Office of Meteorology and Climatology, Postfach 514, CH-8044, Zürich, Switzerland, 1991.
- Slingo, A., J. A. Pamment, and M. J. Webb, A 15-year simulation of the clear-sky greenhouse effect using the ECMWF reanalyses: Fluxes and comparisons with ERBE, *J. Climate*, 11(4), 690–708, 1998.
- Stephens, G. L., The parametrization of radiation for numerical weather prediction and climate models, *Mon. Weather Rev.*, 112, 826–867, 1984.
- Tett, S., P. Stott, M. Allen, W. Ingram, and J. Mitchell, Causes of twentieth century temperature change near the Earth's surface, *Nature*, 399, 569–575, 1999.
- Wardle, D. I., and D. V. Barton, Zero offsets in pyranometer signals related to long-wave radiation, temperature change and ventilation and some implications regarding measurement uncertainty, *Tech. Rep. ARPD-129X52*, Atmospheric Environment Service, Canada, 1988.
- Wild, M., and A. Ohmura, Longwave forcing at the surface as simulated in transient climate change experiments, in *IRS2000: Current Problems in Atmospheric Radiation*, edited by W. L. Smith and Yu. M. Timofeyev, pp. 745–748, A Deepak publ., Hampton, VA, 2001.
- Wild, M., A. Ohmura, H. Gilgen, and E. Roeckner, Regional climate simulation with a high resolution GCM: Surface radiative fluxes, *Clim. Dynam.*, 11, 469–486, 1995.
- Wild, M., A. Ohmura, and U. Cubasch, GCM-simulated surface energy fluxes in climate change experiments, *J. Climate*, 10(12), 3093–3110, 1997.
- Wild, M., A. Ohmura, H. Gilgen, J.-J. Morcrette, and A. Slingo, Evaluation of downward longwave radiation in general circulation models, *J. Climate*, 14(15), 3227–3239, 2001.
- WMO, Manual on codes, *Tech. Rep. 306*, World Meteorological Organization, 41 avenue Giuseppe Motta, CP-2300, CH-1211 Geneva, Switzerland, 1993.
- Zdunkowski, W. G., R. M. Welch, and G. J. Korb, An investigation of the structure of typical two-stream methods for the calculation of solar fluxes and heating rates in clouds, *Contrib. Atmos. Phys.*, 53, 147–166, 1980.

# Acknowledgements

A lot of people helped me in many ways to bring this work to a successful end. I want to specially thank the following persons:

- My advisor, Prof. Atsumu Ohmura (Institute for Atmosphere and Climate (IACETH) at the ETH Zurich), who had a lot of patience to answer my questions, and who evaluated thoroughly my plans and thoughts to give me helpful advice for further investigations.
- My supervisor, PD Dr. Rolf Philipona, who invited me to attend my practical training 1998 in Davos, and who offered me the opportunity to complete my PhD at the PMOD/WRC. He gave me the motivation and inspiration to try hard to gain deeper insight into the science of radiation. He always took the time for my questions, even when he actually didn't have any time at all.
- Prof. Dr. Werner Schmutz, director of PMOD/WRC, who offered the well-maintained infrastructure at PMOD/WRC and continued the financial support by the observatory for my PhD after the end of the grant of the Swiss National Science Foundation in 2003.
- Dr. Francis Schubiger, working at the NWP-group at MeteoSwiss, who provided me forecast data of the aLMo NWP-model, and who introduced me to the specific problems of numerical modelling.
- Dr. Claus Fröhlich, former director of PMOD/WRC, who gave me important advice about the radiative transfer model MODTRAN.
- Armand Vernez, Evio Tognini, Serge Brönnimann and Nicola Gobbi, working at MeteoSwiss, and Franz Herzog at the SLF in Davos, who were all very busy to repair any damage at the ASRB stations as quick as possible.
- All staff members at PMOD/WRC, who made the everyday life interesting with many discussions, celebrations, sports, etc.

And a very special thank goes to all other people, who supported me to become a climatologist!

The work was financed by the Swiss National Science Foundation (Grant No. 21-58746.99) and PMOD/WRC.



# Curriculum Vitae

Dürr Bruno

born on October 16, 1975 in Gams, Switzerland

citizen of Gams (SG), Switzerland

## Education

- 1982–1988 Primary school in Gams
- 1988–1990 Secondary school in Gams
- 1990–1995 Kant. Gymnasium in Sargans (SG)
- 1995–2000 Swiss Federal Institute of Technology (ETH), Zurich, Dipl. Natw. ETH
- 2000–2004 PhD student at Physikalisch-Meteorologisches Observatorium Davos / World Radiation Center (PMOD/WRC)

## Professional Training

- August 1998 Practical training (4 weeks) at PMOD/WRC Davos
- 1998–1999 Auxiliary assistant at the Laboratory of Hydraulics, Hydrology and Glaciology at ETH Zurich

## Conference Contributions:

- International Association of Meteorology and Atmospheric Sciences (IAMAS), 8th Scientific Assembly, Innsbruck, Austria, July 2001.
- DACH Meteorologentagung, Vienna, Austria, September 2001.
- Annual meeting of Swiss Meteorological Society (SGM), Davos, Switzerland, September 2002.
- International Conference on Alpine Meteorology (ICAM), Brig, Switzerland, May 2003.

## Publications:

- *Automatic cloud amount detection by surface longwave downward radiation measurements*, Authors: B. Dürr and R. Philipona, *Journal of Geophysical Research*, Vol. 109, doi: 10.1029/2003JD004182, 2004.
- *Comparison of modeled and observed cloud-free longwave downward radiation over the Alps*, Authors: B. Dürr, R. Philipona, F. Schubiger and A. Ohmura, *Meteorologische Zeitschrift*, accepted.

- 
- *Radiative forcing - measured at Earth's surface - corroborate the increasing greenhouse effect*, Authors: R. Philipona, B. Dürr, Ch. Marty, A. Ohmura and M. Wild, *Geophysical Research Letters*, Vol. 31, doi:10.1029/2003GL018765, 2004.
  - *Greenhouse effect and altitude gradients over the Alps - by surface longwave radiation measurements and model calculated LOR*, Authors: R. Philipona, B. Dürr, and Ch. Marty, *Theoretical and Applied Climatology*, Vol. 77, 2004.
  - *Greenhouse forcing outweighs decreasing solar radiation - driving rapid temperature rise over land.*, Authors: R. Philipona and B. Dürr, *Geophysical Research Letters*, Vol. 31, doi: 10.1029/2004GL020937, 2004.
  - *Comparison of two radiation algorithms for surface-based cloud-free sky detection*, Authors: M. Sutter, B. Dürr and R. Philipona, *Journal of Geophysical Research*, Vol. 109, doi: 10.1029/2004JD004582, 2004.